Tailoring Poisson's Ratio in Nanoporous Metals

Vom Promotionsausschuss der
Technischen Universität Hamburg

zur Erlangung des akademischen Grades

Doktor-Ingenieur (Dr.-Ing.)

genehmigte Dissertation (Monografie)

von
Haonan Sun

aus
Shenyang, China

2026

Erstgutachter: Prof. Dr.-Ing. Shan Shi

Zweitgutachter: PD Dr.-Ing. habil. Nikolai Kashaev

Vorsitzender: Prof. Dr. rer. nat. habil Alexander Petrov

Tag der mündlichen Prüfung: 22. Oktober 2026

Acknowledgments

Throughout my doctoral studies, I received invaluable support and assistance from many people. I would like to thank everyone for their invaluable support and guidance throughout my doctoral journey. I would like to express my special gratitude to my doctoral supervisor, Dr.-Ing. Shan Shi, who was also my research mentor. She provided me with extensive research guidance and offered me valuable life advice, which greatly changed my attitude towards life. I would also like to thank the chair of my dissertation defence, Dr. rer. nat. habil Alexander Petrov, and the invited reviewer, Dr.-Ing. habil Nikolai Kashaev. Thank you for taking the time to participate in my dissertation defence and review; it was an honour to work with you to improve my dissertation.

In my four years at the TUHH, I had the companionship of old friends and also made many new ones, both my compatriots and international friends. I am grateful to Zhongyang Li, without him, I wouldn't have known they were hiring, and I wouldn't have come here; Ying Zhang, man what can I say, as my senior brother, is a role model for me in both personal character and research; Wei-che Chang is a sincere friend, being with him is always a pleasure; Yong Li, as my good older brother, he has given me much valuable advice and taught me a great deal in the writing of my thesis; Boyi Zhang is a very rare friend, thank you for your valuable advice regarding my residence permit application.

As a friend I've worked with, Lukas Lührs was my mentor at the beginning of my doctoral dissertation, I learned DIC from him, which is one of the core testing techniques in my doctoral work; Fatemeh Ebrahimi is diligent and hardworking. I hope she learns German well and finds a good job soon.

There are so many people I need to thank; if I were to list them all here, it would probably be longer than Chapter 5 of this thesis. In short, I want to express my gratitude to everyone who has helped and accompanied me during these four years of work! Wishing us all the best for the future.

Abstract

Poisson's ratio is a fundamental mechanical property that reflects volumetric deformation, yet its role in nanoporous metals has received far less attention than stiffness or strength. In particular, the dependence of Poisson's ratio on network architecture and chemical environment in nanoscale porous solids remains poorly understood. This dissertation addresses this gap by systematically investigating Poisson's ratio in dealloyed nanoporous metals, focusing on two complementary tuning strategies: architectural hierarchy and chemo-mechanical coupling.

In the first part, hierarchical nanoporous gold with nested bicontinuous network architectures was reproducibly fabricated using a three-step dealloying–annealing–dealloying route. This approach enabled independent control of two ligament length scales while maintaining monolithic, crack-free samples. Uniaxial compression combined with in-situ digital image correlation was used to measure axial and transverse strains, allowing both elastic and plastic Poisson's ratios to be determined. The results show that Poisson's ratio is largely insensitive to the upper-level ligament size and is governed primarily by the effective solid fraction of the load-bearing network. A scaling law for the elastic Poisson's ratio in hierarchical network materials is proposed and experimentally validated.

In the second part, the dissertation examines reversible tuning of Poisson's ratio through chemical control. Nanoporous palladium and palladium–gold alloys were subjected to electrochemically controlled hydrogen absorption and desorption, enabling precise adjustment of hydrogen concentration under potentiostatic, near-equilibrium conditions. In nanoporous PdAu, the elastic Poisson's ratio is reduced by nearly 50% at intermediate hydrogen concentration, in quantitative agreement with predictions from Larché–Cahn open-system elasticity. These results provide the first experimental verification of an open-system elastic Poisson's ratio and extend validation of open-system elasticity beyond Young's modulus.

Together, this dissertation demonstrates that Poisson's ratio in nanoporous metals is not a fixed material constant but a tunable property that can be tailored through structural design and controlled chemical loading. By linking nanoscale architecture, solute redistribution and mechanical response, this work provides a mechanistically informed basis for understanding and controlling volumetric deformation in porous metallic networks.

Zusammenfassung

Die Querkontraktionszahl (Poissonzahl) ist eine fundamentale mechanische Eigenschaft, die die Volumenverformung widerspiegelt. Ihre Rolle in nanoporösen Metallen wurde jedoch deutlich weniger beachtet als die von Steifigkeit oder Festigkeit. Insbesondere die Abhängigkeit der Querkontraktionszahl von der Netzwerkarchitektur und der chemischen Umgebung in porösen Nanostrukturen ist noch unzureichend erforscht. Diese Dissertation schließt diese Lücke durch die systematische Untersuchung der Querkontraktionszahl in entlegierten nanoporösen Metallen. Der Fokus liegt dabei auf zwei komplementären Strategien zur Optimierung: der architektonischen Hierarchie und der chemomechanischen Kopplung.

Im ersten Teil wurde hierarchisch nanoporöses Gold mit verschachtelten bikontinuierlichen Netzwerkarchitekturen reproduzierbar mittels eines dreistufigen Verfahrens aus Entlegierung, Temperung und erneuter Entlegierung hergestellt. Dieser Ansatz ermöglichte die unabhängige Kontrolle zweier Ligamentlängenskalen bei gleichzeitiger Erhaltung monolithischer, rissfreier Proben. Mittels uniaxialer Kompression in Kombination mit digitaler Bildkorrelation in situ wurden axiale und transversale Dehnungen gemessen, wodurch sowohl die elastische als auch die plastische Querkontraktionszahl bestimmt werden konnte. Die Ergebnisse zeigen, dass die Querkontraktionszahl weitgehend unabhängig von der Größe der oberen Ligamente ist und primär vom effektiven Feststoffanteil des lasttragenden Netzwerks abhängt. Ein Skalierungsgesetz für die elastische Querkontraktionszahl in hierarchischen Netzwerkmaterialien wird vorgeschlagen und experimentell validiert.

Im zweiten Teil untersucht die Dissertation die reversible Einstellung der Querkontraktionszahl durch chemische Steuerung. Nanoporöses Palladium und Palladium-Gold-Legierungen wurden einer elektrochemisch kontrollierten Wasserstoffabsorption und -desorption unterzogen, wodurch die Wasserstoffkonzentration unter potentiostatischen, nahezu im Gleichgewicht befindlichen Bedingungen präzise eingestellt werden konnte. In nanoporösem PdAu wird die elastische Querkontraktionszahl bei mittlerer Wasserstoffkonzentration um fast 50% reduziert, was quantitativ mit Vorhersagen der Larché-Cahn-Elastizitätstheorie für offene Systeme übereinstimmt. Diese Ergebnisse liefern den ersten experimentellen Nachweis einer elastischen Querkontraktionszahl für ein offenes System und erweitern die Validierung der Elastizitätstheorie für offene Systeme über den Elastizitätsmodul hinaus.

Diese Dissertation zeigt, dass die Querkontraktionszahl in nanoporösen Metallen keine feste Materialkonstante, sondern eine einstellbare Eigenschaft ist, die durch Strukturdesign und kontrollierte chemische Beladung gezielt beeinflusst werden kann. Durch die Verknüpfung von Nanoarchitektur, Stoffverteilung und mechanischem Verhalten liefert diese Arbeit eine mechanistisch fundierte Grundlage für das Verständnis und die

Kontrolle der Volumenverformung in porösen Metallnetzwerken.

Contents

List of Figures **ix**

List of Tables **xv**

List of Abbreviations **xvii**

1 Introduction **1**
1.1 Background and Motivation 1
1.2 Dealloying-made nanoporous metals 4
1.3 Poisson's Ratio in nanoporous metal 5
1.4 Larché–Cahn Open-System Elasticity 8
1.5 Outline of the Thesis 10

2 Theoretical Fundamentals **11**
2.1 Fundamentals of dealloying 11
2.1.1 Thermodynamic and electrochemical prerequisites 11
2.1.2 The parting limit: connectivity versus kinetics 12
2.1.3 Critical dealloying potential and polarization behavior 13
2.1.4 Mechanistic models of porous-network formation during dealloying 15
2.1.5 Morphology evolution and coarsening 15
2.2 Poisson's Ratio in isotropic linear elasticity 16
2.3 Scaling Laws 18
2.4 Open-System Elasticity (Larché-Cahn Theory) 20
2.4.1 Thermomechanical Framework and Key Definitions 20
2.4.2 Maxwell Relations and the Origin of Chemo-Mechanical Coupling 21
2.4.3 Closed-System Elasticity vs. Open-System Elasticity 22
2.4.4 Isotropic Approximation 22
2.4.5 Implications for np Pd–H Systems 23

3 Materials Preparation and Methods **27**
3.1 Material 27
3.2 Electrochemical dealloying and in situ electrochemical tests 28
3.2.1 HNPG 29
3.2.2 np Pd and np PdAu 33
3.3 Sample characterization 35
3.3.1 Imaging, elemental composition and structural analysis 35
3.3.2 Solid Volume Fraction Measurement 36

3.3.3 Mechanical Characterization and Digital Image Correlation . . . 36

4 Poisson's Ratio in Hierarchical Nanoscale Networks 41
4.1 Results . . . 41
4.1.1 Microstructure . . . 41
4.1.2 Mechanical properties . . . 44
4.2 Discussion . . . 49
4.2.1 Impact of upper level ligament size . . . 49
4.2.2 Impact of solid volume fraction . . . 54
4.2.3 Evolution of mechanical properties during compressive deformation 56
4.3 Chapter Summary . . . 58

5 Hydrogen-induced Tunable Poisson's Ratio in np Pd 59
5.1 Results . . . 60
5.1.1 Microstructure and Phase Composition . . . 60
5.1.2 Poisson's ratio variation with hydrogen concentration . . . 63
5.2 Discussion . . . 67
5.2.1 Comparison with open-system elasticity model . . . 67
5.2.2 Hydrogen-Mechanics Coupling in np Pd vs. np PdAu . . . 69
5.2.3 Equilibration, Gorsky limit and validity of open-system parameters . . . 71
5.3 Chapter Summary . . . 73

6 Summary and Outlook 75
6.1 Summary . . . 75
6.2 Outlook . . . 76

Bibliography 79

Publications & Conferences 93

List of Figures

1.1 Microstructure images of nanoporous metals. (a) Scanning electron micrograph (SEM) of nanoporous gold (NPG); (b) SEM of nanoporous gold platinum alloy (np AuPt); (c) SEM of nanoporous palladium (np Pd) and (d) Transmission Electron Microscopy (TEM) of nanoporous platinum (np Pt). Reprinted with permission from Ref [9–12], respectively. 2

1.2 Microstructure images of hierarchical nanoporous metals. (a) SEM of hierarchical nanoporous gold fabricated via a dealloying-coarsening-dealloying method; (b) SEM of hierarchical nanoporous copper fabricated by one-step dealloying. Reprinted with permission from Ref [50, 68], respectively 5

2.1 Schematic illustration of an anodic polarization curve for a binary alloy undergoing electrochemical dealloying. The transition from passivation-like behavior to sustained selective dissolution defines the critical dealloying potential E_c. Reprinted with permission from Ref [131]. 14

2.2 Arrhenius plot of the normalized ligament diameter d/L as a function of inverse temperature for thermally coarsened nanoporous gold. The linear behavior indicates thermally activated coarsening kinetics, with an activation energy consistent with surface diffusion of gold atoms. Reprinted with permission from Ref [139]. 16

2.3 Schematic illustration of Poisson's ratio (ν): under stress (σ), the material contracts in the axial direction (with axial strain, $\varepsilon_{\text{axial}}$) and expands in the transverse direction (with transverse strain, $\varepsilon_{\text{trans}}$). ν quantifies this coupling as the negative ratio of transverse to axial strain, $\nu = -\varepsilon_{\text{trans}}/\varepsilon_{\text{axial}}$. 17

2.4 Scaling behaviors of shear modulus (G) and elastic Poisson's ratio (ν_{E}) with solid fraction (φ_{net}) of nanoporous gold with different numbers (n) of hierarchical levels. (a) G versus φ_{net} for n=1-2; (b) ν_{E} versus φ_{net} for n=1-2. Open purple rhombuses: G is estimated from experimental Y and ν_{E} of NPG in literature; Red solid lines in (a): Eq. 2.16; Red solid lines in (b): Eq. 2.17. 20

2.5 Chemical potential, susceptibility and open-system Poisson's ratio for a regular interstitial solution using parameters representative of Pd. (a) Normalized chemical potential μ/RT_C, (Eq. 2.31) at different temperatures. The legend indicates the reduced temperature, $\tau = T/T_C$, where T_C is the critical temperature. The dash line shows the miscibility gap for $T < T_C$; (b) Susceptibility, χ, of the Pd–H system modeled as a regular interstitial solution using Pd–H parameters; (c) Open-system Poisson's ratio, ν^μ (Eq. 2.29) and (d) relative Poisson's ratio, ν^μ/ν^x as functions of x. At the critical temperature ($\tau = 1$), ν^μ exhibits the steepest variation with x; consequently, ν^μ changes from its initial value to -1 at the critical point. 24

3.1 Three-electrode electrochemical cell used for dealloying. (a) Schematic illustration of the unified cell configuration, showing the working electrode (WE), counter electrode (CE) and reference electrode (RE) connected to a potentiostat for potential control; (b) Photograph of the actual electrochemical cell equipped with an external water jacket for precise temperature control of the electrolyte. 28

3.2 Preparation process, appearance and microstructure of HNPG. (a) Scheme describing the synthesis route and structural features of each stage from $Ag_{93}Au_7$ master alloy to nanoporous $Ag_{75}Au_{25}$ (NPSG) alloy and then to HNPG; (b) SEM images showing the fracture surface microstructure of HNPG. The lower level ligaments were embedded in the upper level ligaments to form a hierarchical structure and (c) optical microscope images of HNPG free from cracks and defects. The dimensions and weight are then measured to obtain the solid volume fraction. . . . 30

3.3 Electrochemical protocol for the first-step partial dealloying of $Ag_{93}Au_7$ (at.%) to form nanoporous $Ag_{75}Au_{25}$. (a) Constant applied potential of 0.359 V vs. pseudo-Ag/AgCl in 0.01 M H_2SO_4; (b) transient current response showing the decay as Ag is selectively dissolved and (c) integrated anodic charge versus time. The dealloying process was terminated when the cumulative charge matched the target value Q_{target}, calculated from the desired change in Ag atomic fraction using Faraday's law. 31

3.4 Representative electrochemical protocol for the final dealloying step to obtain HNPG from coarsened NPSG precursors. (a) Time sequence of applied potentials in 1.0 M $HClO_4$: an initial step at 0.8 V followed by a higher-potential step at 1.0 V (both vs. pseudo-Ag/AgCl), designed to enable gradual Ag removal while avoiding crack formation; (b) Corresponding current response showing rapid decay during each step, consistent with progressive surface passivation and compositional evolution; (c) Integrated anodic charge versus time, used to monitor total Ag dissolution and (d) Subsequent cyclic voltammetry (CV) between 0.34 and 0.99 V (5 cycles at 10 mV/s). 32

3.5 Representative electrochemical protocol for dealloying $Pd_{15}Cu_{85}$ in 1.0 mol/L H_2SO_4 at 60 °C. (a) Applied dealloying potential = 0.576 V vs. commercial Ag/AgCl; (b) resulting current response and (c) integrated charge over time. 34

3.6 Representative cyclic voltammetry (CV) data of nanoporous Pd in 1.0 mol/L H_2SO_4 at room temperature, recorded at a scan rate of 10 mV/s. (a) Time evolution of the applied potential vs. commercial Ag/AgCl during potential cycling; (b) Current–potential response of the np Pd, showing characteristic redox peaks associated with hydrogen adsorption/desorption and surface oxidation/reduction processes. The shape and stability of the cyclic voltammetry reflect the electrochemical activity and surface state of the dealloyed np Pd. 34

3.7 Representative electrochemical protocol for dealloying $Pd_{12.5}Au_{2.5}Cu_{85}$ in 1.0 mol/L H_2SO_4 at 80 °C using a two-step potentiostatic procedure. (a) Applied potential profile: the first step at 0.74 V vs. SHE (0.526 V vs. commercial Ag/AgCl) and the second at 0.79 V vs. SHE (0.576 V vs. commercial Ag/AgCl); (b) Corresponding current transient shows rapid decay in both steps as Cu dissolution proceeds and (c) Integrated charge vs. time reveals the cumulative electrochemical charge passed, enabling estimation of Cu removal via Faraday's law. 35

3.8 Mechanical characterization for HNPG and np Pd/np PdAu samples. (a) Photo of the setup for HNPG. A high-precision/high-speed camera and a matching adjustable illumination device. The sample to be tested is placed between the conical push rods of a universal mechanical testing device, which are designed to provide an enhanced illumination on the surface of the sample being tested; (b) In situ compression setup used for np Pd and np PdAu samples, featuring a transparent electrochemical cell to allow hydrogen charging under potentiostatic or open-circuit conditions. Details are described in Sec. 3.2.2 and (c) Simplified schematic diagram of the setup, illustrating that the random characteristics of the sample surface are created using artificial spray paint to enhance contrast and allow more accurate DIC analysis. 38

3.9 In situ electrochemical cell used for hydrogen absorption/desorption experiments on np Pd and np PdAu. (a) Overview of the customized three-electrodes setup used inside the in situ mechanical testing stage; (b) enlarged view showing the working electrode (WE), reference electrode (RE, SHE) and carbon cloth counter electrode (CE) during operation. . 39

3.10 The digital image correlation (DIC) setup. (a) A high-resolution image of one HNPG sample under the camera with proper exposure and focus to ensure the accuracy of DIC analysis. ε_t and ε_a represent the transverse and axial strain respectively. Virtual strain gauge maps of (b) ε_t and (c) ε_a when the engineering strain is 10%. 40

4.1 Microstructure of NPSG alloy and HNPG samples at different annealing temperatures. (a-d): SEM images of NPSG alloy annealed at 300 °C, 350 °C, 400 °C and 450 °C, respectively, showing ligament sizes of 70 nm, 100 nm, 140 nm and 180 nm. (e-h) SEM images of the HNPG samples dealloyed out of NPSG alloy samples in (a-d), showing the same lower level ligament size (L_1) of 20 nm, while the upper level ligament size (L_2) retain the original ligament size of the corresponding NPSG alloy; (i-l) Further zoom in (e-h), which show more details of lower level ligament. 42

4.2 SEM images of HNPG samples with same upper level ligament size, L_2 = 140 nm and different lower level ligament size L_1. (a) L_1 < 20 nm; (b) L_1 = 20 nm and (c) L_1 = 40 nm. 43

4.3 Results of uniaxial loading/unloading compression test of 4 representative HNPG samples with different L_2 varying from 60 nm to 180 nm and approximate initial solid volume fractions of 0.144, 0.142, 0.141 and 0.142, respectively. (a) Engineering stress-strain curves (σ - ε_{eng}). The zoomed image shows a loading/unloading segment; (b) The log-linear plot of Young's modulus Y as a function of engineering strain ε_{eng}; (c) Elastic Poisson's ratio (ν_{E}) as a function of engineering strain (ε_{eng}) and (d) Plastic Poisson's ratio (ν_{P}) as a function of ε_{eng}. The error bars represent the standard deviation, which are the max and min values of measured ν_{E} and ν_{P} during each elastic and plastic deformation stage. . 44

4.4 The log-linear plot of HNPG's Y as a function of the φ_{net} at different compressive strains. The four HNPG samples have an approximately same initial φ_{net} = 0.142 and L_2 vary from 60 nm to 180 nm. 45

4.5 The variations in the ν_{E} of HNPG with different L_2 as a function of φ_{net} evolution are presented. (a), (b), (c) and (d) ν_{E} for HNPG samples with L_2 ranging from 60 nm to 180 nm. The yellow-shaded region in each figure represents the spread of ν_{E} for at least 10 samples, with the upper and lower boundaries defined by the maximum and minimum values at the corresponding φ_{net}. Additionally, the ν_{E} of a representative sample is included within each shaded region. The error bars represent the standard deviation, which are the max and min values of measured ν_{E} during each elastic deformation stage. 47

4.6 The variations in the ν_{E} of HNPG with different L_2 as a function of φ_{net} evolution from Figure 4.5 are presented together. 48

4.7 The variation of the elastic Poisson's ratio ν_{E} during compression. (a), (b), (c) and (d) ν_{E} versus engineering strain ε_{eng} for HNPG samples with L_2 sizes ranging from 60 nm to 180 nm. The yellow-shaded region in each figure represents the spread of ν_{E} for at least 10 samples, with the upper and lower boundaries defined by the maximum and minimum values at the corresponding ε_{eng}. Additionally, the ν_{E} of a representative sample is marked as open symbols within each shaded region. The error bars on open symbols represent the standard deviation, which are the max and min values of measured ν_{E} during each elastic deformation stage. 49

4.8 The variations of the ν_P of 4 representative HNPG samples with different L_2, ranging from 60 nm to 180 nm and approximate initial φ_{net}, are shown as a function of φ_{net}. The error bars represent the standard deviation, which are the max and min values of measured ν_P during each plastic deformation stage. 50

4.9 The variation of the plastic Poisson's ratio ν_P during compression for hierarchical nanoporous gold with $L_2 = 140$ nm and $L_1 < 20$ nm (green triangles), 20 nm (black squares) and 40 nm (blue circles). (a) ν_P vs. engineering strain ε_{eng}; (b) ν_P vs. net solid fraction φ_{net}. Data points include error bars (one standard deviation) for each series. 50

4.10 Average values of ν_E, ν_P, Y and φ_{eff} at 10% ε_{eng} as a function of L_2. (a) ν_E; (b) ν_P; (c) Y and (d) φ_{eff}. φ_{eff} is calculated from the Y using Eq. 4.2. Each data point represents the average value of at least 10 HNPG samples, with an error bar showing the max and min values. . . 51

4.11 Scaling behavior of ν_E with respect to φ_{net} of nanoporous gold with different numbers of hierarchical levels. Close symbols: Literature experimental data, which were obtained from microscale NPG samples using compression testing [16, 149], tensile testing [20, 149] and ultrasonic testing techniques [166] and from compression tests on millimeter-sized NPG samples [27, 28, 150]. Open symbols: experimental data from compression tests on millimeter-sized HNPG samples in this work. Grey dot line: Gibson-Ashby equation, $\nu_E = 0.33$ [145]. Blue dash line: Soyarslan's law, $\nu_E = D_1 \ln\varphi_{net} + D_2$, where $D_1 = 0.116$, $D_2 = 0.363$ [37]. Red solid lines: Scaling law proposed in this work by Eq. 2.17, with $n = 1$ and $n = 2$, respectively. The error bars for HNPG take the max and min values of measured ν_E for each sample; the error bars for NPG are taken directly from literature. 54

4.12 ν_P of HNPG as a function of φ_{net}, compared to ν_P of NPG from various sources in literature. The error bars for HNPG were obtained from at least 5 samples at ε_{eng} around 10%, indicating the max and min measured values, while the error bars for NPG samples are taken directly from literature. 55

4.13 Microstructure evolution during compression. Molecular dynamics (MD) simulated microstructure of virtual HNPG at a compressive strain of (a) ε_{eng}=0 and (b) ε_{eng} =49% [22], Top: a three-dimensional overview, middle: cross section perpendicular to the compression direction, bottom cross-section parallel to the compression direction. The loading direction is indicated by red arrows. Reprinted with permission from Ref [22]. SEM images of the cross sections (c) parallel and (d) perpendicular to the compression direction of HNPG samples at ε_{eng}=60%. 57

5.1 SEM pictures show the microstructure morphology of np Pd and np PdAu samples. (a) np Pd; (b) np PdAu. 60

5.2 High-angle annular dark-field scanning transmission electron microscopy (HAADF-STEM) images of np Pd and np PdAu samples, revealing the nanoscale bicontinuous ligament structure. (a) np Pd; (b) np PdAu. The high atomic number contrast in HAADF mode enhances the visualization of ligament connectivity and size variations between the two samples. . 61
5.3 X-ray diffraction patterns of the precursor master alloys and the corresponding nanoporous samples. (a) XRD patterns of $Pd_{15}Cu_{85}$ and $Pd_{12.5}Au_{2.5}Cu_{85}$ (at.%) master alloy; (b) XRD patterns of np Pd and np PdAu. 62
5.4 Cyclic voltammograms (CV) and H sorption (a) CV patterns of np Pd (blue) and np PdAu (red) recorded in 1 mol/L H_2SO_4 at a scan rate of 1 mV/s. (b) Net (including surface adsorption plus bulk absorption) hydrogen concentration (x_H) vs. electrode potential (vs. SHE) for np Pd. Regimes of hydrogen under potential deposition (UPD) on the pore surfaces and of bulk hydrogen sorption in the dilute α and concentrated α' phase are marked. Reprinted with permission from Ref [25] 64
5.5 Relation between applied electrochemical potential and equilibrium x_H for np Pd and np PdAu under potentiostatic conditions. x_H were determined independently from electrochemical sorption measurements performed under identical conditions as the mechanical tests. 65
5.6 Mechanical test results and elastic Poisson's ratio (ν_E) vs. hydrogen concentration (x_H) for representative np Pd and PdAu samples with the corresponding engineering strain for the 3 % loading-unloading test. (a) Engineering stress-strain (σ - ε_{eng}) curve for the np Pd sample; (b) σ - ε_{eng} curve for the np PdAu sample; (c) ν_E as a function of x_H for the np Pd sample and (d) ν_E as a function of x_H for the np PdAu sample. 66
5.7 Normalized elastic Poisson's ratio under potentiostatic (fixed-μ_H) conditions, shown as ν_E^μ/ν_0 versus x_H. (a) np Pd; (b) np PdAu. Symbols: experimental unloading-based ν_E obtained from in-situ DIC (same data as in Fig. 5.6). Lines: open-system prediction calculated from Eq. 2.30 using hydrogen-dependent Young's modulus from Ref. [25]. For the purpose of comparison, the measured ν_E is treated as an estimate of ν_E^μ in the near-equilibrium. 67
5.8 Comparison of the normalized open-system elastic Poisson's ratio, ν_E^μ/ν_0, with experimental measurements in the dilute hydrogen regime for np Pd (pink squares) and np PdAu (purple triangles). The theoretical curves were calculated directly from Eq. 5.11, using the hydrogen-dependent Young's modulus reported in Ref. [25] and approximating the closed-system elastic constants by their hydrogen-free values. The curves represent enlarged low-concentration portions of the theoretical predictions shown in Figure 5.7, with $x_H < 0.01$ for np Pd and $x_H < 0.04$ for np PdAu. 69

List of Tables

4.1 Structural parameters of the HNPG samples. 43

5.1 Approximate elemental compositions of np Pd and np PdAu after dealloying, determined by SEM-EDX measurements on fracture surfaces. Values are reported in atomic percent (at.%). The Pd concentration of np Pd is estimated by difference from the reported residual Cu content. 60

List of Abbreviations

Materials and crystal structures

HNPG	Hierarchical nanoporous gold
NPG	Nanoporous gold
NPSG	Nanoporous silver–gold alloy (Ag–Au precursor)
np AuPt	Nanoporous gold–platinum alloy
np Pd	Nanoporous palladium
np PdAu	Nanoporous palladium–gold alloy
np Pt	Nanoporous platinum
fcc	Face-centered cubic

Microscopy and structural characterization

SEM	Scanning electron microscopy
TEM	Transmission electron microscopy
STEM	Scanning transmission electron microscopy
HAADF	High-angle annular dark-field
HAADF-STEM	High-angle annular dark-field scanning transmission electron microscopy
EDX/EDS	Energy-dispersive X-ray spectroscopy
FIB	Focused ion beam
XRD	X-ray diffraction

Mechanical characterization

DIC	Digital image correlation
DMA	Dynamic mechanical analysis

Electrochemistry

WE	Working electrode
RE	Reference electrode
CE	Counter electrode
SHE	Standard hydrogen electrode
CV	Cyclic voltammetry
UPD	Underpotential deposition

Modelling and simulation

MD	Molecular dynamics
KMC	Kinetic Monte Carlo
RVE	Representative volume element

Chapter 1

Introduction

1.1 Background and Motivation

Nanoporous metals have attracted sustained interest in both fundamental research and application-oriented studies over the past decades. This is largely because their bicontinuous nanostructures combine a high surface area with a morphology that can be adjusted, as well as the associated functional responses [1–5]. Significant efforts have been devoted to synthesising these materials, controlling their microstructure, characterising their mechanical properties and optimising their performance. This has been carried out across a wide range of nanoporous metals, including nanoporous gold (NPG) [6], nanoporous palladium (np Pd) [7, 8], nanoporous platinum (np Pt) [9], and other metals. These materials can be fabricated in various forms such as nanoparticles, thin films, foils, wires and monolithic bulk materials. Representative microstructural images of several nanoporous metals, including NPG, np AuPt alloys, np Pd and np Pt, are shown in Figure 1.1. These images highlight their bicontinuous ligament–pore microstructures and the diversity of morphologies accessible via dealloying-based synthesis. In nanoporous metals, the solid phase forms an interconnected network of nanoscale struts, commonly referred to as ligaments, as clearly shown in Figure 1.1.

A distinguishing feature of nanoporous metals is that they can be fabricated as monolithic bulk samples with ligament sizes spanning roughly 5 to 500 nm, while retaining macroscopic integrity at millimeter to centimeter length scales [10, 13–16]. This combination of macroscopic form and nanoscale microstructure enables conventional mechanical testing methods, such as uniaxial compression, to be used to investigate the deformation behaviour, size effects, and surface-influenced mechanics of nanostructured solids. The bicontinuous network of ligaments and pores results in an extremely high surface-to-volume ratio [9], with a significant fraction of atoms residing near surfaces. The coordination and bonding of these atoms differ from those in bulk environments.

Accordingly, monolithic nanoporous metals provide a controllable platform for studying how surface-related stresses modify the effective mechanical response of a bicontinuous network at nanoscale [17–21]. For monolithic NPG, extensive work has shown that elastic modulus and yield strength vary systematically with relative density and microstructural length scale [9, 12, 22–26]. And the Poisson's ratio can also deviate from bulk values depending on topology and surface-related effects [27, 28]. These investigations demonstrate the critical role of nanoscale geometry in defining

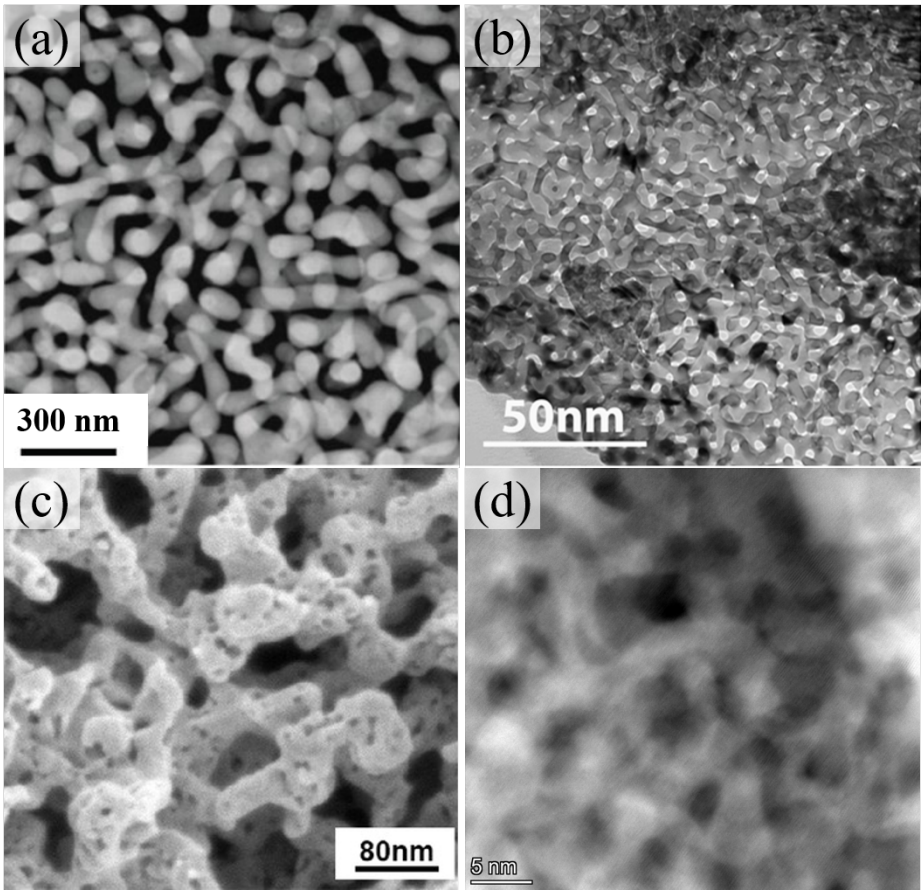


Figure 1.1: Microstructure images of nanoporous metals. (a) Scanning electron micrograph (SEM) of nanoporous gold (NPG); (b) SEM of nanoporous gold platinum alloy (np AuPt); (c) SEM of nanoporous palladium (np Pd) and (d) Transmission Electron Microscopy (TEM) of nanoporous platinum (np Pt). Reprinted with permission from Ref [9–12], respectively.

emergent mechanical properties. They also provide insight into the structure–property relationships of porous metals under mechanical loading.

Among these systems, NPG is one of the most widely studied and best characterized. It can be reproducibly fabricated by dealloying silver-gold (AgAu) alloys, which results in a uniform, crack-free structure. This structure exhibits excellent chemical and mechanical stability. These features make NPG highly suitable for systematic investigations into nanoscale mechanics, including the effects of surface stress, deformation mechanisms and structure-property relationships [10, 28, 29].

At the same time, there is growing interest in expanding beyond Au-based systems to develop nanoporous metals. They offer not only mechanical robustness and structural control, but also additional functional properties. Pd stands out as a particularly promising candidate in this regard. Known for its strong affinity to hydrogen, Pd readily forms stable hydride phases under relatively mild conditions and exhibits considerable volumetric expansion during hydrogen absorption [30–32]. When Pd is processed into a nanoporous structure, it is usually done by dealloying Pd-based precursors, such as Pd–Cu master alloys [8]. The nanoporous Pd retains the tunable morphology and high surface area characteristic of nanoporous metals, while exhibiting

the well-established hydrogen insertion–induced chemo-mechanical behaviour of Pd–H systems. This dual functionality creates new possibilities for investigating hydrogen-induced mechanical phenomena, such as actuation [12] and the elastic softening effects predicted by open-system elasticity theory [25, 33].

Previous studies have primarily focused on the strength and stiffness of nanoporous metals, but much less on Poisson's ratio (ν), even though the Poisson's ratio plays a key role in controlling volumetric strain and deformation behavior [27, 34, 35]. In materials with porous-networked microstructures, ν is not always a fixed constant. Instead, it can vary depending on the geometry of the network [27], such as how the ligaments deform [36–38] and how the structure interacts with its environment [28]. As a result, Poisson's ratio becomes a highly tunable property through variations in network geometry and deformation mechanisms. Similarly, such as nanoporous Pd, solute absorption induces lattice expansion. That also implies that the lateral strain response may depend on the chemical state of the material [39, 40].

However, two knowledge gaps remain. First, while scaling laws for stiffness and strength in nanoporous networks are well established [22, 41], a quantitatively validated framework for Poisson's ratio—especially in hierarchical networks with multiple ligament length scales—is still lacking. Second, experimental measurement on open-system elastic constants is reported [8], and direct measurement of an open-system Poisson's ratio under controlled chemical potential has remained particularly limited. Therefore, this thesis investigates Poisson's ratio in two materials systems.

1. **Hierarchical nanoporous gold.** Structure hierarchy is employed as a purely structural design strategy in which multiple characteristic ligament length scales are incorporated within a single nanoporous network. Hierarchical nanoporous gold (HNPG) serves as a model system to isolate structure effects. By systematically varying the hierarchy, HNPG enables a direct investigation of how network geometry across different length scales influences deformation mechanisms and, consequently, both the elastic and plastic Poisson's ratios.

2. **Nanoporous palladium-hydrogen.** Chemically active nanoporous systems are examined using nanoporous palladium. In this material, the absorption and desorption of hydrogen induces lattice strain and modifies the elastic response, raising the possibility of actively tuning the mechanical behaviour. In particular, potentiostatic control provides a route to probe unloading-based elastic Poisson's ratios under near-equilibrium conditions, which can be interpreted within the Larché–Cahn open-system framework and compared quantitatively to theoretical predictions. This chemo-mechanical coupling is interpreted within the Larché–Cahn open-system elasticity, which describes the interaction between mechanical stress and solute redistribution under fixed chemical potential [39].

This dissertation therefore develops complementary, experimentally grounded routes to tailor Poisson's ratio: structure hierarchy and environment-tuning via hydrogen absorption.

1.2 Dealloying-made nanoporous metals

Dealloying is a selective dissolution process in which one or more reactive elements are removed from an alloy, leaving a porous framework of the nobler components behind [42, 43]. Chemical or electrochemical dealloying methods have been widely employed to fabricate nanoporous metals. These methods can be used to build structures with the features of bicontinuous, sponge-like structures with interconnected pores and ligaments [17, 18, 44, 45].

One of the major advantages of dealloying is the ability to control the size of the ligaments and pores. These can be systematically varied by adjusting synthesis parameters such as electrode potential [46, 47], electrolyte [48], temperature [49] and the post-dealloying process [22, 50] for details on thermal annealing duration and temperature. These structures span a wide range of characteristic length scales, from just a few nanometers up to several micrometers, depending on processing and coarsening conditions in the dealloying process [51]. For example, Liu et al. demonstrated that electrochemical reduction of as-dealloyed NPG increased ligament size from 15 nm to 45 nm, while annealing at 200 °C-500 °C coarsened ligaments further from 54 nm to 548 nm [52].

The typical ligament size of nanoporous metal, such as the standard NPG, is around 40 nm [53]. However, recent efforts have focused on reducing this scale even further, such as nanoporous Au-Pt alloys with smaller ligament sizes down to 5 nm [11] and nanoporous Pt with ultra fine features around 2 nm [9] have been reported. This trend toward finer feature sizes is largely motivated by the associated increase in surface area. A larger surface area is undoubtedly advantageous for many functional applications. Materials with finer ligaments which provide abundant active sites, allowing stronger surface-mediated interactions. As a result, nanoporous metals are actively explored in areas like catalysis [54], chemical sensing [55], supercapacitors [56] and actuation [11]. Their open, porous structures allow for efficient mass transport and maintain mechanical integrity, making them ideal for a variety of nanoscale technologies.

Nevertheless, new challenges can be introduced by over-fined nanostructures. As the ligament size decreases, the pore size also decreases sharply. Then the mass transport through the structure may be significantly hindered, limiting the accessibility of reactants or ions to active sites and increasing diffusion resistance [57–60]. In addition, extremely fine microstructures can be difficult to process. In material systems, balancing nanoscale reactivity with structural robustness and transport efficiency remains a key challenge. These trade-offs have led to a growing interest in hierarchical microstructures that incorporate ligament sizes. By combining both coarse and fine features within a same material, the hierarchical porous structures can enhance both transport properties and mechanical robustness. And it can still providing high surface area for functional performance. One notable example is HNPG, in which a coarse ligament network is overlaid with a fine-scale secondary hierarchy level structure [50, 61]. This multiscale configuration not only improves charging kinetics but also provides a tunable platform for investigating both functional and mechanical behavior across length scales.

Recent studies have demonstrated that HNPG enables systematic exploration of how stiffness and strength scale with density and hierarchical microstructure [22]. These findings offer new insights into the mechanics of hierarchical solids. Such hierarchical

nanoporous metals, including HNPG [50, 62], hierarchical nanoporous platinum [63], palladium [12, 64, 65], copper [66] and nickel [67], have attracted significant attention due to their ability to combine large surface areas with efficient mass transport pathways.

The hierarchical microstructures are generally achieved through either (i) multi-step dealloying of single-phase alloys or (ii) single-step dealloying of multiphase alloys [64, 65, 67, 68]. For example, Qi et al. synthesized HNPG with two distinct ligament sizes by a dealloying–coarsening–dealloying route starting from $Ag_{90}Au_{10}$ alloys [50] while Li et al. synthesized hierarchical nanoporous copper by one-step dealloying from $Al_{75}Cu_{25}$ alloys [68]. Representative micrography of HNPG and copper structures are shown in Figure 1.2, illustrating the multiscale microstructure accessible via both multi-step and one-step dealloying routes.

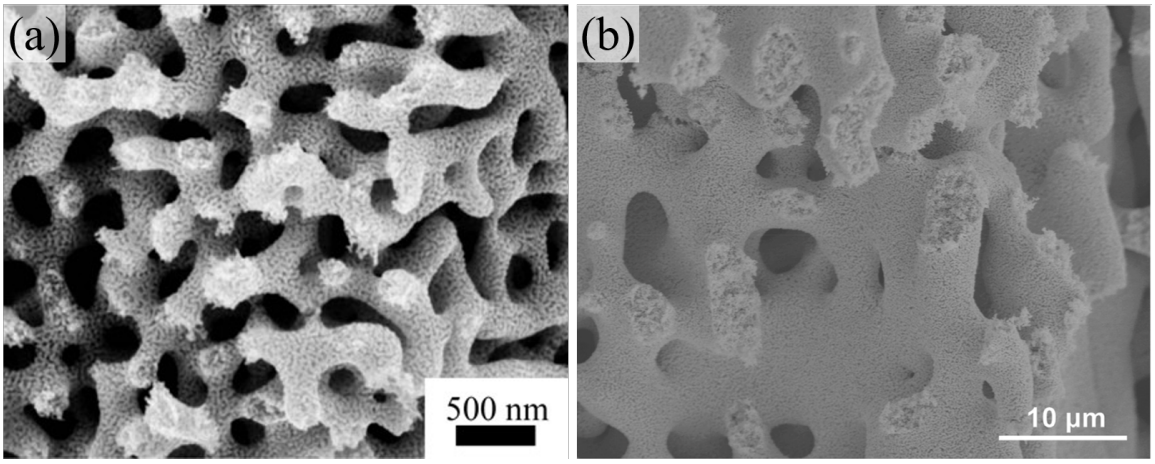


Figure 1.2: Microstructure images of hierarchical nanoporous metals. (a) SEM of hierarchical nanoporous gold fabricated via a dealloying-coarsening-dealloying method; (b) SEM of hierarchical nanoporous copper fabricated by one-step dealloying. Reprinted with permission from Ref [50, 68], respectively

Overall, both chemical and electrochemical dealloying are well-established and controllable methods for producing high-quality monolithic nanoporous noble metals, especially in gold-based systems. In this context, np Pd are prepared using similar dealloying approaches serve as chemically responsive model systems with well-defined microstructures and mechanical integrity. These materials provide an important alternative to NPG for exploring nanoscale mechanics, open-system elasticity and chemo-mechanical coupling [8, 12, 25, 64, 65].

1.3 Poisson's Ratio in nanoporous metal

Poisson's ratio (ν) is a fundamental mechanical property that quantifies the amount of lateral contraction or expansion of a material. It's a key parameter which describes the coupling between axial and transverse deformation under load shows how materials deform under stress.

For most conventional isotropic solid materials, ν changes within the range from 0 to 0.5. 0 (like cork or some polymer foams) represents no lateral deformation during

axial deformation and 0.5 (like rubber or a perfectly incompressible elastic material) represents it deforms at a constant volume. Besides, the mechanically stable isotropic elasticity permits a broader range (-1 to 0.5), which includes auxetic behavior. In addition, some nested or porous materials exhibit negative Poisson's ratios, known as auxetic materials [69–71], and offer enhanced mechanical properties such as increased hardness, strength and impact resistance [72–74]. When compressed axially, it expands laterally as much as possible without changing its total volume [74, 75]. ν is also closely related to many other material properties, such as thermal expansion [76–80], acoustic behavior [81–83] and fracture toughness [84–86]. For example, in materials which are used for thermal insulation or acoustic damping, the lateral deformation governed by ν can significantly affect their performance. This makes ν a critical design parameter that need to be considered in various fields, including bridge construction [87–89], aircraft components [90] and biomechanics [91, 92].

Poisson's ratio also provides insight into the mechanical behaviour of materials at the nanoscale, which is significant for optimising the performance of materials in mini devices [93–95]. Understanding how ν varies with structure size and solid volume fraction (φ) expands the design space for nanoporous materials with tailored mechanical response. Moreover, accurate prediction of mechanical behavior in nanoporous networks often requires explicit consideration of ν in numerical simulations. For example, in finite element modeling, it influences stress distributions and deformation patterns [96, 97]. This is particularly important for nanoscale materials, as their microstructure and hierarchical structure significantly influence their mechanical response while also enabling strong coupling effects with chemical or physical fields. Furthermore, ν is essential for calculating multiscale stresses, thermal shock parameters and other performance metrics [36, 98, 99].

NPG, fabricated via electrochemical or chemical dealloying as discussed above, has become a model system for investigating structure–property relationships in porous solids. In particular, its bicontinuous nanoscale ligament–pore network provides a well-defined microstructural framework in which key parameters. Such as ligament size, solid volume fraction and network topology can be systematically varied. This enables direct correlation of microstructural features with mechanical properties, including stiffness, strength and Poisson's ratio [23, 27, 28].

Beyond unimodal NPG, nanoporous metals with hierarchical structures have gained increasing attention over the past decade, since the larger pore channels improve mass transport while the smaller pores ensure the sufficient surface area [100, 101]. Recent studies have shown that HNPG allows ligament sizes at different hierarchical levels to be tuned with a high degree of independence, allowing systematic investigation of how stiffness and strength scale with density and microstructure [22]. Jeon et al. also reported that HNPG exhibits significantly improved electrochemically tunable mechanical properties compared to NPG at equivalent solid fraction [100] and Riedel et al. showed that structural parameters at both hierarchy levels can be tuned independently [102].

As mentioned before, Poisson's ratio in hierarchical porous networks has received comparatively less systematic attention. Since the reliable experimental methodologies for measuring ν in nanoporous metals have already been established, notably through the work of Lührs and co-workers, who demonstrated quantitative determination of

both elastic and plastic Poisson's ratios using well-controlled mechanical testing and strain analysis [27, 28]. So with these established approaches, the remaining gap lies not in experimental feasibility but in understanding how structure hierarchy influences ν across multiple length scales. In particular, while scaling laws have been successfully developed for stiffness and strength in HNPG [22], analogous works for ν are still lacking. Elucidating this relationship is essential for predictive modeling and rational design of hierarchical porous materials. This motivates us to extend existing scaling equations to the deformation behavior.

Structural hierarchy provides one effective route for tuning ν in nanoporous metals, as demonstrated by HNPG. The changes of ν in HNPG arise from geometry-dependent deformation mechanisms across multiple length scales. In such systems, ν is controlled by network microstructure, including ligament connectivity, bending modes and the interaction between hierarchical levels. In np Pd, hydrogen absorption and desorption lead to solute redistribution within the solid network, coupling mechanical deformation to chemical potential. According to Larché–Cahn open-system elasticity, stress-assisted solute redistribution can, in principle, lead to strong composition-dependent changes in the effective elastic constants under fixed chemical potential. The theory predicts pronounced softening of the open-system modulus and a substantial modulation of Poisson's ratio, especially near thermodynamic instabilities. In practice, the experimentally accessible tuning range is constrained by phase stability and by the requirement of near-equilibrium conditions.

Two features make this "open-system" route distinctive in the present context. First, the modulation of Poisson's ratio is reversible under electrochemical control, whereas architected or metamaterial-based tuning is typically fixed once fabricated. Second, within the PdAu-H system studied here, the change in Poisson's ratio can be large and continuous over the experimentally accessible single-phase composition window.

These distinctions highlight that Poisson's ratio in nanoporous metals can be tuned through two fundamentally different pathways:

(i) structural hierarchy, where ν evolves due to microstructure-controlled deformation mechanisms, and (ii) chemo-mechanical coupling in open systems, where ν changes as a consequence of stress-driven solute redistribution.

Motivated by this contrast, the following chapters systematically investigate Poisson's ratio in dealloyed nanoporous metals, focusing on hierarchical gold structures and hydrogen-responsive palladium-based alloys. Both the elastic and plastic Poisson's ratios are examined to elucidate how nanoscale microstructure and environmental coupling shape volumetric mechanical response.

Effects of microstructure on Poisson's ratio in nanoporous materials:

For isotropic materials, the introduction of nanoscale porosity significantly alters their effective elastic response. In nanoporous metals, the effective Poisson's ratio (ν_{eff}) is defined as a macroscopic, structure-averaged quantity that relates the transverse and axial strains of the porous network under external loading. Unlike the intrinsic Poisson's ratio of the solid material, ν_{eff} reflects the collective deformation of the ligament. As a result, ν_{eff} can differ markedly from the bulk value due to pore morphology, ligament geometry and network topology. The presence of pores breaks translational symmetry and promotes deformation mechanisms such as bending, buckling and shear. Consequently, ν_{eff} becomes highly sensitive to relative density, anisotropy and nanoscale

microstructure.

Experimental studies have reported a broad range of ν_{eff} in nanoporous metals, reflecting differences in ligament arrangement and deformation mode [27]. Complementary computational work has shown that elastic properties of porous networks, including ν, depend sensitively on network topology and connectivity [103]. Depending on whether deformation is dominated by bending or stretching of the ligaments, the effective Poisson's ratio can differ substantially from the bulk value of the parent material. In addition, nanoporous materials with concave or chiral network topologies may exhibit a negative Poisson's ratio ($\nu < 0$), expanding laterally under tensile loading [104]. These observations demonstrate that Poisson's ratio in porous solids is an emergent property governed by mesoscale microstructure rather than a direct inheritance from the constituent material.

Chemo-mechanical coupling:

Mechanical deformation can also interact with solute redistribution. This effect is described by the open-system elasticity framework developed by Larché and Cahn [39]. In this theory, the material is treated as an open thermodynamic system in contact with a solute reservoir, such that the chemical potential of the solute is fixed during mechanical loading.

In hydrogen-containing palladium-based systems, hydrogen absorption induces lattice expansion and introduces a composition-dependent strain. Under open-system conditions, an applied stress can drive local redistribution of hydrogen within the solid. This redistribution relaxes part of the elastic strain energy and leads to a reduction of the apparent elastic stiffness. As a consequence, the effective elastic response differs from that of a closed system with fixed composition. In np Pd and PdAu, this manifests as a hydrogen-dependent Young's modulus, as demonstrated experimentally by Shi *et al.* [25]. Because Poisson's ratio is determined by the relative values of elastic moduli, changes in the open-system Young's modulus can also lead to a variation in the effective elastic Poisson's ratio under hydrogen loading.

1.4 Larché–Cahn Open-System Elasticity

Mechanical behavior in many modern material systems cannot be fully described by classical elasticity, which assumes a closed system with fixed composition during deformation. By contrast, many technologically relevant materials, such as battery electrodes and hydrogen storage alloys exhibits open-system behaviour. The solute species (e.g., H, Li or O) can redistribute in response to local stress [105–107]. The coupling between mechanical strain leads to fundamentally different elastic responses. And it enables novel phenomena such as stress-induced diffusion, phase transformation and energy dissipation [108–110].

Related examples of stress–composition coupling include martensitic transformations in steels, where solute atoms are trapped in a distorted lattice, enhancing strength and hardenability [111]. In the nickel-based superalloy, elastic stress alters solute diffusion during precipitation, thereby controlling microstructural evolution and mechanical performance at elevated temperatures [112–114]. Similarly, in electrode materials such as silicon and palladium. The insertion of lithium or hydrogen can cause massive lattice expansions which can reach 300% in silicon and 10% in Pd-H. That will generate

internal stress fields that feed back into solute transport [109, 110, 115]. These chemo-mechanical couplings can degrade performance during cyclic operation, but also present opportunities for actuation or tunable mechanics.

A major milestone in understanding stress–solute interactions was the model proposed by Larché and Cahn in 1973, which unified elasticity and thermodynamics into a single open-system framework [39]. Their theory introduced the concept of "open-system elastic constants", which is defined under conditions of constant chemical potential rather than constant composition. This shift in thermodynamic conditions alters the effective stiffness and other mechanical responses. Under open-system conditions, part of the mechanical stress is relieved by solute redistribution, resulting in an effective softening of the elastic modulus. The theory predicts that elastic coefficients can vary significantly with solute concentration and become especially sensitive near phase boundaries or critical points [116–119].

Despite extensive theoretical study [116, 120–122], direct experimental verification of open-system elastic constants has remained limited. In nanoporous metals, however, this challenge becomes more tractable. Their high surface-to-volume ratios and short diffusion paths allow fast equilibration of solute concentration with external reservoirs. These features make it feasible to probe mechanical properties under true constant chemical potential conditions. For instance, recent work on hydrogen sorption nanoporous Pd has demonstrated composition-dependent stiffness consistent with Larché–Cahn predictions [12, 64, 123, 124].

Moreover, the so-called "Gorsky effect", a delayed strain relaxation resulting from stress-driven solute diffusion, has been observed in metal–hydrogen systems and provides indirect evidence for this coupling [125–128]. While traditionally used to estimate hydrogen diffusivity from relaxation times [115, 129], this effect also underscores the need to account for time-dependent, solute-mediated strain responses in materials with mobile interstitials.

The defining characteristic of open-system elasticity is the requirement that solute atoms redistribute sufficiently fast in response to stress-induced gradients in chemical potential. In bulk solids, diffusion is typically too slow for the system to reach local chemical equilibrium on the timescale of mechanical loading. In contrast, the diffusional equilibration time ($\tau_{\text{diff}} \sim L^2/D$) in nanoporous metals is controlled by the ligament size L, and D is the bulk diffusion coefficient of the solute. For hydrogen in Pd, $D \sim 10^{-11}\,\text{m}^2/\text{s}$ at room temperature [115], implying sub-millisecond equilibration for ligament diameters of tens of nanometers. However, the effective equilibration time may also depend on surface exchange and microstructural connectivity. These timescales are orders of magnitude shorter than those associated with typical dynamical mechanical analysis (DMA) frequencies (1-10 Hz). Therefore, nanoporous Pd-based networks offer favorable length and time scales for approximating the local-equilibrium assumption underlying Larché–Cahn open-system elasticity, provided that the experiments are conducted under sufficiently slow loading and adequate potential-hold times. Nanoporous metals thus provide an experimentally accessible setting, provided that diffusion equilibration is fast compared with the mechanical loading timescale. Based on this, open-system elastic responses can be investigated under electrochemically controlled chemical potentials, enabling a quantitative comparison with Larché–Cahn-type predictions.

In the context of this dissertation, Larché–Cahn open-system elasticity provides the

theoretical foundation for interpreting how hydrogen alters the ν of nanoporous Pd and PdAu. The coupling between chemical composition and stress directly impacts ν under loading, offering a route to understand modulate ν through electrochemical control. For instance, reversibly tuning ν of np Pd and its alloys through electrochemical controlled hydrogen absorption/desorption to be explored in this thesis.

1.5 Outline of the Thesis

This thesis is structured as follows.

Chapter 1 introduces the motivation, background, and scope of this thesis.

Chapter 2 provides a theoretical foundation for understanding the mechanics of nanoporous metals. It begins with the thermodynamic and kinetic principles of electrochemical dealloying, before moving on to models of ligament coarsening and scaling laws relating elastic properties to relative density. This chapter then reviews ν in porous network materials, addressing its structure sensitivity and its significance in relation to nanoscale deformation. Finally, it introduces the Larché–Cahn theory of open-system elasticity to describe stress–composition coupling in materials with mobile solutes.

Chapter 3 provides details of the experimental methods employed in this study. It covers the preparation of master alloys and their transformation into nanoporous structures via electrochemical dealloying. It also outlines the techniques used for structural and compositional characterization, including scanning electron microscopy (SEM), energy dispersive X-ray spectroscopy (EDX/EDS), transmission electron microscopy (TEM) and X-ray diffraction (XRD), as well as the procedures for mechanical testing under uniaxial compression. Particular focus is given to digital image correlation (DIC), which is employed for measuring full-field strain and evaluating ν.

Chapter 4 focuses on the scaling behaviour of ν in HNPG. The first part presents microstructural and mechanical data for samples with different ligament sizes and levels of hierarchy. The second part interprets these results within the framework of multiscale network mechanics, emphasizing the deviation from classical scaling models. The chapter demonstrates how hierarchical microstructure enables control over the elastic and plastic Poisson's ratios.

Chapter 5 examines the tunability of Poisson's ratio in np Pd and np PdAu under hydrogen absorption. The first part presents the results of in-situ mechanical testing and electrochemical cycling, highlighting reversible changes in elastic behavior. In the second part, these observations are discussed in the context of Larché–Cahn open-system elasticity, with comparisons between theory and experiment.

Chapter 6 summarizes the key findings of this thesis and discusses their broader implications for tunable elasticity in nanoscale materials. An outlook is provided on future directions, including potential extensions to other material systems and functional applications.

Chapter 2

Theoretical Fundamentals

This chapter establishes the theoretical foundations necessary to interpret the structural and mechanical behavior of the nanoporous metals examined in this dissertation. The discussion begins with the thermodynamic and kinetic principles of dealloying, which govern the formation of bicontinuous nanoporous microstructures (Sec. 2.1). These self organized networks often exhibit mechanical responses that deviate from classical expectations. For example, nonlinear elasticity and anomalous Poisson's ratios (ν) which are addressed through both conventional definitions and modern characterization strategies (Sec. 2.2).

To understand how elastic properties scale with porosity and network geometry, this chapter introduces classical scaling laws together with their extensions for hierarchical materials (Sec. 2.3). In addition, this chapter presents the theoretical framework of open-system elasticity (Sec. 2.4), which accounts for solute–stress coupling and is directly relevant to hydrogen–metal interactions in nanoporous Pd-based systems studied in the later chapters.

2.1 Fundamentals of dealloying

This thesis focuses on electrochemical dealloying, which can be controlled more precisely by adjusting the applied potential, electrolyte chemistry and dealloying temperature. Compared to chemical dealloying, it provides greater reproducibility, more uniform structures and greater flexibility and additional control parameters (potential window, scan rate and electrolyte anion effect). These advantages are particularly significant when synthesizing hierarchical microstructures and coupling dealloying with in situ experiments, such as hydrogen charging/discharging during mechanical tests.

2.1.1 Thermodynamic and electrochemical prerequisites

Dealloying fundamentally requires that the less noble component be thermodynamically prone to oxidation under the given electrochemical conditions. For a redox couple $\mathrm{M} \rightleftharpoons \mathrm{M}^{z+} + z\,e^-$, the equilibrium electrode potential is governed by the Nernst equation [130]:

$$E = E^\circ + \frac{RT}{zF} \ln \frac{a_{\mathrm{M}^{z+}}}{a_{\mathrm{M}}} \tag{2.1}$$

where E° is the standard electrode potential, R is the gas constant, T is the temperature, F is Faraday's constant, z is the number of transferred electrons and a is the activities of the ionic and metallic species. In practice, dealloying proceeds when the applied potential exceeds the local Nernst potential for the less noble element and provides sufficient kinetic driving force to overcome surface passivation. This condition depends not only on the intrinsic redox properties of the alloy components, but also on the electrolyte composition and local concentration gradients that develop during corrosion [131].

The total amount of less noble metal elements removed during dealloying can also be calculated and controlled by Faraday's law of electrolysis:

$$Q = n \cdot F \cdot z \tag{2.2}$$

where Q is the total charge passed, n is the amount (in moles) of less noble metal elements dissolved and z is the number of electrons transferred per atom. This equation is routinely used in experiments to estimate the degree of dealloying, particularly for calculating the residual composition of porous materials based on anodic charge integration values. Accurate application requires correction for parasitic currents and side reactions that may contribute to the total measured charge [42, 132].

2.1.2 The parting limit: connectivity versus kinetics

The concept of the parting limit was first introduced by Tammann in 1919 [133]. In a binary alloy system, it represents the minimum atomic fraction of the less noble (more electrochemically active) component required for continuous or bulk dealloying to proceed under given environmental conditions. When the concentration of the less noble metal falls below this critical threshold, selective dissolution ceases or becomes self-passivating due to the rapid enrichment of the more noble component at the solid–electrolyte interface. As a result, the corrosion or porosity develops only locally where typically near the surface rather than penetrating through the bulk alloy.

Over the past century, many studies have been attempted to identify and explain the origin of the parting limit through experimental and computational methods. Early theoretical interpretations linked it to the geometrical site percolation threshold of the alloy lattice [134]. This framework holds particularly well for systems with a large difference in electrochemical nobility between the constituent elements. For instance, Sieradzki and co-workers reported that the experimentally determined sharp parting limits in ZnCu/ZnAl alloys closely coincide with the respective site percolation thresholds in fcc lattices [135, 136].

However, in alloy systems such as AgAu, the experimentally observed parting limit deviates significantly from the simple geometrical site-percolation threshold. In the AgAu system, the experimentally determined critical composition for dealloying is approximately 55 at% Ag, whereas the fcc site-percolation threshold is about 0.19–0.20 [134]. To explain this discrepancy, Sieradzki et al. in 1989 proposed a layer-by-layer dealloying mechanism derived from high-density percolation theory [136]. They employed Kinetic Monte Carlo (KMC) simulation techniques to simultaneously account for the dissolution of lower-precious-metal elements and the surface diffusion of higher-precious-metal elements in a two-dimensional binary alloy system. This approach yielded two key findings:

1. When dissolution occurs even at highly coordinated lattice sites (e.g., terrace atoms), the computed parting limit approaches that of ZnCu-type alloys, nearly coinciding with the site percolation threshold.

2. When dissolution is restricted to low-coordination sites (excluding terraces), the predicted limit shifts toward the experimentally observed threshold of AgAu-type systems.

The simulations also revealed that the mobility of the noble component could influence the calculated parting limit. However, this two-dimensional step-by-step model was later deemed incomplete, as experimental evidence indicated that selective dissolution in AgAu alloys must initiate from step sites.

Subsequent three-dimensional KMC simulations have provided a more realistic description of pore evolution and parting behavior during dealloying such as the MESOSIM framework developed by Erlebacher and co-workers [42, 132]. Assuming Ag atoms cease dissolving when their coordination number at the interface exceeds 9, and neglecting diffusion at the Au surface, the model predicts a separation limit of approximately 58.4 at% Ag in the AgAu system. This value is close to the experimentally reported threshold (~55 at%) and to the high-density percolation limit (~60 at%) obtained under similar kinetic assumptions. Incorporating Au surface diffusion into the simulations slightly modifies but does not substantially alter the predicted parting limit, confirming the robustness of the result.

Taken together, these findings suggest that the parting limit arises from a complex interplay between geometrical connectivity of the dissolving species and kinetic barriers imposed by noble metal redistribution. For alloys with large chemical potential contrast, the limit is well described by percolation theory. For systems like AgAu, interfacial kinetics dominate and shift the threshold well above the geometric. In either case, the parting limit imposes a fundamental constraint on alloy design for dealloying-based synthesis and must be carefully considered in the selection of precursor compositions.

2.1.3 Critical dealloying potential and polarization behavior

Even the precursor composition exceeds the parting limit, dealloying will not proceed, unless the electrochemical driving force is sufficiently large to overcome surface-smoothing effects driven by the surface diffusion of noble metal. The critical dealloying potential (E_c) is defined as the minimum applied electrode potential at which sustained bulk dealloying occurs. Below this applied potential, passivation due to noble-element enrichment dominates, and only limited surface roughening may take place.

In experiment, E_c is typically identified from potentiodynamic polarization curves. It exhibits three distinct regimes as the potential is swept anodically: (i) a low-potential passivation region with negligible current, (ii) a sharp rise near the critical potential indicating the onset of active dissolution and (iii) a high-potential selective-dissolution regime characterized by significant current flow.

Although the specific dissolution and passivation mechanisms depend on the intrinsic chemistry of a given alloy–electrolyte system, the operational definition of a critical dealloying potential from anodic polarization behavior is general. Figure 2.1 illustrates a representative anodic polarization response for a binary alloy undergoing

selective dissolution, adapted from the work of Sieradzki *et al.* [131]. At low applied potentials, the current remains small and dealloying is suppressed by surface passivation or noble-element enrichment. Upon increasing the potential beyond a critical value E_c, a sharp rise in anodic current marks the onset of sustained selective dissolution and bulk dealloying. In addition to the potential-based criterion, the onset of sustained dealloying can also be described in terms of a characteristic current density. A minimum anodic current density on the order of $i_{crit} \sim 1\,mA/cm^2$ is typically required to maintain continuous dissolution of the less noble component and prevent complete surface passivation [42, 131]. Below this threshold, dissolution is too slow to overcome surface enrichment of the noble element, leading to passivation and suppression of bulk dealloying. Above this threshold, the dissolution rate exceeds the rate of surface diffusion and reorganization, enabling the development of a bicontinuous porous structure. This empirical current-density criterion is consistent with the sharp increase in anodic current observed at E_c in polarization measurements.

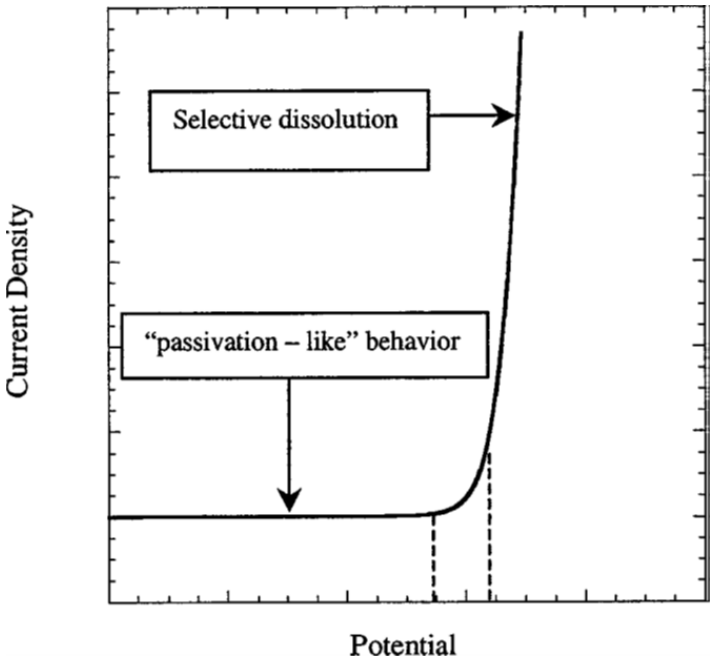


Figure 2.1: Schematic illustration of an anodic polarization curve for a binary alloy undergoing electrochemical dealloying. The transition from passivation-like behavior to sustained selective dissolution defines the critical dealloying potential E_c. Reprinted with permission from Ref [131].

The absolute value of E_c depends on factors such as alloy composition, electrolyte chemistry and temperature. This qualitative polarization profile is characteristic of a wide range of dealloying systems, including AgAu and CuPd alloys. Here, the schematic curve is used solely to illustrate the operational identification of the critical dealloying potential, rather than to compare quantitative values across different material systems.

2.1.4 Mechanistic models of porous-network formation during dealloying

Several mechanistic descriptions have been proposed to explain the formation of porous networks during dealloying. In the present thesis, dealloying is primarily treated as a synthesis route rather than a topic of mechanistic debate; therefore, we focus on the model which is most widely used to explain bicontinuous ligament–pore morphologies, namely the KMC model introduced by Erlebacher and co-workers [42]. This percolation-enhanced, terrace-site dissolution model is also known as the Erlebacher model.

Erlebacher model combines selective dissolution with rapid surface diffusion and explicitly accounts for dissolution at both low-coordination (step/edge) and higher-coordination (terrace) sites. The key factor is the formation of step vacancies. These vacancies can generate vacancy clusters and continuously create new low-coordination environments, thereby sustaining the advancement of the corrosion front [42, 51]. Within this picture, porous-network formation proceeds through the following sequence:

1. Preferential dissolution initiates at low-coordination surface sites.
2. Terrace vacancies are created; noble atoms diffuse rapidly and aggregate into clusters (islands).
3. The evolving vacancy/island morphology continuously exposes fresh, low-coordination sites, enabling a self-propagating dissolution front.
4. Undercutting of metallic connections yields a three-dimensional bicontinuous ligament–pore network, whose characteristic spacing reflects the early-stage island distribution.

KMC simulations based on this framework reproduce several experimentally observed features in dealloying systems, including: (i) the existence and magnitude of the parting limit in AgAu alloys, (ii) a critical potential for sustained bulk dealloying and (iii) the spontaneous emergence of ligament–pore morphologies consistent with experiments [42, 51, 132]. This framework provides a physical basis for using dealloying as a controllable route to generate the bicontinuous nanoporous microstructures studied throughout this thesis.

2.1.5 Morphology evolution and coarsening

After a bicontinuous porous network is established during dealloying, the ligament and pore sizes continue to evolve through curvature-driven coarsening. In nanoporous metals, this process is commonly governed by surface diffusion, because the characteristic length scales are small and the surface-to-volume ratio is high. Under the assumption that surface diffusion is the dominant mass-transport mechanism, the classical Mullins theory predicts that the characteristic length scale L increases with time t according to the power-law relation [137, 138]:

$$L(t) \propto t^{1/4}$$

Rather than focusing on the exact time exponent in individual experiments, many studies on nanoporous gold have examined the underlying transport mechanism that

controls coarsening. A widely used approach is to analyze the temperature dependence of ligament growth and to extract an activation energy for the coarsening process. If the measured activation energy is comparable to that for surface diffusion of gold atoms, surface diffusion can be identified as the rate-limiting step.

Such experimental evidence was reported by Jeon *et al.* [139], who studied the thermal coarsening of nanoporous gold produced by dealloying Ag-Au alloys. Figure 2.2 shows an arrhenius-type plot of the logarithm of the ligament size as a function of inverse temperature. The linear dependence indicates thermally activated kinetics, and the extracted activation energy was found to be consistent with surface diffusion of Au rather than bulk diffusion. This result supports the applicability of a surface-diffusion–controlled coarsening picture for nanoporous gold, in agreement with the physical assumptions underlying the Mullins scaling law.

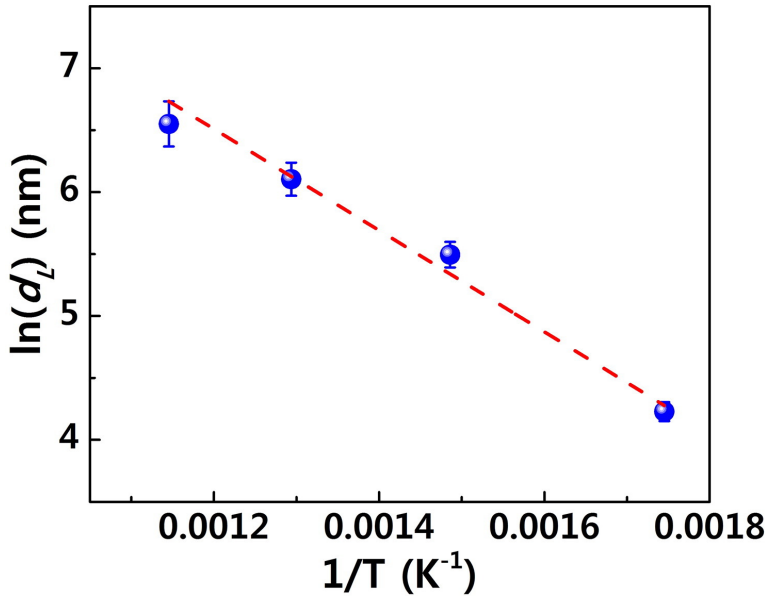


Figure 2.2: Arrhenius plot of the normalized ligament diameter d/L as a function of inverse temperature for thermally coarsened nanoporous gold. The linear behavior indicates thermally activated coarsening kinetics, with an activation energy consistent with surface diffusion of gold atoms. Reprinted with permission from Ref [139].

Thermal annealing therefore provides an effective means to accelerate ligament coarsening and to tune the characteristic length scale of nanoporous gold in a controlled manner. This principle is widely exploited in the design of hierarchical nanoporous structures, where dealloying and annealing steps are combined to introduce multiple ligament length scales within a single network.

2.2 Poisson's Ratio in isotropic linear elasticity

The Poisson's ratio ν quantifies the extent of lateral contraction or expansion experienced by a material in response to longitudinal stress. For infinitesimal strains [27, 34, 35]:

$$\nu = -\frac{\varepsilon_{\text{trans}}}{\varepsilon_{\text{axial}}} \tag{2.3}$$

where $\varepsilon_{\text{axial}}$ (ε_{a}) and $\varepsilon_{\text{trans}}$ (ε_{t}) denote the axial and transverse strains, respectively. A schematic illustration of this relationship is shown in Figure 2.3.

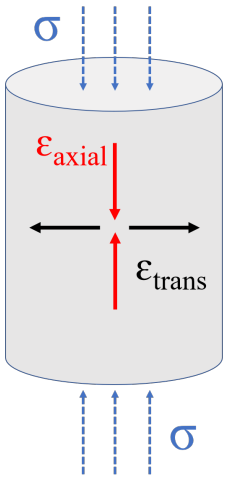


Figure 2.3: Schematic illustration of Poisson's ratio (ν): under stress (σ), the material contracts in the axial direction (with axial strain, $\varepsilon_{\text{axial}}$) and expands in the transverse direction (with transverse strain, $\varepsilon_{\text{trans}}$). ν quantifies this coupling as the negative ratio of transverse to axial strain, $\nu = -\varepsilon_{\text{trans}}/\varepsilon_{\text{axial}}$.

In isotropic linear elasticity, the mechanical response of a material is fully described by two independent elastic constants. Poisson's ratio ν is commonly used as one of these independent parameters and is related to other elastic moduli, such as the Young's modulus Y, shear modulus G and bulk modulus K, through well-defined constitutive relations [140, 141].

$$G = \frac{Y}{2(1+\nu)} \tag{2.4}$$

$$K = \frac{Y}{3(1-2\nu)} \tag{2.5}$$

These relations can be algebraically inverted to yield expressions for ν in terms of Y, G and K [142]:

$$\nu = \frac{Y}{2G} - 1 \tag{2.6}$$

$$\nu = \frac{3K - 2G}{2(3K+G)} \tag{2.7}$$

These expressions emphasize that ν reflects the relative resistance to shape change (through G) and to volume change (through K). In the incompressible limit ($\nu \to 0.5$), the bulk modulus diverges, indicating infinite resistance to volumetric deformation.

It is essential to note that these relationships apply strictly to isotropic materials. For anisotropic solids, such as single crystals or textured polycrystals, the elastic response depends on direction and is described by a higher-order stiffness (or compliance) tensor with more independent elastic constants. In such cases, Poisson's ratio is not a

single scalar value but depends on the chosen loading and transverse directions [141]. Nevertheless, many fcc metals such as Au, Pt and Pd exhibit nearly isotropic elastic behavior at the macroscopic scale. Experimentally measured, orientation-averaged values of ν for these metals typically lie in the range 0.30–0.45 [141, 143].

2.3 Scaling Laws

Scaling laws provide a unifying framework for understanding how the mechanical properties of porous materials emerge from their underlying microstructure. In nanoporous metals where the solid phase forms a continuous nanoscale network. The stiffness/strength and ν are governed not only by the intrinsic properties of the parent metal but also by geometric features such as solid volume fraction, connectivity and hierarchical organization. Because these structural parameters can vary widely during dealloying and coarsening. Instead, scaling laws capture how mechanical properties evolve systematically with porosity and topology, enabling quantitative comparisons across samples with degrees of hierarchy. This makes scaling laws essential for interpreting experimental results, guiding structural design, and linking nanoscale microstructure to macroscopic mechanical response in nanoporous metals. In this section, we will discuss in detail the derivation and principles of the scaling law used in this thesis.

For open-cell porous materials at low solid volume fraction φ, mechanical properties P often follow the Gibson-Ashby scaling law [144]:

$$P = bP_0\varphi^{\beta} \tag{2.8}$$

where P_0 is the property of the solid material and b, β are empirical constants [144, 145]. This framework is effective for describing elastic properties such as Young's modulus and strength in low-density cellular solids with constant connectivity.

However, in random porous structures with connectivity that varies with solid volume fraction and a critical percolation threshold φ_{per}, the original Gibson-Ashby model becomes inadequate. To account for this, Roberts and Garboczi proposed a modified scaling relation [103]:

$$P = P_0 C \left(\frac{\varphi_{\mathrm{net}} - \varphi_{\mathrm{per}}}{1 - \varphi_{\mathrm{per}}} \right)^{m} \tag{2.9}$$

where C and m are material-dependent constants.

In hierarchical network materials geometric similarity at each level (i.e., a nested network [22, 50]), the overall mechanical response P_n arises from contributions at each structural level. Analogous to Eq. 2.9, the property can be expressed as:

$$P_n = P_0 C^n \prod_{j=1}^{n} \left(\frac{\varphi_j - \varphi_{\mathrm{per}}}{1 - \varphi_{\mathrm{per}}} \right)^{m} \tag{2.10}$$

where n denotes the number of hierarchical levels.

Assuming identical solid volume fraction, Eq. 2.10 simplifies to:

$$P_{\mathsf{net}} = P_0\, C^n \left(\frac{\varphi_{\mathsf{net}}^{1/n} - \varphi_{\mathrm{per}}}{1 - \varphi_{\mathrm{per}}} \right)^{mn} \tag{2.11}$$

where P_{net} denotes the mechanical property of an n-level hierarchical network.

This framework has been proposed to describe the effective Young's modulus Y of HNPG [22]. Assuming it also applies to shear modulus G, according to Eq. 2.11, the Y and G of hierarchical porous networks follow:

$$Y_{\mathrm{net}} = C_{\mathrm{Y}}^{n} Y_0 \left(\frac{\varphi_{\mathrm{net}}^{1/n} - \varphi_{\mathrm{per}}}{1 - \varphi_{\mathrm{per}}} \right)^{n m_{\mathrm{Y}}} \tag{2.12}$$

$$G_{\mathrm{net}} = C_{\mathrm{G}}^{n} G_0 \left(\frac{\varphi_{\mathrm{net}}^{1/n} - \varphi_{\mathrm{per}}}{1 - \varphi_{\mathrm{per}}} \right)^{n m_{\mathrm{G}}} \tag{2.13}$$

where C_{Y}, m_{Y} and C_{G}, m_{G} are fitting constants for Young's and shear modulus, respectively; Y_0 and G_0 are the corresponding properties of the bulk material.

For isotropic elasticity, the elastic constants are interrelated by Eq. 2.6, allowing derivation of the scaling equation:

$$\nu_{\mathrm{E}}^{\mathrm{net}} = (\nu_{\mathrm{E}}^{0} + 1) \left(\frac{C_{\mathrm{Y}}}{C_{\mathrm{G}}} \right)^{n} \left(\frac{\varphi_{\mathrm{net}}^{1/n} - \varphi_{\mathrm{per}}}{1 - \varphi_{\mathrm{per}}} \right)^{n(m_{\mathrm{Y}} - m_{\mathrm{G}})} - 1 \tag{2.14}$$

Scaling law for Young's modulus

For unimodal nanoporous structures formed by dealloying, the stability of ligaments is governed by curvature-driven surface diffusion. In particular, slender ligaments with high aspect ratios are susceptible to Plateau–Rayleigh-type instabilities, which promote morphological smoothing and limit the persistence of highly elongated features, especially at low solid fractions φ_{net} [146, 147]. The critical percolation threshold is $\varphi_{\mathrm{per}} = 0.159$ [37]. Soyarslan *et al.* [37] applied the Roberts-Garboczi scaling law to dealloyed nanoporous gold (NPG), obtaining $C_{\mathrm{Y}} \approx 2.0$ and $m_{\mathrm{Y}} \approx 2.5$. These parameters are also supported by experimental data on single-level NPG ($n = 1$) and remain valid for hierarchical NPG ($n = 2$) [22].

The corresponding scaling law for hierarchical NPG with equal φ at each level becomes:

$$Y_{\mathsf{net}} = Y_0\, 2^{n} \left(\frac{\varphi_{\mathsf{net}}^{1/n} - \varphi_{\mathsf{per}}}{1 - \varphi_{\mathsf{per}}} \right)^{5n/2} \tag{2.15}$$

where $Y_0 = 79$ GPa for Au [148].

Scaling law for Shear modulus

Direct measurements of the shear modulus G in NPG are scarce and hard to achieve. Based on reported values of Y and ν_{E} from literature [16, 20, 27, 28, 149, 150], G can be estimated via the classical elasticity relation Eq. 2.4. Assuming a shear modulus of $G_0 = 27$ GPa for fully dense Au [148], fitting the estimated G data to the proposed scaling law yields $C_{\mathrm{G}} \approx 2.0$ and $m_{\mathrm{G}} \approx 2.4$ as shown in Figure 2.4, leading to the following expression for hierarchical nanoporous structures:

$$G_{\mathrm{net}} = G_0 2^{n} \left(\frac{\varphi_{\mathrm{net}}^{1/n} - \varphi_{\mathrm{per}}}{1 - \varphi_{\mathrm{per}}} \right)^{2.4n} \tag{2.16}$$

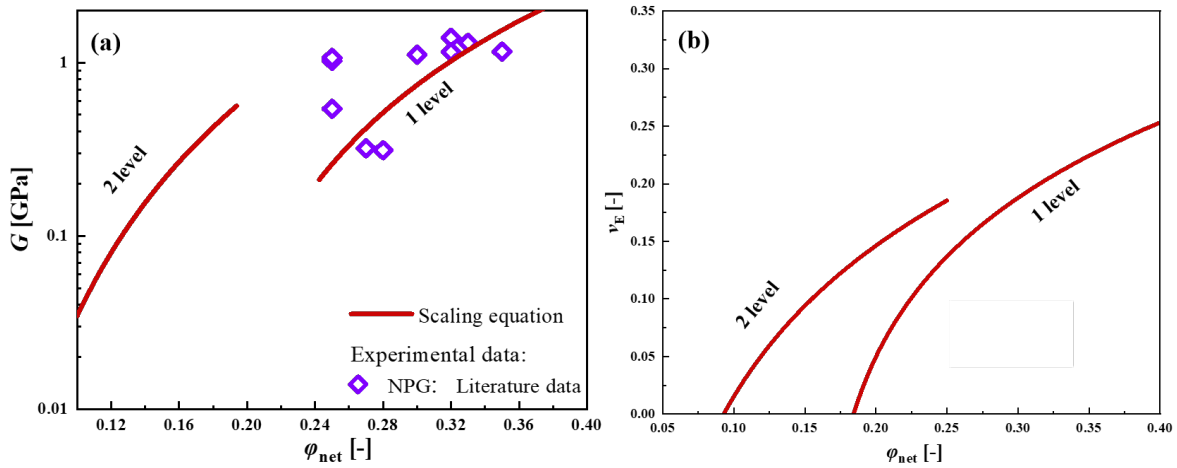


Figure 2.4: Scaling behaviors of shear modulus (G) and elastic Poisson's ratio (ν_{E}) with solid fraction (φ_{net}) of nanoporous gold with different numbers (n) of hierarchical levels. (a) G versus φ_{net} for n=1-2; (b) ν_{E} versus φ_{net} for n=1-2. Open purple rhombuses: G is estimated from experimental Y and ν_{E} of NPG in literature; Red solid lines in (a): Eq. 2.16; Red solid lines in (b): Eq. 2.17.

Figure 2.4 illustrates the scaling behavior of G and ν_{E} for nanoporous gold with different hierarchical levels (n = 1 and n = 2). Open purple rhombuses represent G values estimated from Y and ν_{E} of literature data on NPG using Eq. 2.6. The solid curves show predictions from the scaling law Eq. 2.16 for both n = 1 and n = 2.

Scaling law for Elastic Poisson's ratio

The same scaling constants C_{G} = 2.0 and m_{G} = 2.4 can be substituted into the hierarchical scaling law for elastic Poisson's ratio (ν_{E}). Substituting Eq. 2.15 and 2.16 into Eq. 2.6 yields:

$$\nu_{\mathrm{E}}^{\mathrm{net}} = (\nu_{\mathrm{E}}^{0} + 1)\left(\frac{\varphi_{\mathrm{net}}^{1/n} - \varphi_{\mathrm{per}}}{1 - \varphi_{\mathrm{per}}}\right)^{0.1n} - 1 \tag{2.17}$$

where ν_{E}^{0} is the elastic Poisson's ratio of bulk gold. The weak exponent 0.1 reflects the near cancellation between the scaling of Y and G, rather than a distinct physical mechanism. Figure 2.4b shows the predicted ν_{E} trends based on Eq. 2.17 for n = 1 and n = 2, using $(C_{\mathrm{Y}}, m_{\mathrm{Y}})$ = (2.0, 2.5) from Soyarslan et al. [37]. This model successfully captures the reduction of elastic Poisson's ratio in low-density nanoporous and hierarchical networks.

2.4 Open-System Elasticity (Larché-Cahn Theory)

2.4.1 Thermomechanical Framework and Key Definitions

Classical elasticity assumes a fixed chemical composition during mechanical loading. However, when a solid is in a chemical contact with an external reservoir, its elastic response can also deviate fundamentally from closed-system behavior. Open-system elasticity, formulated by Larché and Cahn, extends Hooke's law by explicitly accounting for coupling between mechanical stress, strain and chemical potential [39, 151, 152].

In a such system, an applied stress can drive redistribution of the mobile solute (e.g., hydrogen), which in turn modifies the strain response of the solid.

Pd-H is a prototypical system for studying this chemo-mechanical coupling because of its high hydrogen solubility and fast hydrogen diffusion at ambient temperature. Hydrogen absorption in Pd induces a volumetric lattice expansion [30, 31]. When the material is in contact with a hydrogen reservoir and the chemical potential μ is fixed, the system behaves as an open thermodynamic system. Under these conditions, mechanical loading can induce redistribution of hydrogen within the solid. This stress-driven solute redistribution leads to a reduction of the apparent elastic stiffness. Shi *et al.* experimentally demonstrated this open-system elastic response in np Pd-based materials [25]. It has been showed that the Young's modulus of np Pd and np PdAu decreases systematically with increasing hydrogen concentration x_{H}, in agreement with the predictions of Larché–Cahn theory. These results establish hydrogen-sorption np Pd as ideal platforms for investigating open-system elasticity and motivate extending this framework beyond Young's modulus to other elastic parameters, including the elastic Poisson's ratio.

Poisson's ratio in a closed system is often treated as a composition-independent constant set by the underlying bonding and microstructure. However, under open-system conditions, the Poisson's ratio becomes composition-dependent as the hydrogen redistribution. Under near-equilibrium conditions controlled by electrochemical processes, this behavior has not yet been directly quantified experimentally. To provide a thermodynamic basis for this behavior, we briefly introduce the coupling between stress, strain and chemical potential in the Larché–Cahn framework.

2.4.2 Maxwell Relations and the Origin of Chemo-Mechanical Coupling

The central coupling in the Larché-Cahn framework originates from a Maxwell relation that links the stress dependence of chemical potential to the concentration dependence of stress. Starting from the Helmholtz free energy density $f(\varepsilon_{ij}, x)$. Then the conjugate variables follow as:

$$\sigma_{ij} = \left(\frac{\partial f}{\partial \varepsilon_{ij}}\right)_x, \qquad \mu = \left(\frac{\partial f}{\partial x}\right)_\varepsilon \tag{2.18}$$

Mixed partial derivatives of f yield the Maxwell relation:

$$\left(\frac{\partial \sigma_{ij}}{\partial x}\right)_\varepsilon = \left(\frac{\partial \mu}{\partial \varepsilon_{ij}}\right)_x \tag{2.19}$$

This identity reveals that the chemical expansion coefficient:

$$\eta_{ij} = \left(\frac{\partial \varepsilon_{ij}}{\partial x}\right)_\sigma \tag{2.20}$$

Thus, stress gradients generate chemical potential gradients, driving solute redistribution, while concentration gradients feed back into the strain field.

2.4.3 Closed-System Elasticity vs. Open-System Elasticity

In the closed system, where solute concentration x is fixed, Hooke's law applies [153, 154]:

$$\varepsilon_{ij} = S_{ijkl}\sigma_{kl} \tag{2.21}$$

where S_{ijkl} is the conventional compliance tensor. In an open-system, however, the local solute concentration is not fixed, but varies with stress at constant μ. The total strain, denoted $\tilde{\varepsilon}_{ij}$, thus includes an additional contribution from stress-induced solute redistribution:

$$\tilde{\varepsilon}_{ij} = \tilde{S}_{ijkl}\sigma_{kl} \tag{2.22}$$

where $\tilde{S}_{ijkl}$ is the open-system compliance tensor. The difference $\Delta S_{ijkl} = \tilde{S}_{ijkl} - S_{ijkl}$ quantifies the softening introduced by mobile solute redistribution under deformation or stress.

For clarity, we consider the uniaxial, scalar reduction of the general tensorial framework. Under isothermal and uniaxial loading conditions, Larché and Cahn derived the differential form of the free energy per unit volume $f(\varepsilon_{ij}, x)$ as [39]:

$$df = \sigma d\varepsilon + \rho_0 \mu dx \tag{2.23}$$

where ρ_0 is the site density. Applying a Legendre transformation with respect to strain yields:

$$d(f - \sigma\varepsilon) = -\varepsilon d\sigma + \rho_0 \mu dx \tag{2.24}$$

Differentiating twice gives a Maxwell relation:

$$\left(\frac{\partial \mu}{\partial \sigma}\right)_x = -\frac{1}{\rho_0}\left(\frac{\partial \varepsilon}{\partial x}\right)_\sigma \tag{2.25}$$

where ρ_0 the density of available interstitial sites. This Maxwell relation shows that mechanical loading can modify the chemical potential, thereby inducing changes in solute concentration under open-system conditions. To quantify the sensitivity of concentration to changes in chemical potential, it is convenient to introduce the solute susceptibility, defined as:

$$\chi = \frac{1}{\rho_0}\left(\frac{\partial x}{\partial \mu}\right)_T \tag{2.26}$$

This quantity characterizes how strongly the solute concentration responds to variations in chemical potential and plays a central role in determining the magnitude of open-system elastic effects.

2.4.4 Isotropic Approximation

For isotropic solids, the open-system Young's modulus Y^μ is related to its closed-system counterpart Y^x through [25]:

$$Y^\mu = \frac{Y^x}{1 + \chi\eta^2 Y^x} \tag{2.27}$$

The compliance difference is given by:

$$\Delta s = s^\mu - s^x = \chi\eta^2 \tag{2.28}$$

For an isotropic solid under open-system conditions, Larché and Cahn showed that solute exchange does not affect the shear response, so that the open-system shear modulus is strictly equal to its closed-system value, $G^{\mu} = G^{x}$ [39].

The open-system Poisson's ratio ν^{μ} is given by the general Larché-Cahn expression (Eq. 61 in REF. [39]):

$$\nu^{\mu} = \frac{\nu^{x} - \chi\eta^{2}Y^{x}}{1 + \chi\eta^{2}Y^{x}} \tag{2.29}$$

where Y^{x} and ν^{x} are the Young's modulus and Poisson's ratio measured at fixed hydrogen content, χ is the solute susceptibility, and η is the compositional strain coefficient.

Using the isotropic elastic identity $\nu = Y/(2G) - 1$ together with $G^{\mu} = G^{x}$, Eq. (2.29) can be rewritten in an equivalent form:

$$\nu^{\mu}(x) = (\nu^{x} + 1)\,\frac{Y^{\mu}(x)}{Y^{x}} - 1 \tag{2.30}$$

2.4.5 Implications for np Pd–H Systems

Pd-based alloys provide a convenient model system for investigating open-system elasticity, owing to their fast hydrogen diffusivity. In such systems, the solute susceptibility χ becomes particularly near the miscibility gap, enhancing stress–solute coupling. The concentration–strain coefficient η, which governs the lattice response to hydrogen insertion, is determined from lattice expansion data and typically takes the value $\eta \approx 0.063 \pm 0.003$ [25].

Although the values of χ and η are system-dependent, representative estimates can be obtained from previous studies [25, 155]. For hydrogen in Pd-based systems:

- The concentration–strain coefficient is $\eta \approx 0.063 \pm 0.003$;
- The volumetric site density is $\rho_0 \approx 1.2 \times 10^{22}\,\mathrm{atoms/cm^3}$ for the fcc lattice.

To rationalize the evolution of $\nu^{\mu}_{\mathrm{E}}(x)$, it is instructive to consider a regular interstitial solution with a miscibility gap, for which the chemical potential may be written in reduced form as [156]

$$\mu = RT_{\mathrm{C}}\left(2 - 4x + \tau \ln\frac{x}{1-x}\right) \tag{2.31}$$

where R is the gas constant, T_{C} is the critical temperature and $\tau = T/T_{\mathrm{C}}$ is the reduced temperature. Although this regular-solution description is not intended as a quantitative phase-diagram model for the nanoporous networks studied here, it captures the key qualitative point required for open-system elasticity: the curvature of $\mu(x)$ controls the susceptibility $\chi(x)$ and χ reflects the magnitude of the additional compliance term and thus the tunability of Y^{μ} and ν^{μ}.

Figure 2.5 summarizes this connection for parameters representative of Pd-H. Figure 2.5a shows μ/RT_{C} as a function of x for different reduced temperatures. For $T < T_{\mathrm{C}}$, the miscibility gap limits the single-phase region accessible under equilibrium conditions, whereas for $T \geq T_{\mathrm{C}}$, μ increases with x. Figure 2.5b shows the corresponding susceptibility $\chi(x)$, which becomes large where the μ-x curve is locally flat and evolves

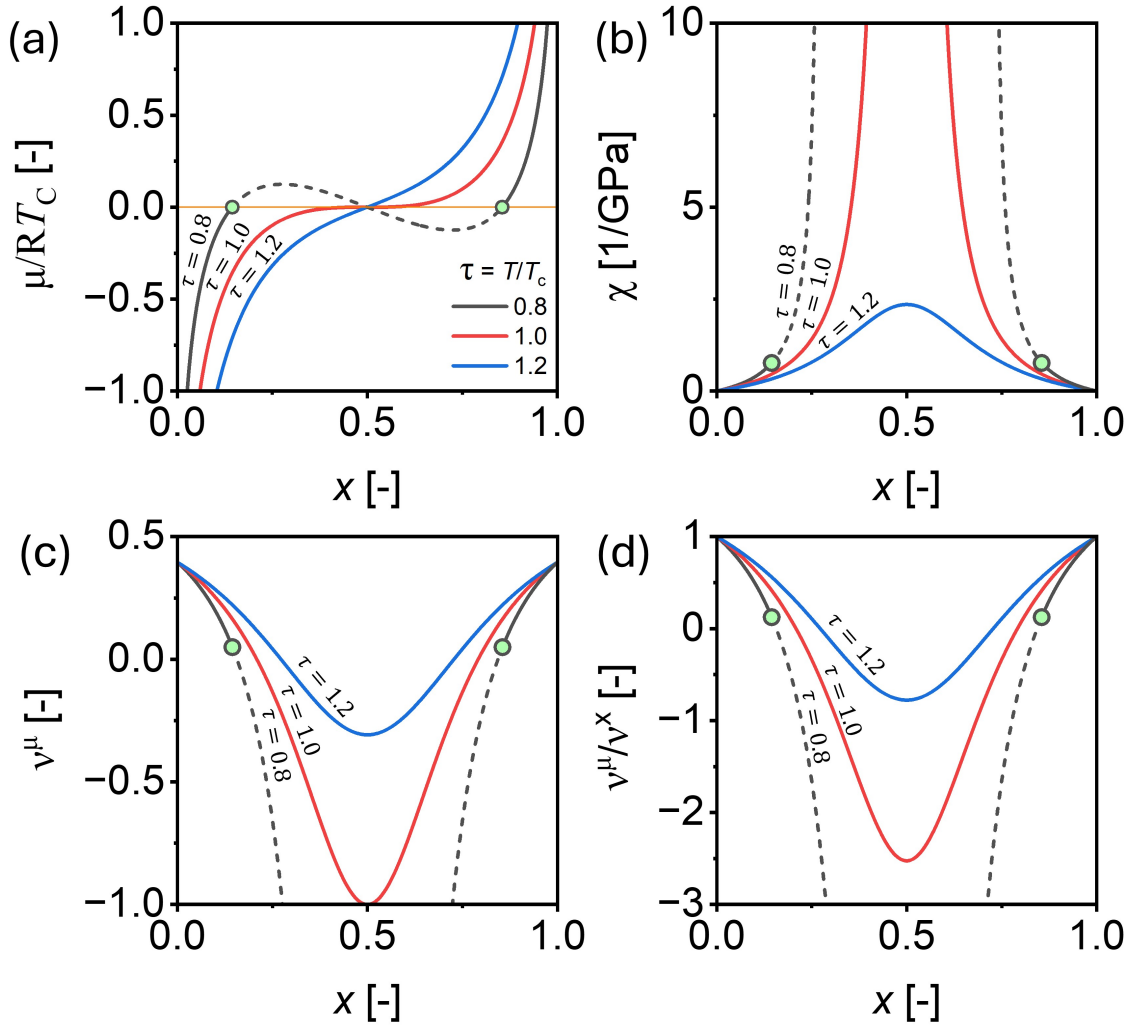


Figure 2.5: Chemical potential, susceptibility and open-system Poisson's ratio for a regular interstitial solution using parameters representative of Pd. (a) Normalized chemical potential μ/RT_C, (Eq. 2.31) at different temperatures. The legend indicates the reduced temperature, $\tau = T/T_C$, where T_C is the critical temperature. The dash line shows the miscibility gap for $T < T_C$; (b) Susceptibility, χ, of the Pd–H system modeled as a regular interstitial solution using Pd–H parameters; (c) Open-system Poisson's ratio, ν^μ (Eq. 2.29) and (d) relative Poisson's ratio, ν^μ/ν^x as functions of x. At the critical temperature ($\tau = 1$), ν^μ exhibits the steepest variation with x; consequently, ν^μ changes from its initial value to -1 at the critical point.

most steeply around the critical composition. In turn, Eq. (2.30) predicts that ν^μ can undergo a pronounced, continuous decrease with increasing x and approach the theoretical lower bound of -1 in the vicinity of the critical point (Figure 2.5c). The normalized ratio ν^μ/ν^x (Figure 2.5d) emphasizes that this modulation can be very large even when ν^x itself remains positive.

Chapter Summary

This chapter has outlined the theoretical background relevant to the synthesis, microstructure and elastic behavior of dealloyed nanoporous metals. Starting from the thermodynamic and kinetic principles of electrochemical dealloying, the formation of bicontinuous porous networks was discussed, including key concepts such as the parting limit, the critical dealloying potential and curvature-driven coarsening governed by surface diffusion. These aspects provide a basis for understanding how processing parameters influence the resulting microstructure.

Subsequently, scaling relations for porous network materials were introduced to describe how macroscopic mechanical properties, including Young's modulus and Poisson's ratio, depend on structural parameters such as solid volume fraction and network structure. Extensions to hierarchical structures were also presented, providing a framework for interpreting multiscale nanoporous systems.

In addition, the concept of open-system elasticity, as developed by Larché and Cahn, was briefly reviewed. This framework describes the coupling between mechanical deformation and solute redistribution under conditions of controlled chemical potential, and offers a basis for analyzing composition-dependent elastic response in systems with mobile solute species.

Overall, the theoretical considerations summarized in this chapter provide a conceptual and quantitative basis for the analysis of the experimental results presented in the following chapters.

Chapter 3

Materials Preparation and Methods

This chapter details the experimental methods used to synthesize, characterize and mechanically test nanoporous metallic materials, with a focus on HNPG and dealloyed np Pd and np PdAu. These systems serve as representative model platforms to investigate how microstructure and hydrogen concentration influence mechanical response.

Section 3.1 describes the alloying processes and thermomechanical treatments used to prepare master alloys with well-controlled composition and microstructure. Section 3.2 introduces the electrochemical dealloying procedures used to generate nanoporous networks with different characteristic ligament sizes, with special attention given to hierarchical structure formation in HNPG and electrochemical hydrogen sorption in Pd-based alloys. Section 3.3 outlines the imaging and analytical techniques employed across multiple length scales, including electron microscopy and diffraction-based methods, to assess porosity, ligament size, composition and phase. Finally, Section 3.3.3 presents the mechanical testing protocols and digital image correlation (DIC) analysis used to extract mechanical parameters such as Young's modulus, yield strength and Poisson's ratio under both ambient and electrochemical conditions.

3.1 Material

Three types of precursor master alloys were synthesized for the fabrication of HNPG, np Pd and np PdAu. In all cases, high-purity elemental wires were used as starting materials and alloyed by arc melting, followed by homogenization, quenching, mechanical processing, sectioning and ultrasonic cleaning. Specific procedures for each system are summarized below.

All alloys were prepared by repeated melting-solidification at least 25 times of high-purity metal wires (Au: 99.95%, Alfa Aesar, Ag: 99.99%, Heraeus Metals, Pd: 99.95%, Heraeus Metals and Cu: 99.99%, Alfa Aesar) in an arc-melter (MAM-1, Edmund Bühler) under Ar atmosphere to ensure compositional uniformity. All the metal wires were cleaned in an ultrasonic bath before melting. First, the wires were immersed in acetone at 60 °C for at least 15 minutes and then in ethanol at room temperature for 5 minutes. This process removes stains from the surface of the metal wire and any oil residue left behind during the pulling process which is crucial for maintaining the purity of alloy ingots after melting. In addition, before using the arc-melter, thoroughly clean its chamber by using the accompanied substrate cleaner No. 1 (Umicore, Code: 0481900)

and No. 2 (Umicore, Propan-2-ol) to remove any residual stains and finally wipe dry with anhydrous ethanol. The sequence of using cleaning agents is critical. Improper cleaning may result in incomplete chamber cleaning or failure to fully remove the aluminum oxide abrasive from the substrate cleaner No. 1. This will ultimately result in the alloy ingots failing to meet purity standards which would compromise subsequent experiments. Besides, a pure titanium ball (99.95%, Alfa Aesar) is necessarily placed inside the chamber and melted several times before alloy melting begins in order to completely consume any residual oxygen in the chamber and protect the alloy from oxidation.

The resulting alloy ingots were then sealed in evacuated quartz tubes for homogenization annealing. $Ag_{93}Au_7$ (at.%), $Pd_{15}Cu_{85}$ (at.%) and $Pd_{12.5}Au_{2.5}Cu_{85}$ (at.%) were homogenized at 850 °C, 1000 °C and 1000 °C for at least 7 days, respectively. All the ingots were then cold-rolled into thin plates using a manual rolling mill with small strain increments to avoid cracking, with a final thickness of 1.2 mm. After that, the rolled plates were polished on both sides and plates were mounted on ceramic plates with wax and subsequently cut into cuboids of 1.2 mm × 0.8 mm × 0.8 mm for $Ag_{93}Au_7$, $Pd_{15}Cu_{85}$ and $Pd_{12.5}Au_{2.5}Cu_{85}$, respectively. All cuboids were finally cleaned in an ultrasonic bath, first in acetone at 60 °C for 15 minutes and then in ethanol at 25 °C for 5 minutes, before being subjected to electrochemical dealloying.

3.2 Electrochemical dealloying and in situ electrochemical tests

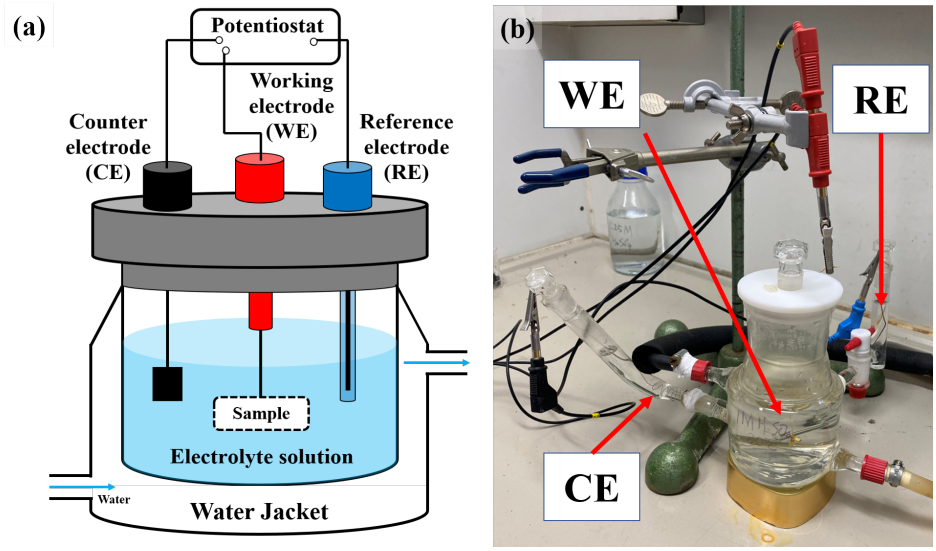


Figure 3.1: Three-electrode electrochemical cell used for dealloying. (a) Schematic illustration of the unified cell configuration, showing the working electrode (WE), counter electrode (CE) and reference electrode (RE) connected to a potentiostat for potential control; (b) Photograph of the actual electrochemical cell equipped with an external water jacket for precise temperature control of the electrolyte.

All nanoporous metals in this study were prepared in an acidic aqueous electrolyte

via an electrochemical dealloying method. As illustrated in Figure 3.1, all electrochemical dealloying experiments were conducted using a thermostated three-electrodes electrochemical cell. Figure 3.1a shows a schematic of the unified cell configuration employed throughout this study, where the working electrode (WE), counter electrode (CE) and reference electrode (RE) are connected to a potentiostat. While the general setup remained consistent, the choice of CE and RE was adjusted depending on the material system and electrolyte composition. A water jacket connected to a thermostat is used to control the temperature of the electrolyte.

To illustrate the working principle of the three electrodes and the cell, Figure 3.1b shows the actual setup used in the experiments. The water jacket allows precise control of electrolyte temperature. When heating was required, the circulating water bath was set to the desired temperature; otherwise, the bath was maintained at 25 °C to minimize environmental temperature fluctuations. This design ensures improved reproducibility and accuracy in the electrochemical measurements.

A potentiostat was used to control the applied potential and to monitor the electrochemical response during dealloying. In most experiments, pseudo-Ag/AgCl reference electrodes [157] were employed due to their stable and reproducible potential in low-chloride acidic electrolytes. For specific systems, such as np Pd and np PdAu, commercial Ag/AgCl electrodes (3 M KCl, Sigma-Aldrich) or a standard hydrogen electrode (SHE, Gaskatel) were used instead. Detailed electrode configurations and dealloying parameters for each material system are provided in the following subsections. Potentials reported throughout this work are always referenced to the electrode specified in each subsection; accordingly, absolute potentials are not compared across different reference systems. Conversion to SHE is given for orientation; temperature-dependent offsets may introduce an uncertainty on the order of several mV.

3.2.1 HNPG

HNPG was synthesized via a three-step "dealloying–coarsening–dealloying" protocol, as illustrated in Figure 3.2a. This synthesis approach follows the methodology established by Shi *et al.* [22], with slight adjustments to the dealloying and coarsening conditions to achieve the desired hierarchical ligament sizes. All electrochemical treatments were carried out in the thermostated three-electrodes cell described in Sec. 3.2, using a potentiostat (PGSTAT 302N, Metrohm) for potential control. Unless otherwise specified, a pseudo-Ag/AgCl reference electrode [157] was used throughout. The choice of counter electrode depended on the synthesis stage: a silver wire was used in Stage I, whereas a carbon cloth (Kynol, specific surface area 1200–1750 m^2/g) was employed in Stage III, where cyclic voltammetry (CV) was applied. The electrolyte was gently stirred and maintained at 25 °C unless otherwise specified.

Step I: Dealloying to form nanoporous $Ag_{75}Au_{25}$: Cuboidal $Ag_{93}Au_7$ (at.%) samples, prepared as described in Sec. 3.1, were immersed in 0.01 M H_2SO_4 (Suprapur, Merck) at a constant potential of 0.359 V vs. pseudo-Ag/AgCl until the target amount of Ag was selectively dissolved, yielding an intermediate composition of $Ag_{75}Au_{25}$.

The amount of Ag removed was calculated using Faraday's law of electrolysis in Eq.2.2 where z is the number of electrons transferred per Ag atom (z=1, $Ag \rightarrow Ag^+ + e^-$). The number of moles of Ag atom to be removed was determined from the change in

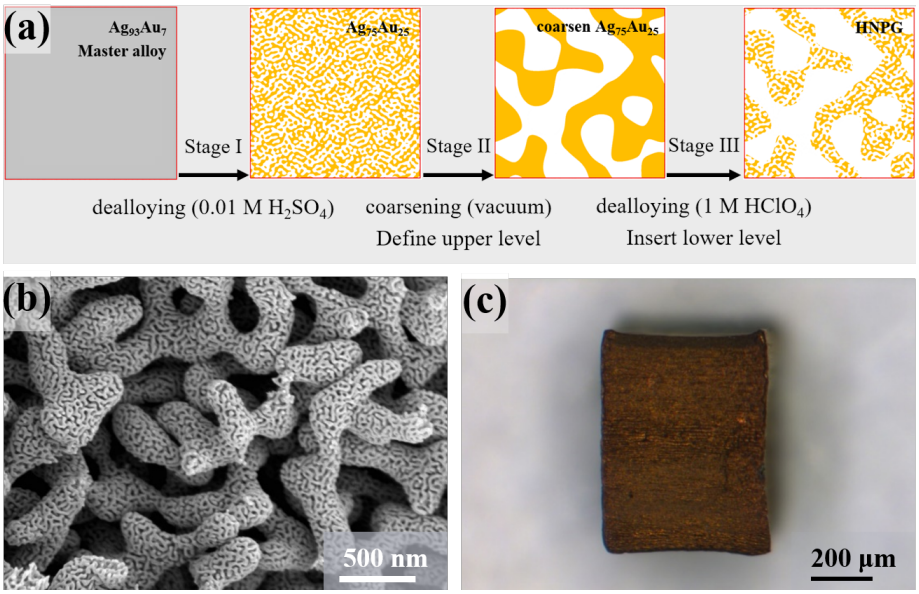


Figure 3.2: Preparation process, appearance and microstructure of HNPG. (a) Scheme describing the synthesis route and structural features of each stage from $Ag_{93}Au_7$ master alloy to nanoporous $Ag_{75}Au_{25}$ (NPSG) alloy and then to HNPG; (b) SEM images showing the fracture surface microstructure of HNPG. The lower level ligaments were embedded in the upper level ligaments to form a hierarchical structure and (c) optical microscope images of HNPG free from cracks and defects. The dimensions and weight are then measured to obtain the solid volume fraction.

atomic fraction [22]:

$$n_{\mathrm{Ag,removed}} = \left(\frac{c_{\mathrm{Ag,initial}} - c_{\mathrm{Ag,final}}}{100} \right) \cdot \frac{m_{\mathrm{sample}}}{M_{\mathrm{alloy}}} \tag{3.1}$$

where $c_{\mathrm{Ag,initial}} = 93\%$ and $c_{\mathrm{Ag,final}} = 75\%$ are the initial and target Ag atomic fractions, m_{sample} is the measured sample mass and M_{alloy} is the molar mass of the $Ag_{93}Au_7$ alloy. The corresponding target charge is:

$$Q_{\mathrm{target}} = n_{\mathrm{Ag,removed}} \cdot F \cdot z. \tag{3.2}$$

The complete electrochemical protocol is illustrated in Figure 3.3. Figure 3.3a shows the applied dealloying potential of 0.359 V vs. pseudo-Ag/AgCl, held constant throughout the process. The corresponding current response (Figure 3.3b) displays a rapid initial decay as Ag is dissolved. The integrated anodic charge (Figure 3.3c) increases monotonically and was used to monitor the degree of dissolution in real time. The dealloying was terminated once the total charge matched the calculated Q_{target}, ensuring precise control over the residual composition and the formation of a bicontinuous nanoporous $Ag_{75}Au_{25}$ network. In actual experiments, the target charge Q_{target} was also adjusted based on empirical values reported in the literature [22] in order to achieve more controlled dealloying.

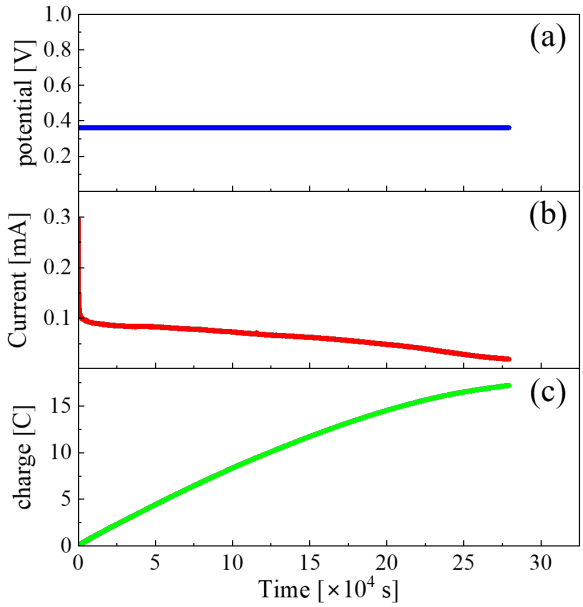


Figure 3.3: Electrochemical protocol for the first-step partial dealloying of $Ag_{93}Au_7$ (at.%) to form nanoporous $Ag_{75}Au_{25}$. (a) Constant applied potential of 0.359 V vs. pseudo-Ag/AgCl in 0.01 M H_2SO_4; (b) transient current response showing the decay as Ag is selectively dissolved and (c) integrated anodic charge versus time. The dealloying process was terminated when the cumulative charge matched the target value Q_{target}, calculated from the desired change in Ag atomic fraction using Faraday's law.

Step II: Thermal coarsening: The as-dealloyed np $Ag_{75}Au_{25}$ samples were cleaned, dried and subsequently annealed under high vacuum ($< 1 \times 10^{-6}$ mbar) at 300 °C, 350 °C, 400 °C and 450 °C for 20 minutes each in an annealing furnace (MILA-5000, ULVAC). This thermal treatment induced ligament coarsening, producing the upper-level nanoporous network with ligaments. Samples after this stage are referred to as nanoporous silver-gold (NPSG).

Step III: Final dealloying to obtain HNPG: The coarsened NPSG samples were subjected to a second electrochemical dealloying step in 1.0 mol/L $HClO_4$ (Suprapur, Merck), employing a two-potential protocol to achieve complete removal of residual Ag and establish the hierarchical network microstructure. As shown in Figure 3.4, the applied potential (Figure 3.4a) was first held at 0.8 V vs. pseudo-Ag/AgCl until the current decayed below 10 μA, followed by a second step at 1.0 V until the current dropped below 2 μA. This second electrochemical dealloying step generates a fine lower-level nanoporous network with ligaments within the previously coarsened ligaments.

The current response over time (Figure 3.4b) displays characteristic transients associated with Ag removal, while the integrated anodic charge (Figure 3.4c) serves as a cumulative measure of the electrochemical reaction progress. Following potentiostatic dealloying, cyclic voltammetry (CV) was performed between 0.34 and 0.99 V (vs. pseudo-Ag/AgCl) for 5 cycles at a scan rate of 10 mV/s, as shown in Figure 3.4d. This final CV step will further remove residual Ag through repeated oxidation–reduction cycles. The resulting HNPG samples thus exhibit dual-length-scale porosity and low Ag content, suitable for subsequent mechanical and electrochemical characterization.

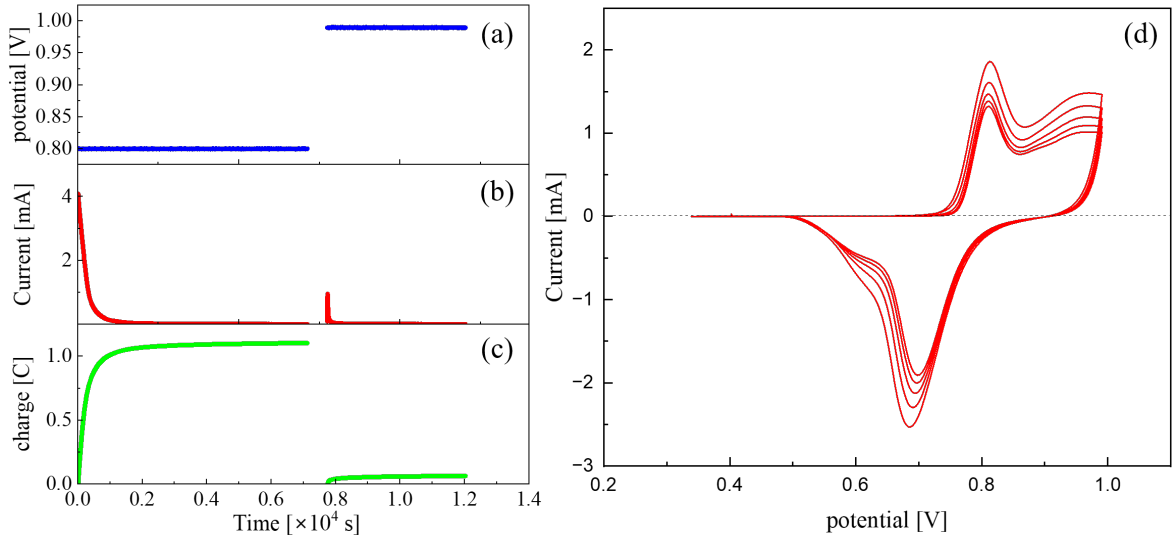


Figure 3.4: Representative electrochemical protocol for the final dealloying step to obtain HNPG from coarsened NPSG precursors. (a) Time sequence of applied potentials in 1.0 M $HClO_4$: an initial step at 0.8 V followed by a higher-potential step at 1.0 V (both vs. pseudo-Ag/AgCl), designed to enable gradual Ag removal while avoiding crack formation; (b) Corresponding current response showing rapid decay during each step, consistent with progressive surface passivation and compositional evolution; (c) Integrated anodic charge versus time, used to monitor total Ag dissolution and (d) Subsequent cyclic voltammetry (CV) between 0.34 and 0.99 V (5 cycles at 10 mV/s).

Adjustment of lower-level ligament size: In addition to the standard Stage III protocol described above, HNPG samples with systematically varied lower-level ligament sizes (L_1) were prepared by modifying the final dealloying conditions.

For samples with finer lower-level ligament sizes ($L_1 < 20$ nm), a two-step potentiostatic treatment was applied in 1.0 mol/L $HClO_4$: first at $E_1 = 1.4$ V vs. pseudo-Ag/AgCl for 3600 s, followed by $E_2 = 1.0$ V vs. pseudo-Ag/AgCl for 1800 s. This higher-potential dealloying protocol promotes aggressive Ag removal and finer pore formation, albeit at the cost of increased surface roughness and potential instability.

The standard condition ($L_1 = 20$ nm) corresponded to the two-potential plus CV protocol described in Stage III and illustrated in Figure 3.4, which combines moderate dealloying bias with post-treatment cyclic voltammetry to balance fine pore and structural stability. For coarser lower-level structures ($L_1 \approx 40$ nm), additional electrochemical coarsening was introduced by applying 60 CV cycles (0.34–0.99 V vs. pseudo-Ag/AgCl at 10 mV/s) to pre-formed $L_1 = 20$ nm samples. This extended cycling enhances coarsening of lower level ligaments without disrupting the overall hierarchical morphology.

All samples were thoroughly rinsed in deionized water (Ultra Clear TWF UV, Siemens) for at least 12 h to remove residual acid, followed by ethanol exchange (≥99.5%) for at least 6 h to facilitate drying. To minimize capillary-induced cracking during drying, excess ethanol was gently removed and the samples were left to dry under gentle environmental conditions (25 °C).

3.2.2 np Pd and np PdAu

np Pd and np PdAu samples were fabricated by electrochemical dealloying of $Pd_{15}Cu_{85}$ and $Pd_{12.5}Au_{2.5}Cu_{85}$, respectively. These alloy precursors were prepared as described in Sec. 3.1. The dealloying experiments were conducted using the same thermostated three-electrodes cell (Sec. 3.2). A commercial Ag/AgCl reference electrode (3 M KCl, Sigma-Aldrich) was used. Copper wire served as the counter electrode during dealloying, whereas carbon cloth was employed during the cyclic voltammetry (CV) cleaning steps.

Synthesis of np Pd:

Dealloying of $Pd_{15}Cu_{85}$ precursor alloys was conducted in 1.0 mol/L H_2SO_4 (Suprapur, Merck) at 60 °C. A constant potential of 0.79 V vs. SHE (0.576 V vs. commercial Ag/AgCl) was applied until the current dropped below 5 μA, indicating no further substantial Cu dissolution. To eliminate residual copper species as much as possible, a post-treatment step comprising cyclic voltammetry (CV) between 0 and 1.2 V vs. SHE (-0.2 and 1.0 V vs. commercial Ag/AgCl) was carried out for 10 cycles at a scan rate of 10 mV/s.

The electrochemical protocol is illustrated in Figure 3.5. Figure 3.5a shows the dealloying potential held constant during the dealloying, while Figure 3.5b records the corresponding current transient. The initially high dissolution current decays rapidly. The integrated charge over time in Figure 3.5c enables an upper-bound estimate of the amount of copper removed based on Faraday's law, as minor contributions from parasitic currents cannot be fully excluded.

After dealloying, the electrochemical characteristics of the resulting np Pd were assessed using cyclic voltammetry. As shown in Figure 3.6, the cyclic voltammetry exhibits distinct redox features such as hydrogen absorption/adsorption/desorption (region below 0.3 V vs. commercial Ag/AgCl) and Pd surface oxidation/reduction at more positive potentials.

Synthesis of np PdAu:

Dealloying of $Pd_{12.5}Au_{2.5}Cu_{85}$ precursor alloys was carried out in 1.0 mol/L H_2SO_4 (Suprapur, Merck) at an elevated temperature of 80 °C, chosen to accelerate Cu dissolution kinetics and promote uniform ligament morphology across the sample. This is consistent with previous findings that higher dealloying temperatures can improve bicontinuity and reduce topological defects in the final nanoporous structure.

A two-step potentiostatic protocol was employed: the first step held the potential at 0.74 V vs. SHE (0.526 V vs. commercial Ag/AgCl) until the current decayed to below 10 μA, after which a second step at 0.79 V vs. SHE (0.576 V vs. commercial Ag/AgCl) was applied until the current fell below 5 μA. The entire procedure is illustrated in Figure 3.7. Figure 3.7a shows the applied potential sequence, Figure 3.7b the corresponding current transient and Figure 3.7c the cumulative anodic charge, which provides a quantitative estimate of Cu removal based on Faraday's law.

The two-step potentiostatic protocol was employed to moderate Cu dissolution during the initial stages of dealloying and thereby reduce the risk of crack formation. Direct application of the higher potential could accelerate Cu dissolution, potentially generating steep chemical-potential gradients and associated internal stresses. Such stresses may promote cracking in the developing nanoporous network, particularly in bulk specimens. Following dealloying, the np PdAu samples underwent an electrochemical cleaning and stabilization treatment similar to that used for np Pd. The treatment

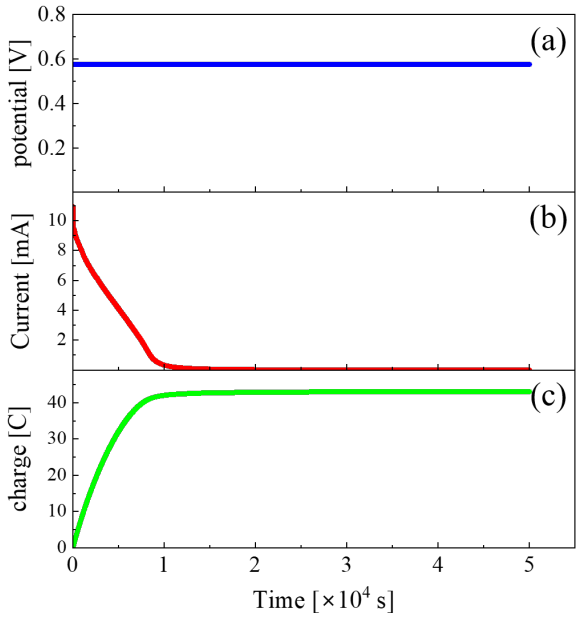


Figure 3.5: Representative electrochemical protocol for dealloying $Pd_{15}Cu_{85}$ in 1.0 mol/L H_2SO_4 at 60 °C. (a) Applied dealloying potential = 0.576 V vs. commercial Ag/AgCl; (b) resulting current response and (c) integrated charge over time.

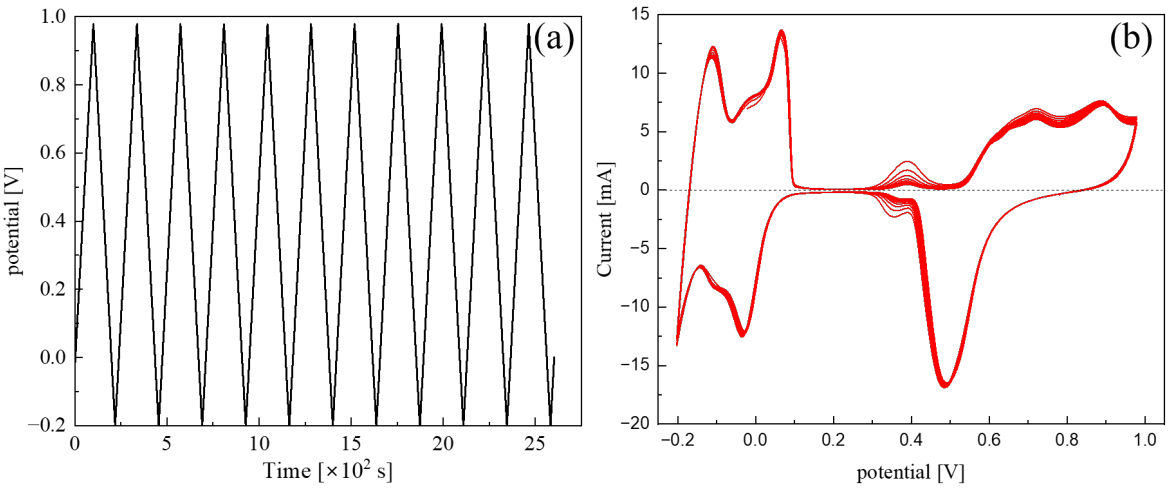


Figure 3.6: Representative cyclic voltammetry (CV) data of nanoporous Pd in 1.0 mol/L H_2SO_4 at room temperature, recorded at a scan rate of 10 mV/s. (a) Time evolution of the applied potential vs. commercial Ag/AgCl during potential cycling; (b) Current–potential response of the np Pd, showing characteristic redox peaks associated with hydrogen adsorption/desorption and surface oxidation/reduction processes. The shape and stability of the cyclic voltammetry reflect the electrochemical activity and surface state of the dealloyed np Pd.

consisted of 20 cycles of cyclic voltammetry (CV) between 0 and 1.0 V vs. SHE at a scan rate of 10 mV/s in fresh 1.0 mol/L H_2SO_4. The resulting voltammetric response exhibited features comparable to those observed for np Pd (Figure 3.6), including hydrogen adsorption, absorption and desorption at lower potentials, as well as Pd surface oxidation and reduction at higher potentials. These similarities indicate comparable

overall electrochemical characteristics after dealloying, despite the differences in their cleaning protocols. After completing the electrochemical treatments, both np Pd and np PdAu samples were thoroughly rinsed in deionized water for at least 12 h, immersed in pure ethanol for at least 6 h, and subsequently dried at 25 °C.

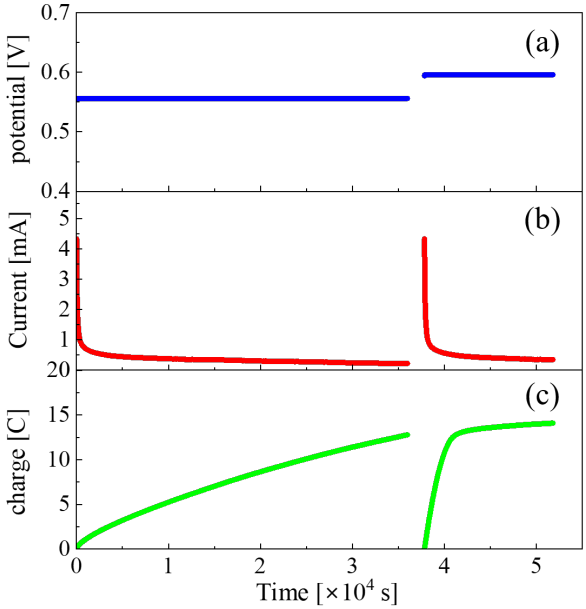


Figure 3.7: Representative electrochemical protocol for dealloying $Pd_{12.5}Au_{2.5}Cu_{85}$ in 1.0 mol/L H_2SO_4 at 80 °C using a two-step potentiostatic procedure. (a) Applied potential profile: the first step at 0.74 V vs. SHE (0.526 V vs. commercial Ag/AgCl) and the second at 0.79 V vs. SHE (0.576 V vs. commercial Ag/AgCl); (b) Corresponding current transient shows rapid decay in both steps as Cu dissolution proceeds and (c) Integrated charge vs. time reveals the cumulative electrochemical charge passed, enabling estimation of Cu removal via Faraday's law.

3.3 Sample characterization

3.3.1 Imaging, elemental composition and structural analysis

High-resolution scanning electron microscopy equipped with an immersion lens (SEM, FEI Helios NanoLab G3), was used to characterize the microstructures of NPSG, HNPG, np Pd and np PdAu. SEM imaging was typically performed at an accelerating voltage of 2 kV with a working distance of about 4 mm. To evaluate the internal microstructure and verify the uniformity of the morphology, SEM images were acquired from freshly exposed fracture surfaces. Cross-sectional specimens were prepared by two different approaches: for as-prepared samples, the center region was precisely cut using a scalpel, whereas plastically deformed samples were sectioned using focused ion beam (FIB) milling with a gallium ion source to preserve microstructural integrity. In the case of plastically deformed specimens, micropillars with a diameter of approximately 8 μm and an aspect ratio of ~2.5 were fabricated for detailed microstructural analysis. To minimize ion-beam-induced damage, the FIB milling was performed stepwise by

gradually decreasing the ion current from 5.0 nA to 0.5 nA at an accelerating voltage of 30 kV. Ligament size, defined as the minimum neck diameter between adjacent pores, was quantified by measuring at least 50 ligaments per representative SEM image using ImageJ software (version 1.53k) [158].

Elemental compositions were analyzed using energy-dispersive X-ray spectroscopy (EDX) integrated into the SEM. Measurements were conducted on fracture surfaces at an accelerating voltage of 15 kV and a working distance of approximately 4 mm to ensure a sufficient excitation volume for accurate quantification. Phase analysis of np Pd and np PdAu samples was performed using X-ray diffraction (XRD, Bruker D8 Advance) equipped with a Cu Kα radiation source.

Transmission electron microscopy (TEM) was carried out using a FEI Talos F200X microscope operated at 200 kV to examine the ultra fine ligament structure. TEM characterization was particularly essential for np PdAu samples, where the ligament sizes were often below the resolution limit of SEM. TEM specimens were prepared by ultrasonic dispersion of small fragments, followed by deposition of the suspension onto molybdenum grids via drop-casting.

3.3.2 Solid Volume Fraction Measurement

The solid volume fraction φ was determined by combining gravimetric and geometric measurements. The mass m of each sample was measured using a microbalance and the macroscopic volume V_{geo} was obtained from calibrated optical microscopy images. The apparent density of the sample is then given by:

$$\rho_{\text{app}} = \frac{m}{V_{\text{geo}}} \tag{3.3}$$

where m is the sample's mass. V_{geo} is sample's geometrically measured volume, which was measured under optical microscope.

Then the solid volume fraction is calculated as:

$$\varphi = \frac{\rho_{\text{app}}}{\rho_0} \tag{3.4}$$

where ρ_0 is the theoretical density of the fully dense material, determined from the nominal composition using the rule of mixtures.

For HNPG, φ at different hierarchical levels were extracted from measurements performed after each dealloying stage, following the approach described in Ref. [159]. The calculated values and their detailed analysis are presented in Sec. 4.1.1.

3.3.3 Mechanical Characterization and Digital Image Correlation

Mechanical characterization: Nanoporous metals are known to deform plastically in compression but fail in a brittle manner under tension [160]. Therefore, all mechanical characterization in this work was conducted under uniaxial compression. The focus was placed on analyzing both elastic and plastic deformation regimes, as well as the directional coupling of axial and transverse strains.

Cuboidal specimens with flat surfaces and uniform dimensions were used to minimize edge effects and ensure proper alignment. All tests were performed at a constant engineering strain rate of $10^{-4}\,\mathrm{s}^{-1}$, with an initial preload of 0.5 N to establish contact between specimen and loading platens. Force and displacement were recorded continuously and converted into engineering stress–strain curves based on the initial geometry. Both continuous loading to large strains (over ~60%) and cyclic load–unload protocols were employed. The latter enabled a more accurate determination of elastic properties: since nanoporous metals typically yield immediately upon loading, Young's modulus was extracted from the load–unload protocols [22]. In the loading–unloading tests, deformation was applied in incremental steps, each followed by partial unloading that allows the evaluation of elastic softening or stiffening during progressive plastic deformation [22]. All experimental protocols were executed using the testXpert II control software (Zwick), either as continuous compression or sequential loading–unloading programs. The acquired data were used to analyze the effective Young's modulus, yield behavior and strain hardening. Plastic Poisson's ratios were extracted from full-field strain data obtained during continuous loading, as described in the following subsection.

For HNPG, uniaxial compression tests were performed on a Zwick 1474 universal testing machine integrated with a high-resolution camera system (LaVision Phantom Miro M-series). The images acquired during loading were analyzed by digital image correlation (DaVis 8.3.0, LaVision GmbH). The test was conducted in a laboratory with 25 °C ambient air. For np Pd and np PdAu, mechanical testing was performed on a Zwick 5kN Allround table top system combined with a high-resolution camera (Baumer VCXU.2-127M) and controlled illumination. DIC analysis was carried out with DaVis 8.3.0 same as HNPG. In selected experiments, hydrogen content x_{H} in the samples was varied by employing a three-electrodes electrochemical cell (1 mol/L H_2SO_4) under open-circuit or potential-controlled conditions. A standard hydrogen electrode (SHE, Gaskatel) served as the reference and carbon cloth was used as counter electrode.

Figure 3.8 illustrates the experimental setup used for mechanical testing of both HNPG and np Pd/np PdAu samples. Figure 3.8a shows the setup for testing of HNPG under ambient conditions, where the sample is placed between conical push rods and observed using a high-speed camera system with ring illumination for DIC analysis. Figure 3.8b presents the in situ electrochemical configuration used for np Pd and np PdAu samples. This setup retains the same optical and mechanical arrangement as in Figure 3.8a, with the addition of a transparent electrochemical cell that enables hydrogen charging under controlled conditions during compression (see Sec. 3.2.2 for details). Figure 3.8c provides a schematic illustration of the measurement configuration, highlighting the sample placement between push rods and the speckled surface pattern used to facilitate accurate DIC tracking.

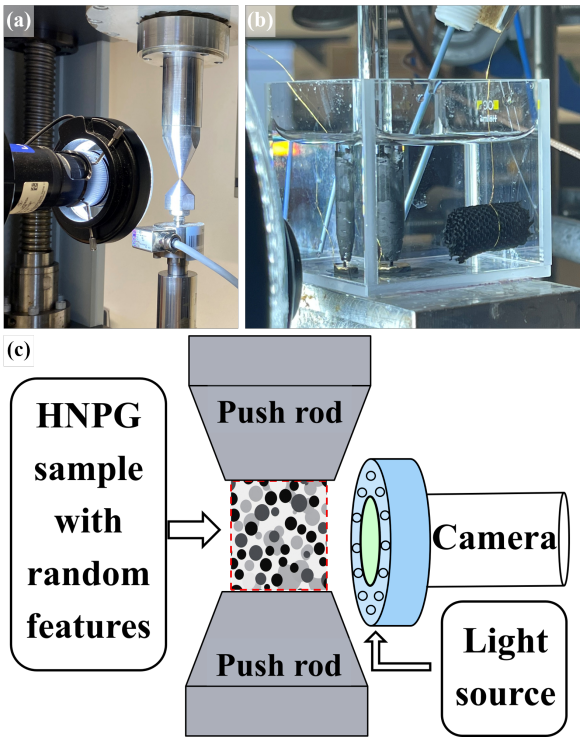


Figure 3.8: Mechanical characterization for HNPG and np Pd/np PdAu samples. (a) Photo of the setup for HNPG. A high-precision/high-speed camera and a matching adjustable illumination device. The sample to be tested is placed between the conical push rods of a universal mechanical testing device, which are designed to provide an enhanced illumination on the surface of the sample being tested; (b) In situ compression setup used for np Pd and np PdAu samples, featuring a transparent electrochemical cell to allow hydrogen charging under potentiostatic or open-circuit conditions. Details are described in Sec. 3.2.2 and (c) Simplified schematic diagram of the setup, illustrating that the random characteristics of the sample surface are created using artificial spray paint to enhance contrast and allow more accurate DIC analysis.

In situ electrochemical hydrogen absorption/desorption tests:

For selected np Pd and np PdAu samples, in situ hydrogen absorption/desorption experiments were performed using a thermostated three-electrodes electrochemical cell in 1.0 M H_2SO_4 electrolyte (Figure 3.9). Previous to each experiment, the electrolyte was purged with high-purity Ar gas for 40 min to remove dissolved oxygen. The nanoporous Pd and PdAu sample served as the WE, a standard hydrogen electrode (SHE, Gaskatel) was used as the RE and a carbon cloth was used as the CE. Hydrogen absorption within the samples was controlled by applying a fixed potential relative to SHE, enabling precise tuning of x_H during subsequent mechanical testing.

Hydrogen absorption and determination of x_H were carried out following a well-defined potentiostatic protocol. For each target x_H, imposed via a selected electrode potential (typically between 120 and 41 mV vs. SHE), the sample was held for at least 1 h prior to mechanical loading. This equilibration period allowed hydrogen absorption to approach equilibrium at fixed potential prior to deformation. Mechanical loading–unloading tests were then performed under the same applied potential, such that potential remained fixed throughout the elastic measurement. The elastic Poisson's

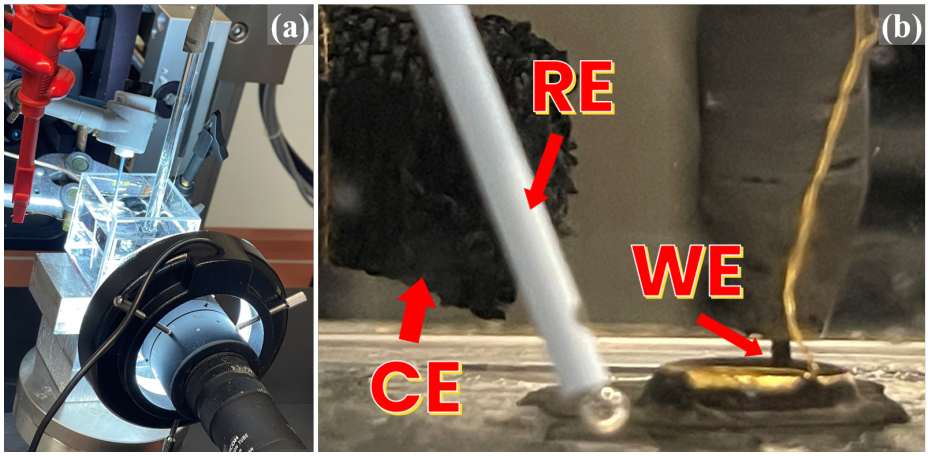


Figure 3.9: In situ electrochemical cell used for hydrogen absorption/desorption experiments on np Pd and np PdAu. (a) Overview of the customized three-electrodes setup used inside the in situ mechanical testing stage; (b) enlarged view showing the working electrode (WE), reference electrode (RE, SHE) and carbon cloth counter electrode (CE) during operation.

ratio was extracted from the unloading segments using full-field strain data obtained by DIC. After completion of the mechanical test at a given potential, the electrode potential was stepped to 260 mV (vs. SHE) for hydrogen desorption. 260 mV is the start potential of hydrogen adsorption [25]. The total desorption charge was integrated to determine the amount of absorbed/adsorbed hydrogen, from which the corresponding hydrogen concentration x_{H} was calculated. This procedure allows x_{H} to be determined independently of the mechanical response, while ensuring that the elastic measurements are conducted under well-defined open-system conditions at fixed chemical potential.

Digital image correlation: Digital image correlation (DIC) was employed to capture full-field strain distributions during uniaxial compression [27]. As a non-contact optical method, DIC enables sub-pixel resolution of surface displacements by tracking local grayscale features, allowing precise evaluation of both axial and transverse strains. These strain components serve as the basis for quantifying the elastic and plastic Poisson's ratios of the material.

To ensure reliable image correlation, homogeneous illumination and sufficient surface contrast were essential. A cylindrical push-rod setup was employed to create uniform lighting conditions across the sample surface. A high-contrast speckle pattern composed of black, white and grey paint was applied to generate random grayscale textures suitable for correlation, as illustrated in Figure 3.10a. The recorded images were analyzed using professional DIC software (DaVis, LaVision GmbH), which enabled sub-pixel tracking of surface displacements, with a displacement resolution on the order of a fraction of a pixel, depending on the imaging conditions and correlation parameters. During deformation, digital images were acquired at regular time intervals of 4 s, corresponding to an acquisition frequency of 0.25 Hz. Virtual strain gauges were defined within the region of interest to extract local axial strain (ε_{a}) in the loading direction and transverse strain (ε_{t}) perpendicular to it. A representative speckled image and the corresponding directions of strain measurement are indicated in Figure 3.10a, while Figures 3.10b and 3.10c display the full-field strain maps for ε_{t} and ε_{a}, respectively, obtained at an engineering strain of 10%.

Poisson's ratio was then calculated using the incremental strain ratio defined in Eq. 2.3 and evaluated separately in the elastic and plastic regimes. The theoretical background and definitions of elastic and plastic Poisson's ratios are provided in Sec. 2.2. Here, the elastic Poisson's ratio (ν_{E}) was extracted from cyclic loading–unloading tests, while the plastic Poisson's ratio (ν_{P}) was determined from continuous compression tests [27, 28, 161]. Given the bicontinuous and statistically homogeneous microstructure of the nanoporous networks, surface strains measured by DIC are taken as representative of the bulk mechanical response.

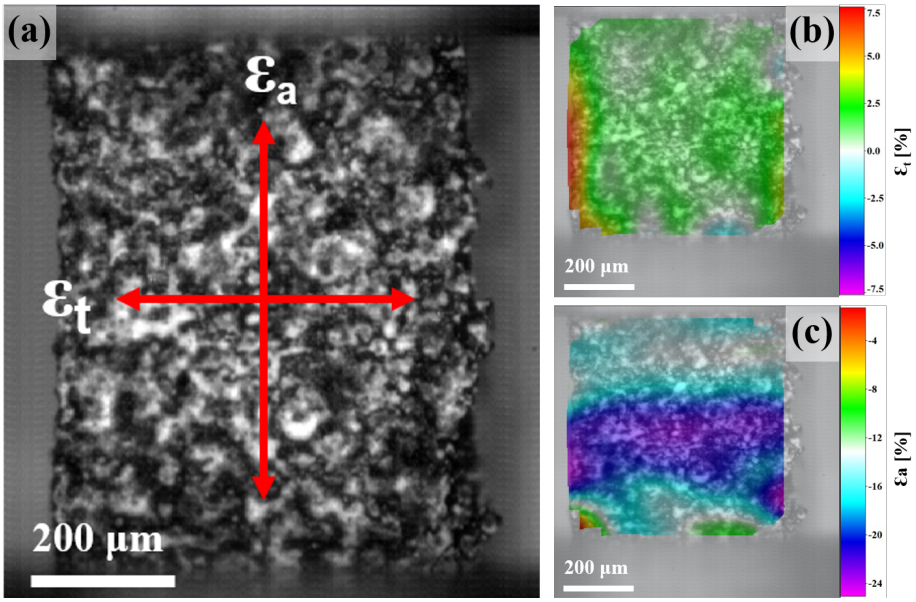


Figure 3.10: The digital image correlation (DIC) setup. (a) A high-resolution image of one HNPG sample under the camera with proper exposure and focus to ensure the accuracy of DIC analysis. ε_{t} and ε_{a} represent the transverse and axial strain respectively. Virtual strain gauge maps of (b) ε_{t} and (c) ε_{a} when the engineering strain is 10%.

Chapter Summary

This chapter introduced the experimental procedures for preparing and characterizing nanoporous gold and Pd-based alloys. Hierarchical structures were obtained via multi-step dealloying and thermal treatments. Ligament size and solid fraction were tuned electrochemically. Structural features were assessed by SEM, EDX, XRD and TEM. Mechanical properties were extracted via uniaxial compression with digital image correlation. These well-established protocols form the experimental foundation for the analyses of mechanical properties of HNPG and np Pd/np PdAu-H systems.

Chapter 4

Poisson's Ratio in Hierarchical Nanoscale Networks

Hierarchical nanoporous metals offer a unique platform for studying stiffness and strength in three-dimensional nanoscale networks with hierarchical microstructures [22, 100], yet their Poisson's ratio, which governs the coupling between axial and transverse strains, remains unexplored. While Chapters 2 outlined the scaling laws for Poisson's ratio in hierarchical network, however the Poisson's ratio of HNPG has not been systematically explored.

In this chapter, we examine the elastic and plastic Poisson's ratios of HNPG, in which the solid volume fraction and upper level ligament size can be tuned independently. Using in situ digital image correlation combined with uniaxial compression, we map the transverse and axial strain fields across a controlled set of microstructures to isolate the effects of solid fraction, ligament sizes and applied strain on mechanical response. Our measurements show that both elastic and plastic Poisson's ratios are largely insensitive to upper level ligament size and to the magnitude of compressive strain. More importantly, we identify and experimentally validate a quantitative scaling relation linking the elastic Poisson's ratio to the solid volume fraction. This scaling behavior reveals a geometry-controlled origin of the elastic Poisson's ratio in hierarchical networks and clarifies how structural hierarchy governs effective elasticity.

4.1 Results

4.1.1 Microstructure

The evolution of the microstructure in both NPSG (Figure 4.1a-d) and HNPG (Figure 4.1e-h) samples as a function of the annealing temperature T_a during Stage II was systematically characterized using SEM, which provides the microstructural basis for understanding the mechanical response of the hierarchical networks. Figure 4.1a-d illustrates that the ligament sizes of NPSG samples increase progressively from 70 nm to 180 nm as T_a increases from 300 °C to 450 °C. Similarly, Figure 4.1e-h demonstrates that the upper level ligament sizes (L_2) of HNPG follow the same trend, increasing with T_a in a comparable manner. It can be observed that L_2 of HNPG remain nearly unchanged compared to their corresponding NPSG precursors, except for the sample

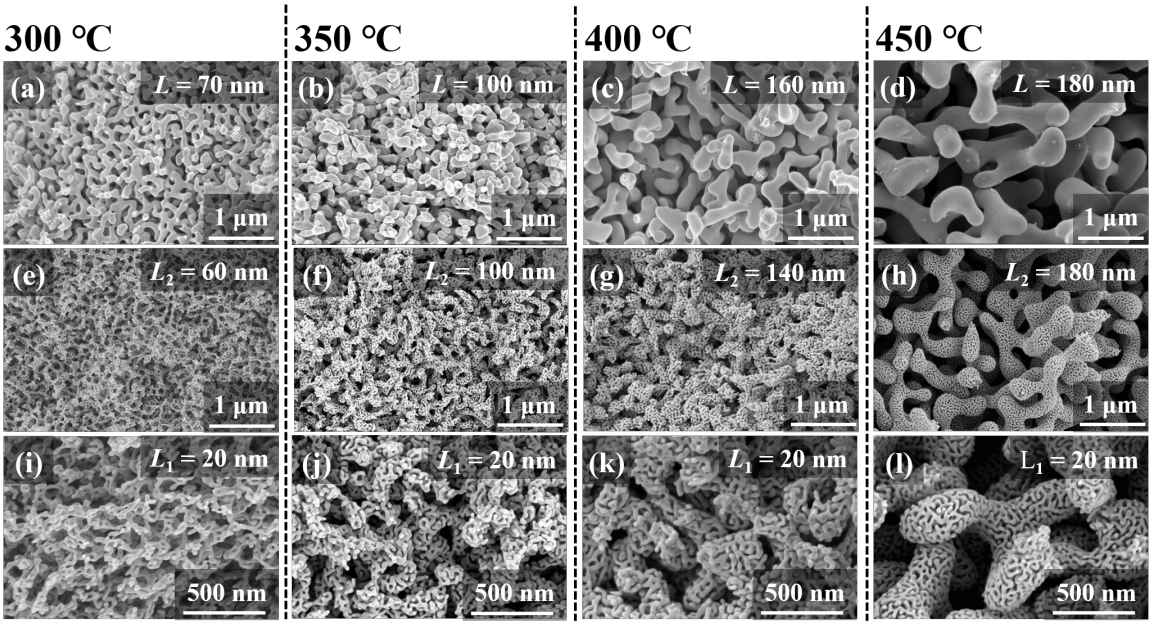


Figure 4.1: Microstructure of NPSG alloy and HNPG samples at different annealing temperatures. (a-d): SEM images of NPSG alloy annealed at 300 °C, 350 °C, 400 °C and 450 °C, respectively, showing ligament sizes of 70 nm, 100 nm, 140 nm and 180 nm. (e-h) SEM images of the HNPG samples dealloyed out of NPSG alloy samples in (a-d), showing the same lower level ligament size (L_1) of 20 nm, while the upper level ligament size (L_2) retain the original ligament size of the corresponding NPSG alloy; (i-l) Further zoom in (e-h), which show more details of lower level ligament.

annealed at 300 °C, where a slight reduction from 70 nm to 60 nm is detected. The preservation of the upper level ligament size during the second dealloying suggests that the solid volume fraction of the upper hierarchy (φ_2) remains nearly constant, thereby providing a reliable basis for calculating the solid fractions at each hierarchical level in HNPG.

To provide a clearer view of the upper level ligament morphology, Figure 4.1i-l presents higher-magnification SEM images corresponding to the regions highlighted in Figure 4.1e-h. These enlarged views reveal the detailed geometry and surface roughness of the upper level ligaments, confirming that their microstructural characteristics are well preserved across different annealing temperatures.

The mean values of L_1 and L_2, determined from measurements on at least ten samples for each synthesis condition, are summarized in Table 4.1. By contrast, all HNPG samples exhibit a constant lower level ligament size of $L_1 = 20$ nm, independent of T_a, which results from the identical dealloying conditions applied during Stage III. EDX measurements reveal that the residual Ag content in NPSG and HNPG samples is 75 ± 1 at% and less than 2 at%, respectively.

Table 4.1 also summarizes the net solid volume fraction (φ_{net}) of the investigated NPSG and HNPG samples. φ_{net}, or relative density, of the as-prepared NPSG and HNPG samples was determined by measuring the mass and volume of the samples. Under the assumption of a constant solid volume fraction for the upper hierarchical level structure during annealing and Stage III, the solid volume fraction at the upper

Table 4.1: Structural parameters of the HNPG samples.

T_a (°C)	φ_{net}		φ_1		φ_2		L_1 (nm)	L_2 (nm)
300	0.146	± 0.013	0.457	± 0.021	0.319	± 0.020	20 ± 2	60 ± 3
350	0.131	± 0.014	0.402	± 0.022	0.327	± 0.019	20 ± 2	100 ± 9
400	0.129	± 0.020	0.385	± 0.028	0.336	± 0.021	20 ± 2	140 ± 11
450	0.126	± 0.015	0.390	± 0.035	0.322	± 0.046	20 ± 2	180 ± 12

Note: T_a, annealing temperature. The data for solid volume fraction and ligaments size take the mean value of at least 10 samples. φ_1 and φ_2 denote solid volume fraction of the lower and upper level hierarchical structures, respectively. φ_{net} denotes net or total solid volume fraction of HNPG, where $\varphi_{net}=\varphi_1\times\varphi_2$.

hierarchical level (φ_2) is assumed to be equal to the φ_{net} of the corresponding NPSG samples. The values and error bars for φ_{net} and φ_2, as listed in Table 4.1, were obtained from measurements on at least ten samples for each synthesis condition. The relationship between the solid volume fractions of the lower and upper hierarchical levels is expressed as:

$$\varphi_2 = \frac{\varphi_{net}}{\varphi_1} \tag{4.1}$$

It is found that HNPG samples with the smallest $L_2 = 60\,\text{nm}$ exhibit the highest φ_{net} of 0.146, whereas samples with larger L_2 exhibit φ_{net} values in the range of 0.126 to 0.131. This trend is consistent with the variations in φ_2 for HNPG samples and the φ_{net} of the corresponding NPSG samples. During the dealloying process, nanoporous gold can densify near its external surface, as reported in previous studies [159]. The sample with $L_2 = 60\,\text{nm}$ exhibits a higher φ_1 and thus a larger φ_{net}, the smaller upper level ligaments place a larger fraction of the lower level ligaments closer to the external surface compared to the other samples [159].

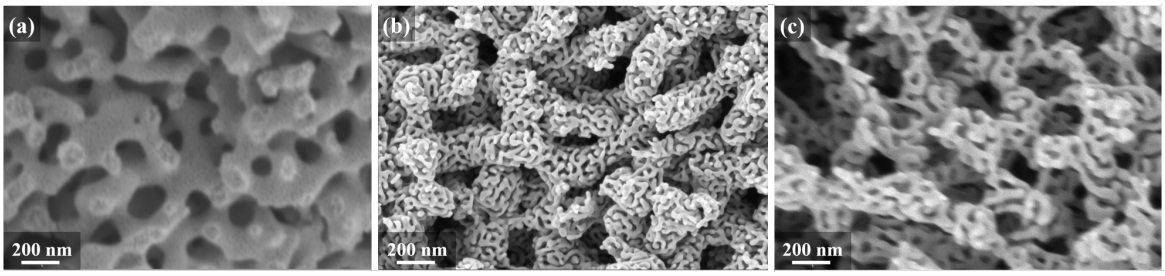


Figure 4.2: SEM images of HNPG samples with same upper level ligament size, $L_2 = 140\,\text{nm}$ and different lower level ligament size L_1. (a) $L_1 < 20\,\text{nm}$; (b) $L_1 = 20\,\text{nm}$ and (c) $L_1 = 40\,\text{nm}$.

Figure 4.2 shows SEM images of the HNPG samples with a fixed upper level ligament size ($L_2 = 140\,\text{nm}$) but different lower level ligament sizes L_1 of <20 nm, 20 nm and 40 nm. These samples are used to investigate the influence of L_1 on the mechanical properties while keeping L_2 constant. EDX analysis reveals a relatively high residual Ag content of approximately 16 at% in the sample with $L_1 < 20\,\text{nm}$, whereas samples with $L_1 = 20\,\text{nm}$ and $L_1 = 40\,\text{nm}$ contain less than 2 at.% residual Ag.

4.1.2 Mechanical properties

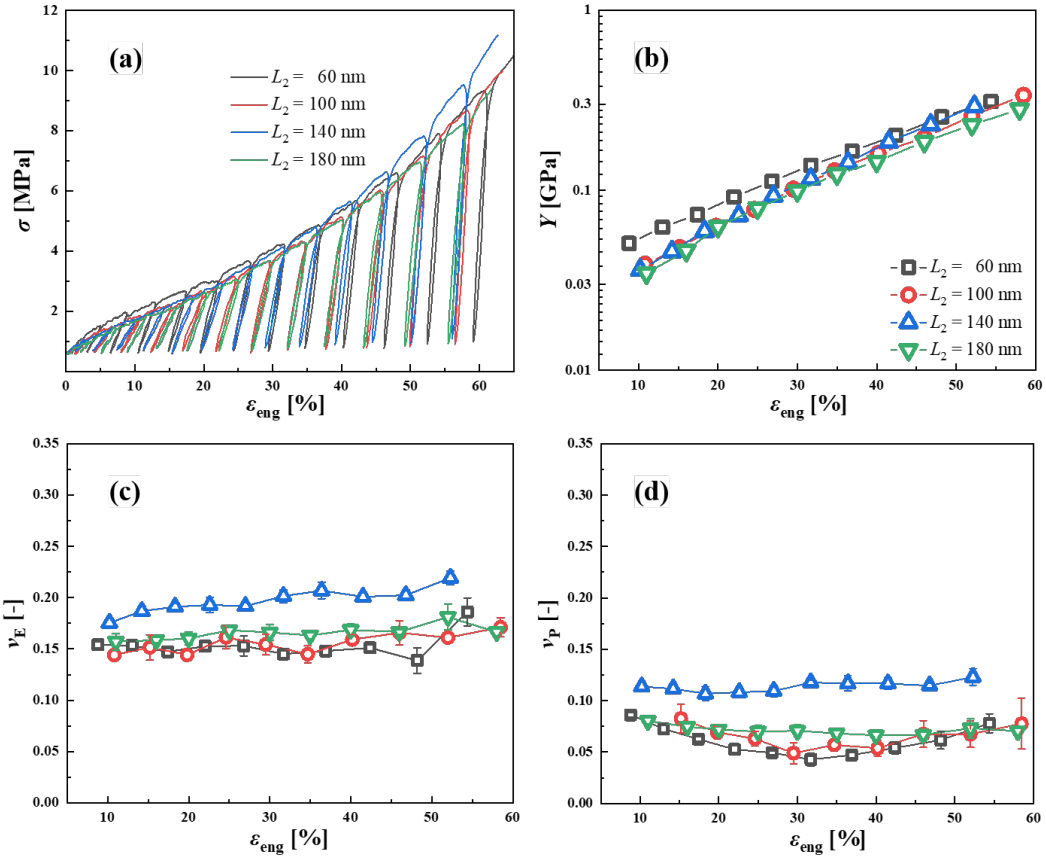


Figure 4.3: Results of uniaxial loading/unloading compression test of 4 representative HNPG samples with different L_2 varying from 60 nm to 180 nm and approximate initial solid volume fractions of 0.144, 0.142, 0.141 and 0.142, respectively. (a) Engineering stress-strain curves (σ - ε_{eng}). The zoomed image shows a loading/unloading segment; (b) The log-linear plot of Young's modulus Y as a function of engineering strain ε_{eng}; (c) Elastic Poisson's ratio (ν_{E}) as a function of engineering strain (ε_{eng}) and (d) Plastic Poisson's ratio (ν_{P}) as a function of ε_{eng}. The error bars represent the standard deviation, which are the max and min values of measured ν_{E} and ν_{P} during each elastic and plastic deformation stage.

Uniaxial compression experiments were conducted on millimeter-scale HNPG specimens using a conventional universal mechanical testing machine, as schematically illustrated in Figure 3.8a. The mechanical response was characterized by evaluating Young's modulus (Y) and both the elastic and plastic Poisson's ratios (ν_{E} and ν_{P}), based on strain field measurements from more than 40 defect-free HNPG samples. All specimens used in this parts shared a uniform lower level ligament size of $L_1 = 20$ nm. The upper level ligament sizes L_2 ranged from 60 nm to 180 nm, while the corresponding structural parameters including total network solid volume fraction (φ_{net}) and hierarchy-specific fractions φ_1 and φ_2 are summarized in Table 4.1. For all mechanical tests, the applied compressive strain exceeded 60%, but in the subsequent analysis, we restrict our attention to the deformation regime within the initial 35% strain, where the DIC has best analyzing accuracy.

Figure 4.3a presents representative engineering stress–strain curves obtained from four HNPG samples, each with a distinct L_2 (60 nm to 180 nm), but close φ_{net} values (~0.142). All curves demonstrate substantial plasticity without macroscopic cracking or failure up to 60% strain. The monotonic rise in flow stress with increasing strain is attributed to the combined effects of strain hardening and densification-induced changes in the φ_{net}. The mechanical parameters Y, ν_{E} and ν_{P} extracted from the same compression sequences are shown in Figs. 4.3b–d.

As shown in Figure 4.3b, Y increases progressively with compressive strain for all samples, in agreement with the increase in effective solid volume fraction caused by densification. Interestingly, despite similar φ_{net} values, the sample with the smallest upper level ligament ($L_2 = 60$ nm) exhibits a slightly higher modulus than the other specimens. This discrepancy is likely related to variations in network connectivity retained after thermal annealing, with larger L_2 samples experiencing more pronounced topological degradation due to coarsening [147, 162].

Figure 4.3c and d depict the evolution of ν_{E} and ν_{P} as a function of compressive strain, respectively. In contrast to the pronounced increase in Y, both Poisson's ratios remain nearly constant throughout deformation, irrespective of L_2. A modest upward trend in ν_{E} is observed at higher strains, reaching $\varepsilon_{\text{eng}} = 60\%$. For ν_{P}, the trend is slightly more complex: an initial decrease is followed by a mild increase beyond $\varepsilon_{\text{eng}} = 30\%$. These subtle but distinct behaviors suggest that while densification and morphological evolution under strain enhance stiffness, they have comparatively minor and nonlinear influence on the material's transverse strain response.

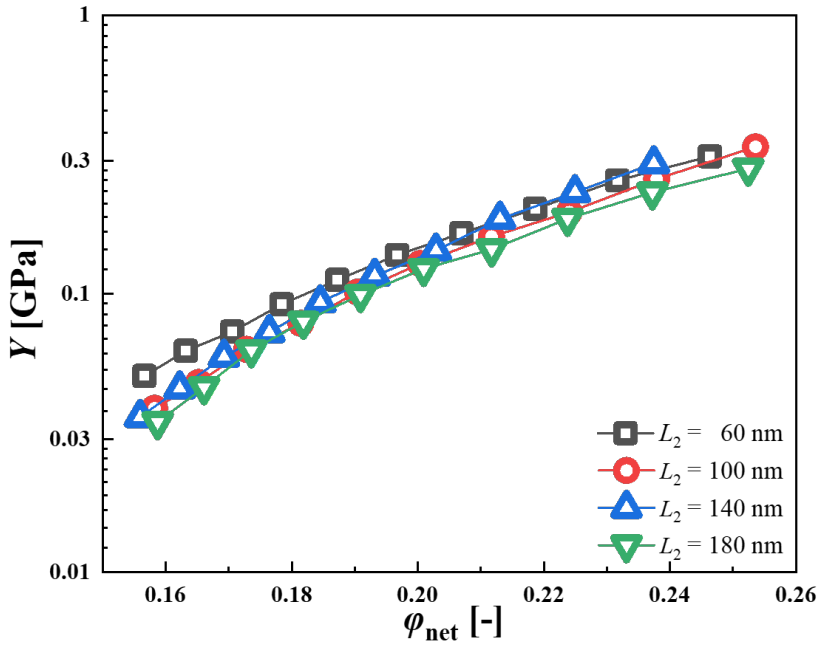


Figure 4.4: The log-linear plot of HNPG's Y as a function of the φ_{net} at different compressive strains. The four HNPG samples have an approximately same initial $\varphi_{\text{net}} = 0.142$ and L_2 vary from 60 nm to 180 nm.

Figure 4.4 presents the relationship between Young's modulus Y and the evolving φ_{net} for the four representative HNPG samples previously discussed in Figure 4.3.

The corresponding φ_{net} for each ε_{eng} can be calculated by the change of samples' volume, which could obtained from axial+transverse strain. All samples initially possess comparable φ_{net} values near 0.142 but exhibit distinct upper level ligament sizes L_2 ranging from 60 nm to 180 nm. Upon progressive compressive deformation to strains approaching 60%, densification leads to an increase in φ_{net} to approximately 0.26 across all samples.

A clear increase in Y with φ_{net} is observed for each sample, consistent with the expectation that an increase in solid fraction enhances the effective stiffness of the porous network. More notably, the Y–φ_{net} curves for all four samples exhibit progressive convergence as deformation proceeds. This convergence indicates a diminishing influence of initial topological differences associated with varying L_2. The observed convergence behavior suggests that the densification leads to new structural connections, which effectively restore or homogenize the connectivity among samples, irrespective of their initial hierarchical morphology. In other words, deformation-induced reconnection appears to compensate for connectivity loss that may have arisen from coarsening or fragmentation during the thermal annealing stages. As a result, the mechanical response at high φ_{net} becomes largely governed by the densified microstructure rather than the original hierarchical microstructure.

Figure 4.5 illustrates how the elastic Poisson's ratio ν_{E} evolves with the solid volume fraction φ_{net} in HNPG samples featuring systematically varied upper level ligament sizes L_2 from 60 nm to 180 nm. The measurements were performed under uniaxial compressive strains up to 35%. In each subplot (a–d), the open data points correspond to the same four representative samples previously introduced in Figure 4.3, each characterized by a distinct L_2 but with comparable initial φ_{net} values (approximately 0.142).

Despite a substantial increase in φ_{net} resulting from compressive densification up to 35%, the measured elastic Poisson's ratio ν_{E} exhibits a surprisingly invariant trend across all HNPG samples. This behavior persists even as the network microstructure undergoes significant morphological changes, including increased φ_{net} and improved connectivity. While such changes are typically expected to influence bulk mechanical properties, ν_{E} remains confined within a narrow range, with only minor upward shifts at larger φ_{net}. This observation suggests a potential decoupling between stiffness (as reflected in Young's modulus) and lateral strain response in hierarchical porous structures. The statistical spread, visualized by the yellow shaded regions in Figure 4.5, further underscores the reproducibility and consistency of ν_{E} trends across different synthesis conditions. Possible mechanistic origins of this invariance are explored in Section 4.2.

To ensure statistical robustness and to evaluate the reproducibility of this behavior, additional datasets were acquired for each L_2, resulting in at least 10 samples per category. Across all L_2 values, ν_{E} falls within a narrow range of 0.11–0.21 throughout the φ_{net} = 0.14–0.22 regime as shown in Figure 4.6. In the low φ_{net} regime (0.14 – 0.16), which corresponds to early deformation, most samples exhibit $\nu_{\text{E}} \approx 0.15$, consistent with literature reports on non-hierarchical nanoporous gold [27]. A modest but noticeable deviation is observed for samples with L_2 = 140 nm, where slightly elevated ν_{E} values are recorded. This minor variation is likely attributable to microstructural differences, such as local loss of inter-ligament connectivity or uneven coarsening, which are known to emerge during thermal annealing.

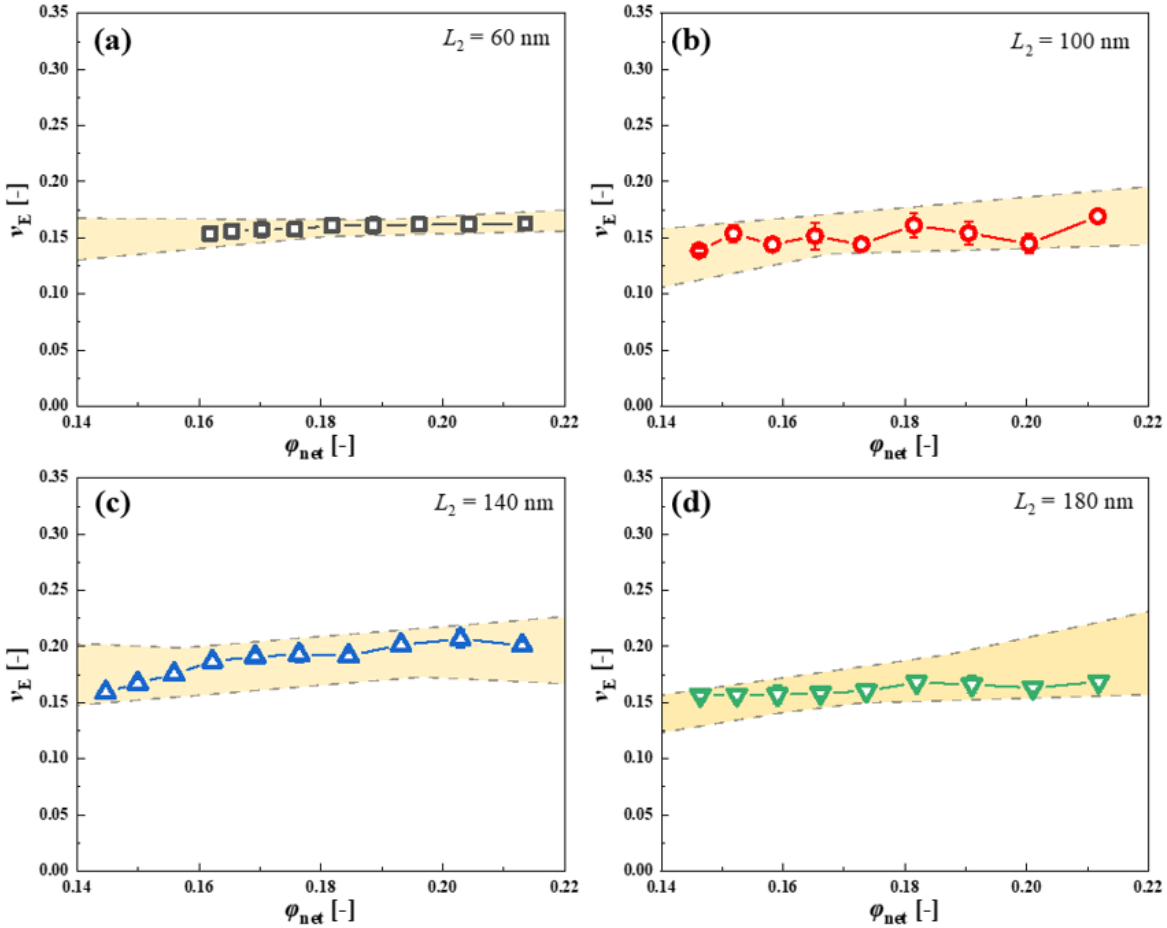


Figure 4.5: The variations in the ν_E of HNPG with different L_2 as a function of φ_{net} evolution are presented. (a), (b), (c) and (d) ν_E for HNPG samples with L_2 ranging from 60 nm to 180 nm. The yellow-shaded region in each figure represents the spread of ν_E for at least 10 samples, with the upper and lower boundaries defined by the maximum and minimum values at the corresponding φ_{net}. Additionally, the ν_E of a representative sample is included within each shaded region. The error bars represent the standard deviation, which are the max and min values of measured ν_E during each elastic deformation stage.

Figure 4.7a–d depicts the evolution of the elastic Poisson's ratio ν_E as a function of engineering strain ε_{eng} for HNPG samples with different upper level ligament sizes L_2. Each figure corresponds to a distinct L_2 value, ranging from 60 nm to 180 nm. The shaded yellow regions represent the full spread of ν_E measured from at least 10 independent samples per condition. Superimposed open symbols indicate results from a representative sample, with accompanying error bars denoting the maximum and minimum ν_E values recorded within each elastic loading interval. Across all samples and ligament sizes, ν_E remains approximately constant at ~0.15 for engineering strains up to 35%. The near invariance of ν_E supports the earlier observation in Figure 4.5, reinforcing the notion that, unlike the Y, ν_E is relatively insensitive to densification-induced changes in φ_{net} during early-stage compression.

Figure 4.8 presents the evolution of the plastic Poisson's ratio ν_P as a function of φ_{net} for four representative HNPG samples with distinct upper level ligament sizes

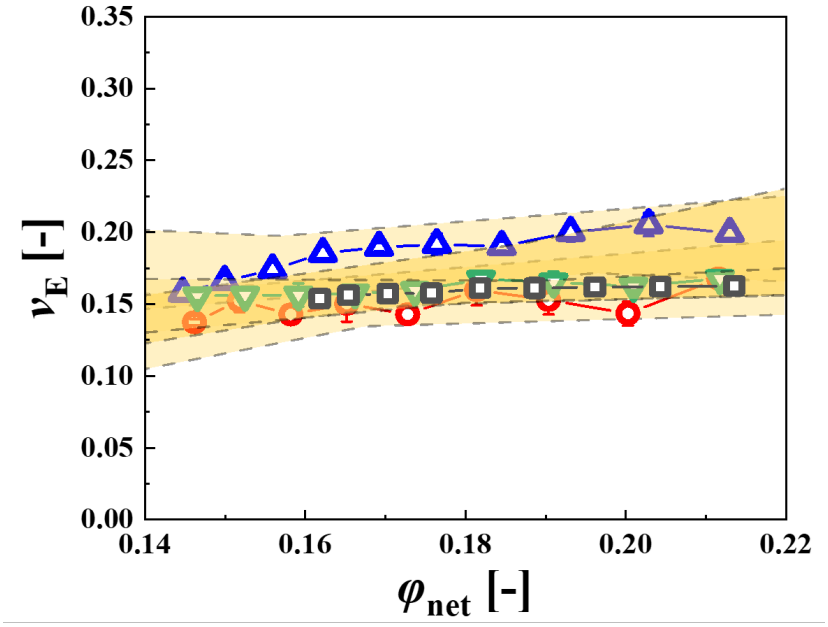


Figure 4.6: The variations in the ν_E of HNPG with different L_2 as a function of φ_{net} evolution from Figure 4.5 are presented together.

L_2 (60 nm to 180 nm), each prepared to have approximately the same initial φ_{net} (Figure 4.3 and Figure 4.4). ν_P were evaluated from the irreversible strain increments accumulated beyond the elastic unloading segments. Within the deformation range of φ_{net} = 0.15–0.22, the measured ν_P values span from approximately 0.05 to 0.12.

A sample-to-sample comparison reveals that the HNPG specimen with L_2 = 140 nm consistently exhibits slightly higher ν_P values across the full range of φ_{net}, mirroring the trend observed for elastic Poisson's ratio in Figure 4.6. This subtle enhancement in ν_P may be attributed to microstructural differences such as connectivity loss or coarsening introduced during thermal treatment. The plastic Poisson's ratio exhibits greater variability with increasing φ_{net} than its elastic counterpart. This effect is particularly pronounced in samples with smaller L_2 values, where fluctuations in ν_P are more severe. Such behavior aligns with earlier observations in non-hierarchical NPG, where ν_P was found to be more sensitive to strain history and deformation pathway [27]. The present results suggest that plastic transverse strain responses are more susceptible to stochastic microstructural rearrangements than their elastic analogs, especially in finer hierarchical microstructures.

Figure 4.9 examines the influence of the lower level ligament size L_1 on the plastic Poisson's ratio ν_P under uniaxial compression, using HNPG samples with fixed upper-scale structure (L_2 = 140 nm). Figure 4.9a and b display ν_P as a function of engineering strain ε_{eng} and net solid volume fraction φ_{net}, respectively, for three different L_1 values: <20 nm, 20 nm and 40 nm.

Across the full range of deformation, the three samples exhibit very similar ν_P values, indicating negligible dependence on L_1. At small strain (e.g., $\varepsilon_{eng} \approx 10\%$ in Figure 4.9a) or equivalently low φ_{net} (≈0.16–0.17 in Figure 4.9b), the measured ν_P lies within 0.05–0.10, consistent with earlier results from samples with varied L_2 (see Figure 4.8) and the summary trends shown in Figure 4.10. Although some small variations in ν_P are present

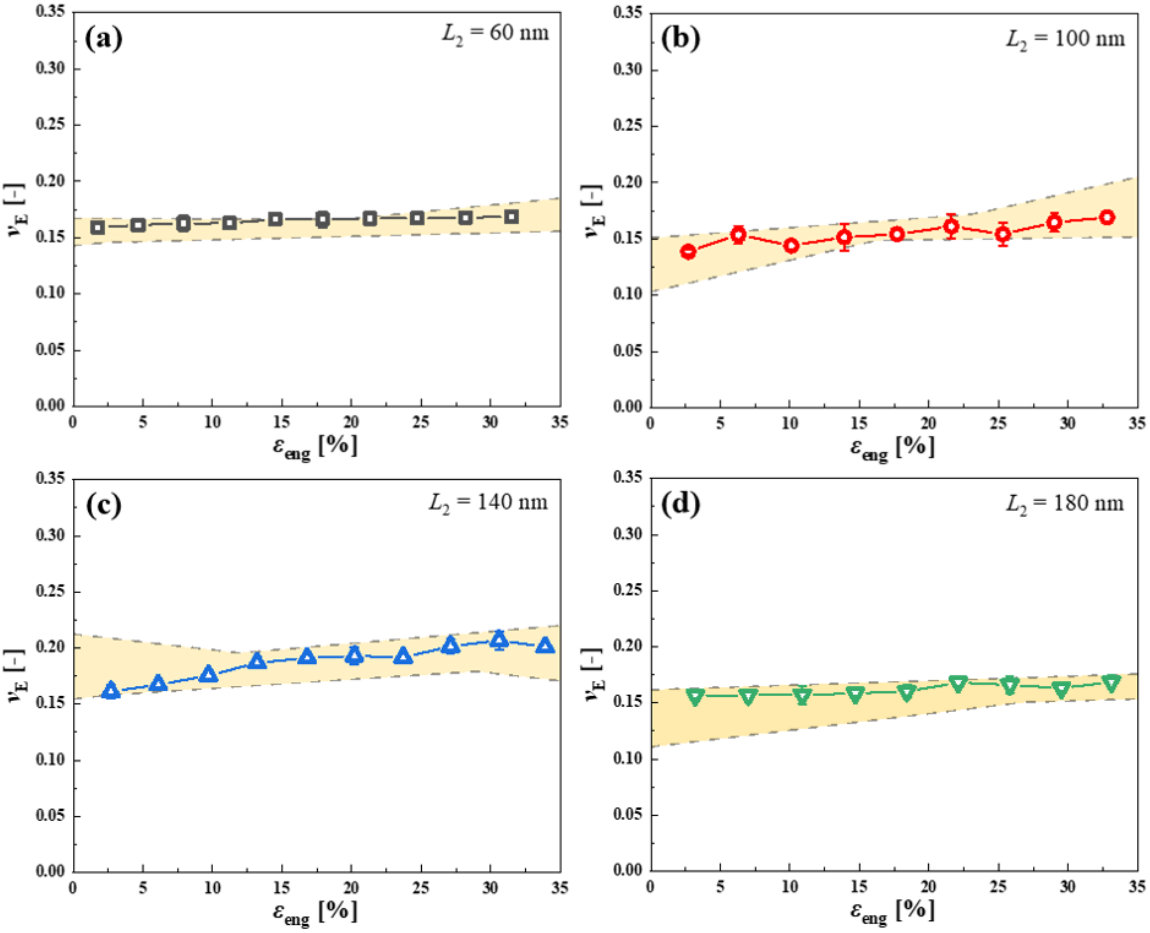


Figure 4.7: The variation of the elastic Poisson's ratio ν_E during compression. (a), (b), (c) and (d) ν_E versus engineering strain ε_{eng} for HNPG samples with L_2 sizes ranging from 60 nm to 180 nm. The yellow-shaded region in each figure represents the spread of ν_E for at least 10 samples, with the upper and lower boundaries defined by the maximum and minimum values at the corresponding ε_{eng}. Additionally, the ν_E of a representative sample is marked as open symbols within each shaded region. The error bars on open symbols represent the standard deviation, which are the max and min values of measured ν_E during each elastic deformation stage.

between the three L_1 conditions, these differences remain within the experimental uncertainty range and do not suggest a systematic size effect attributable to L_1. These findings reinforce the conclusion that ν_P in HNPG is relatively insensitive to structural variations at the lower hierarchical level, at least within the investigated regime.

4.2 Discussion

4.2.1 Impact of upper level ligament size

Based on mechanical measurements performed on HNPG samples with varied upper level ligament sizes L_2 and similar lower level ligament sizes L_1, the influence of L_2 on ν_E, ν_P, Y and φ_{eff} are systematically analyzed, as summarized in Figure 4.10. For consistency

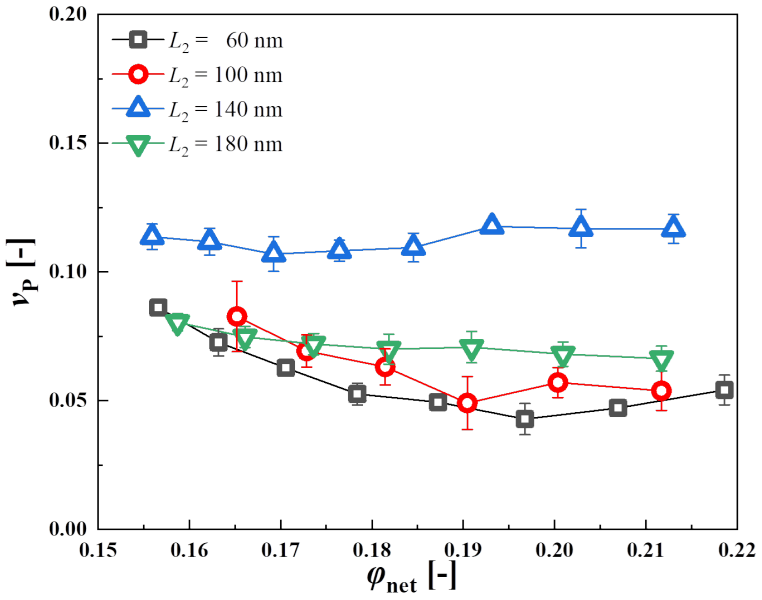


Figure 4.8: The variations of the ν_P of 4 representative HNPG samples with different L_2, ranging from 60 nm to 180 nm and approximate initial φ_{net}, are shown as a function of φ_{net}. The error bars represent the standard deviation, which are the max and min values of measured ν_P during each plastic deformation stage.

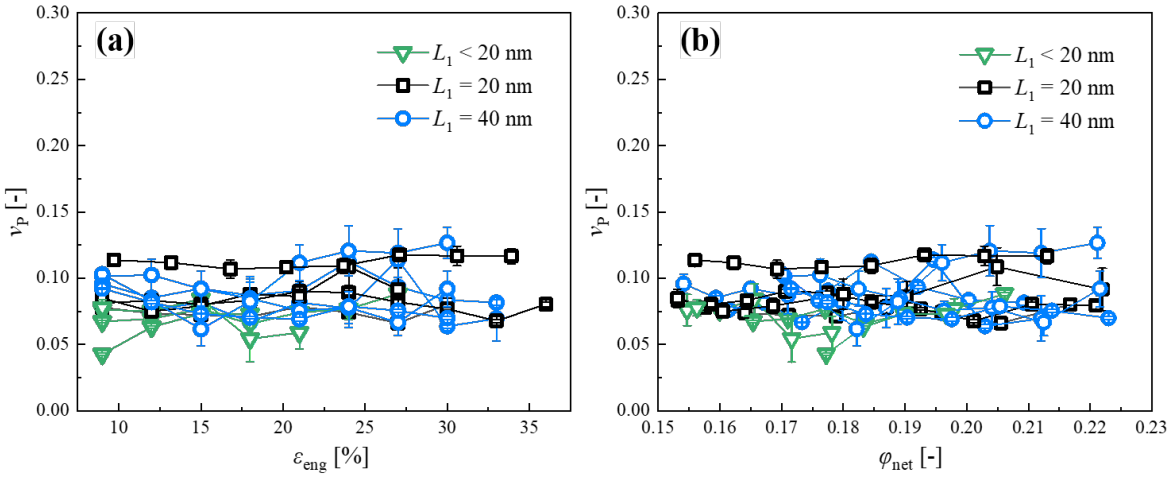


Figure 4.9: The variation of the plastic Poisson's ratio ν_P during compression for hierarchical nanoporous gold with $L_2 = 140$ nm and $L_1 < 20$ nm (green triangles), 20 nm (black squares) and 40 nm (blue circles). (a) ν_P vs. engineering strain ε_{eng}; (b) ν_P vs. net solid fraction φ_{net}. Data points include error bars (one standard deviation) for each series.

and comparison, both Poisson's ratios and Y are evaluated at 10% engineering strain (ε_{eng} = 10%) and plotted as functions of L_2. Each data point represents the average of at least ten independently prepared HNPG samples, with error bars denoting the maximum and minimum values observed within each set.

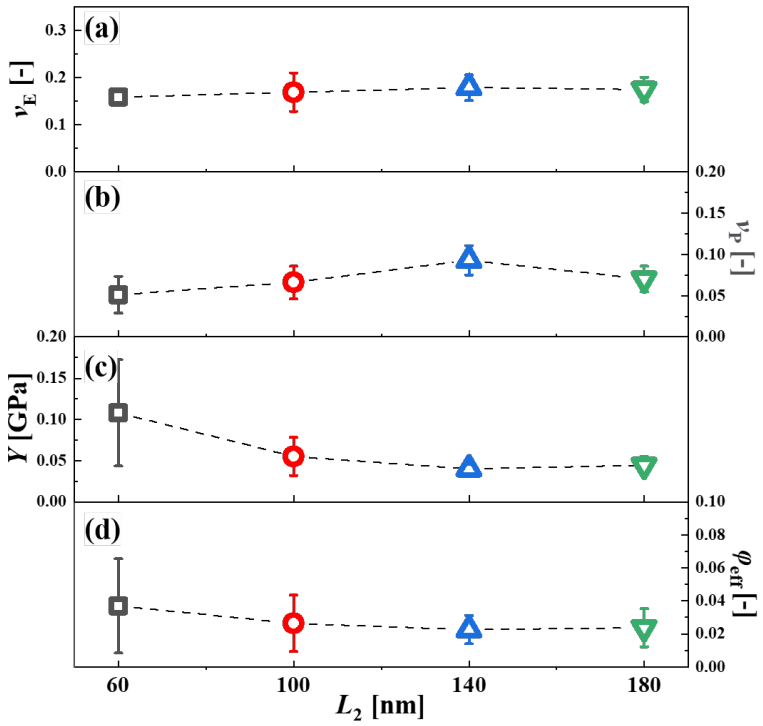


Figure 4.10: Average values of ν_E, ν_P, Y and φ_{eff} at 10% ε_{eng} as a function of L_2. (a) ν_E; (b) ν_P; (c) Y and (d) φ_{eff}. φ_{eff} is calculated from the Y using Eq. 4.2. Each data point represents the average value of at least 10 HNPG samples, with an error bar showing the max and min values.

As shown in Figure 4.10a, within the investigated range of L_2 from 60 nm to 180 nm, the ν_E exhibits no discernible dependence on the upper level ligament size. The average values of ν_E remain consistently close to 0.15 across all L_2 values. This observation is in agreement with the earlier study by Lührs et al. [27], which reported a size-independent ν_E in monolithic nanoporous gold (NPG) with constant φ_{net} = 0.25 and ligament sizes ranging from 50 nm to 180 nm.

Compared to monolithic NPG, however, the HNPG samples investigated here show larger error bars, especially for smaller L_2 values. This variability is likely attributable to sample-to-sample variations in φ_{net}, as also reflected by the solid fraction scatter reported in Table 4.1. Although previous work has demonstrated that HNPG exhibits enhanced specific stiffness and strength relative to NPG, the absolute values of stiffness and strength are lower in our HNPG samples. This discrepancy arises primarily from their significantly reduced relative density—approximately half that of the monolithic NPG structures examined by Lührs et al. [27]. In addition to density effects, the smaller physical dimensions of HNPG ligaments may increase their susceptibility to uneven plastic deformation, induced either during dealloying or by mechanical handling. Such deformation can result in varying degrees of shrinkage and irreversible densification, leading to inconsistencies in the measured φ_{net} and, consequently, in ν_E. Furthermore, especially at small L_2, variations in microstructural connectivity which is stemming from differences in coarsening behavior may further contribute to the observed spread in elastic Poisson's ratio.

Similar to the weak size dependence observed for ν_E in Figure 4.10a, Figure 4.10b

shows that the plastic Poisson's ratio ν_P remains nearly constant at approximately 0.075 across the range of L_2 studied. This value is roughly half of the corresponding ν_E and does not exhibit a clear trend with respect to upper level ligament size. The consistency in ν_P can be reasonably attributed to the uniformity of the lower level ligament size L_1 among these samples, which is known to govern plastic deformation characteristics such as transverse strain in uniaxial compression. The lower-scale microstructure likely dominates the irreversible deformation behavior, thereby mitigating the influence of upper level structural variation. Minor differences in ν_P among samples may nonetheless arise due to fluctuations in network connectivity and local variations in solid volume fraction. These structural inhomogeneities can affect the redistribution of plastic strain during deformation, although their effect appears secondary compared to that of L_1.

In addition to the influence of L_2, the effect of lower level ligament size L_1 on ν_P was systematically investigated by varying L_1 to below 20 nm and up to 40 nm, while maintaining a fixed upper level ligament size of $L_2 = 140$ nm (Figure 4.2). As shown in Figure 4.9, the resulting values of ν_P for both sets of samples remain within the range of 0.05–0.10, consistent with those of HNPG samples with $L_1 = 20$ nm. This result stands in contrast to the pronounced size dependence reported for non-hierarchical NPG by Lührs et al. [27, 28], where decreasing ligament size led to a significant reduction in ν_P. In the case of HNPG, however, no clear trend is observed between L_1 and ν_P across the studied range. This apparent insensitivity may reflect the fact that modifying L_1 inherently introduces concurrent variations in other microstructural attributes, including residual Ag composition and topological arrangement. For example, HNPG with $L_1 < 20$ nm retains up to 16 at.% residual Ag, while coarsening to achieve $L_1 = 40$ nm is accompanied by a reduced L_2/L_1 ratio—both of which are known to influence network connectivity [22, 147, 163].

A similar structure-insensitive behavior of ν_P was reported by Liu et al. [164]. Beyond ligament size, several other parameters—including connectivity, residual silver distribution and solid fraction—can co-evolve during coarsening. As these factors often vary simultaneously and interactively, isolating the contribution of any single variable remains a significant experimental challenge. Future studies with better-controlled microstructures and chemical homogeneity will be essential to decouple these interrelated effects and clarify the underlying mechanisms governing plastic Poisson's ratio in hierarchical nanoporous structures.

The dependence of Y on the upper level ligament size L_2 is presented in Figure 4.10c. Notably, HNPG samples with $L_2 = 60$ nm exhibit substantial variation in Y, in contrast to the more consistent values observed at larger L_2. This pronounced scatter is likely attributable to the small L_2/L_1 ratio, which is approximately 3 in these samples. Such a low hierarchical size ratio implies that each upper level ligament contains only a few lower level ligaments, leading to a non-representative volume element (RVE) at the lower hierarchy. Networks constructed from non-representative volumes inherently suffer from stochastic variations in connectivity, which propagate into fluctuations in mechanical responses such as Young's modulus and yield stress [163].

Small L_2/L_1 ratios are prone to producing a high fraction of dangling lower level ligaments at the periphery of the upper level network. These dangling ligaments do not contribute effectively to load transfer, thereby reducing the overall connectivity of the network at the lower scale and weakening the bulk stiffness. This phenomenon mirrors

the findings of Wu et al. [163], who demonstrated that in non-hierarchical NPG, the the micropillar diameter/ligament size ratio must exceed 20 to ensure representative mechanical behavior. When the ratio falls below 10, the modulus becomes highly scattered due to the emergence of numerous surface dangling ligaments and localized failure mechanisms. These insights support the current observation that, although all HNPG samples with $L_2 = 60\,\text{nm}$ share the same nominal upper level feature size, their mechanical responses diverge significantly. As L_2 increases (or equivalently, as $L_2/L_1 > 7$), the variability in Y across samples diminishes and eventually becomes negligible. This further suggests the critical role of structural representativeness in determining the mechanical uniformity of hierarchical microstructures.

In addition to its influence on lower level connectivity via the L_2/L_1 ratio, the upper level ligament size L_2 also directly affects the connectivity of the network at the upper hierarchical level. Computational simulations by Li et al. [147], along with experimental observations on NPG by Zandersons et al. [165], have revealed that coarsening in low solid volume fraction nanoporous structures is often accompanied by a progressive loss of network connectivity. This trend implies that increasing L_2, which corresponds to more extensive coarsening, leads to reduced topological integrity at the upper scale, ultimately diminishing the stiffness of the upper level network. Taken together, these results suggest that L_2 modulates network connectivity at both hierarchical levels: at the lower level via the L_2/L_1 ratio and at the upper level through coarsening-induced topological degradation. These combined effects account for the variations in mechanical stiffness observed among HNPG samples with fixed L_2 but differing microstructural connectivity.

To provide a quantitative indication of the overall network connectivity in HNPG, we estimated the effective solid volume fraction φ_{eff}, a concept introduced by Jin et al. [52], which links stiffness to structural connectivity via the following expression:

$$\varphi_{\text{eff}} = \left(\frac{Y}{Y_0}\right)^{0.5} \tag{4.2}$$

where Y is the experimentally measured Young's modulus of the HNPG sample and $Y_0 = 79\,\text{GPa}$ corresponds to the modulus of bulk gold [148]. As shown in Figure 4.10d, φ_{eff} spans a broad range from 0.010 to 0.065 for samples with the same $L_2 = 60\,\text{nm}$, reflecting considerable sample-to-sample variability in network connectivity.

With increasing L_2 or more precisely, increasing L_2/L_1, the scatter in φ_{eff} progressively diminishes, mirroring the trend observed for Y in Figure 4.10c. Once the structural hierarchy reaches $L_2/L_1 > 7$, both Y and φ_{eff} stabilize at approximately 0.05 GPa and 0.025, respectively. This saturation behavior aligns well with previous observations on HNPG reported by Shi et al. [22] and supports the notion that the mechanical homogenization requires a sufficiently large separation between hierarchical length scales.

Importantly, these findings suggest that network connectivity exerts a more pronounced influence on Young's modulus than on either ν_{E} or ν_{P}. While Poisson's ratios remain relatively insensitive to size or connectivity variations, Y and φ_{eff} respond strongly, highlighting their greater dependence on topological integrity across both hierarchical levels.

4.2.2 Impact of solid volume fraction

Scaling behavior of elastic Poisson's ratio:

Figure 4.11 presents the scaling behavior of the elastic Poisson's ratio ν_E as a function of the net solid volume fraction φ_{net} for both conventional nanoporous gold (NPG, $n = 1$) and hierarchical nanoporous gold (HNPG, $n = 2$). The plot includes a broad range of literature data for NPG—obtained through compression [16, 149], tension [20, 149] and ultrasonic measurements [166] on both microscale and macroscale specimens—as well as newly obtained data from compression tests on millimeter-scale HNPG samples in this work. Several existing scaling laws are also plotted for comparison, including the classical Gibson–Ashby equation [145], Soyarslan's logarithmic model [37] and the scaling law proposed in this study (Eq. 2.17).

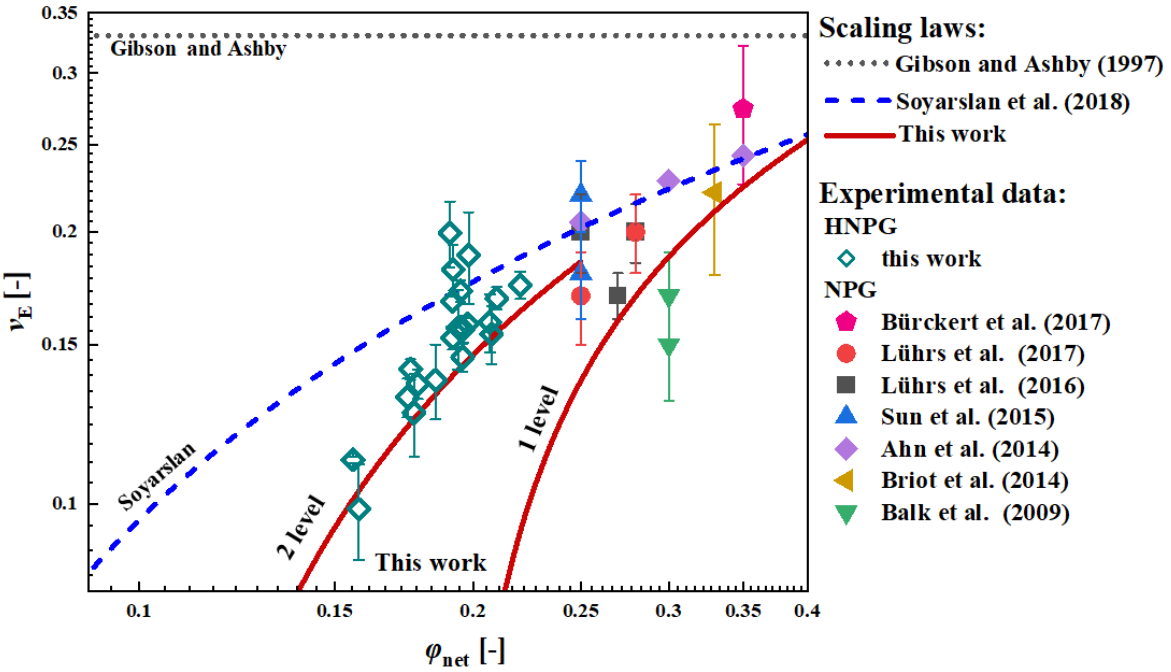


Figure 4.11: Scaling behavior of ν_E with respect to φ_{net} of nanoporous gold with different numbers of hierarchical levels. Close symbols: Literature experimental data, which were obtained from microscale NPG samples using compression testing [16, 149], tensile testing [20, 149] and ultrasonic testing techniques [166] and from compression tests on millimeter-sized NPG samples [27, 28, 150]. Open symbols: experimental data from compression tests on millimeter-sized HNPG samples in this work. Grey dot line: Gibson-Ashby equation, $\nu_E = 0.33$ [145]. Blue dash line: Soyarslan's law, $\nu_E = D_1 \ln\varphi_{net} + D_2$, where $D_1 = 0.116$, $D_2 = 0.363$ [37]. Red solid lines: Scaling law proposed in this work by Eq. 2.17, with $n = 1$ and $n = 2$, respectively. The error bars for HNPG take the max and min values of measured ν_E for each sample; the error bars for NPG are taken directly from literature.

As shown in the figure, the experimental data for both NPG and HNPG exhibit good agreement with the scaling law introduced in this work, particularly in the low-φ_{net} regime where other models tend to over predict ν_E. This comparison shows that the proposed scaling law captures the experimentally observed trend of the ν_E–φ_{net} relationship across different hierarchical levels more consistently. Eq. 2.17 extends the

applicability of Poisson's ratio scaling to hierarchical microstructures ($n > 1$), addressing a critical knowledge gap in understanding the structure–property relationships in multiscale nanoporous materials.

While the present study primarily emphasizes the correlation between Poisson's ratio and the overall solid volume fraction in HNPG, it is important to acknowledge that topological features such as network connectivity can also influence ν_E to a non-negligible extent. Previous studies have demonstrated that connectivity critically governs the mechanical stiffness of nanoporous metals [162] and its impact may become even more significant in low-density or heavily coarsened structures, irrespective of the presence of hierarchical features. Given the complex interplay between geometry, topology and mechanical response, further investigations that incorporate three-dimensional structural reconstructions [98, 167–169] alongside quantitative topological metrics [100, 139] are essential. Such studies will be instrumental in refining the current scaling laws and extending their applicability to a broader range of disordered nanoscale network materials beyond those fabricated by dealloying.

Comparison of plastic Poisson's ratio between HNPG and NPG:

Figure 4.12 compares the plastic Poisson's ratio ν_P of HNPG at ε_{eng} = 10% to literature-reported values for NPG across a range of solid volume fractions φ_{net} [14, 27, 28, 150, 170–172]. The data show significant scatter in ν_P for NPG at a given φ_{net}, which is not unexpected due to differences in testing methods and sample conditions, including geometry, deformation history and ligament size. Nonetheless, a general trend of decreasing ν_P with decreasing φ_{net} is evident. Monolithic NPG typically has $\varphi_{net} > 0.2$ and $\nu_P > 0.075$. Remarkably, the hierarchical structures studied here achieve both lower solid volume fractions (down to 0.11) and lower ν_P values than most previously reported nanoporous metals, highlighting their promise for tunable mechanical design.

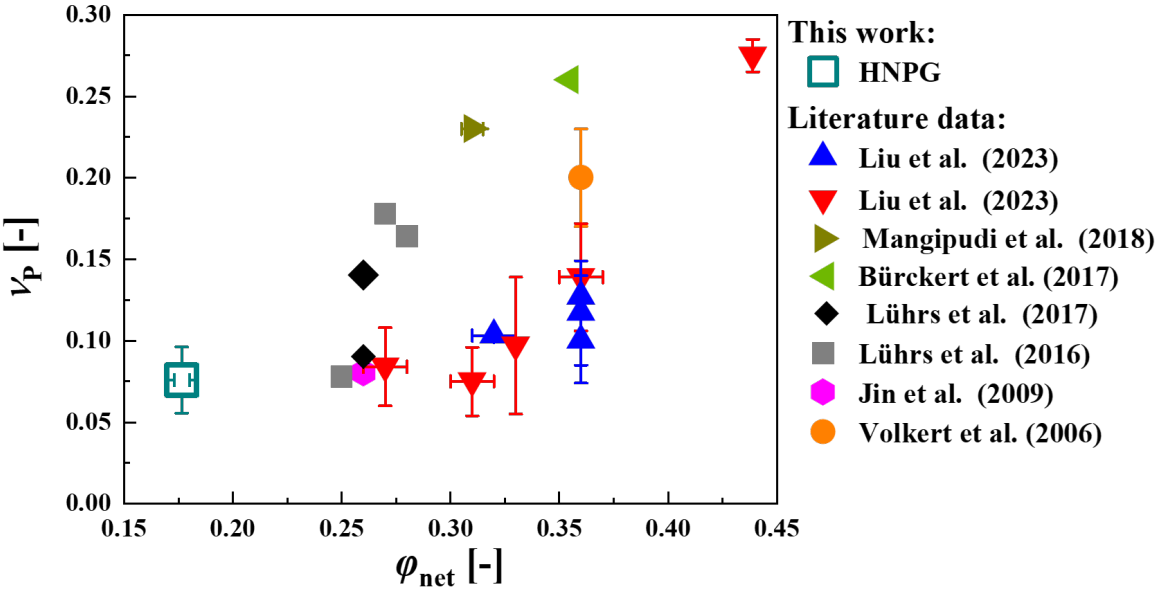


Figure 4.12: ν_P of HNPG as a function of φ_{net}, compared to ν_P of NPG from various sources in literature. The error bars for HNPG were obtained from at least 5 samples at ε_{eng} around 10%, indicating the max and min measured values, while the error bars for NPG samples are taken directly from literature.

Implications of plastic Poisson's ratio for Strength–Hardness Relationship:

Plastic Poisson's ratio is often considered an important parameter for estimating the hardness-to-yield strength ratio, $f = H/\sigma_y$, in porous and cellular materials. Reported values of f for NPG vary widely, typically ranging from 1.0 to 3.0 [18, 52, 164, 172, 173]. According to the empirical Shaw–Sata relation for porous solids [174], a ν_P of approximately 0.075 corresponds to $f = 2.0$. By contrast, continuum simulations by Miller [175] suggest that in low- to moderate-ν_P regimes, indentation hardness is nearly independent of ν_P and approximates the yield strength, implying $f \approx 1.0$. Deviations from this idealized value are often attributed to additional factors such as strain hardening.

Recent experimental results by Liu et al. [164] reinforce this interpretation, showing that for NPG with $\varphi_{net} < 0.3$, f is primarily governed by the strain hardening rate θ, rather than ν_P. All HNPG samples examined in this study exhibit pronounced strain hardening, supporting the use of Liu's modified relationship:

$$f = 1.33 + 0.11\frac{\theta}{\sigma_y} \tag{4.3}$$

where σ_y and θ are the yield strength and strain hardening rate, respectively. Using values extracted at $\varepsilon \approx 0.1$ for HNPG samples with $L_1 = 20\,\text{nm}$ and $L_2 = 60\text{–}180\,\text{nm}$, we obtain f values in the range of 1.76–1.92. This moderate deviation from $f \approx 1.0$ is consistent with the role of strain hardening in hierarchical microstructures and aligns well with recent findings in nanoporous metal systems.

4.2.3 Evolution of mechanical properties during compressive deformation

For NPG, it is well established that compressive deformation leads to an increase in Y, primarily due to densification-induced enhancement of the solid volume fraction and the formation of new ligament connections, thereby increasing the effective load-bearing capacity of the network [52]. A similar stiffening behavior is observed in our HNPG samples, as shown in Figure 4.3, consistent with previous findings by Shi et al. [22].

Interestingly, despite significant plastic deformation and a clear increase in actual solid volume fraction, the elastic Poisson's ratio ν_E remains nearly unchanged throughout compression. This invariance stands in contrast to the scaling behavior between ν_E and φ_{net} established for undeformed structures (see Figure 4.11). While the trend superficially resembles the prediction of the Gibson–Ashby model [145], the measured ν_E in deformed HNPG is much lower than the model's nominal value of 0.33. These observations suggest that scale relationships derived for the original structure may not be directly applicable to deformed structures, where the evolution of the microstructure, particularly the yielding and densification of ligaments, significantly alters the mechanical response.

In contrast to the relatively stable ν_E observed in our HNPG samples, previous studies on monolithic NPG have reported opposing trends in the evolution of elastic Poisson's ratio under compression. Specifically, Bürckert et al. [150] observed a monotonic decrease in ν_E with increasing strain, while Lührs et al. [27] reported an increasing trend. The absence of a pronounced Poisson's ratio to strain dependence in HNPG may be attributed to its significantly lower solid volume fraction φ_{net} compared to conventional NPG.

Typically, φ_{net} in NPG ranges from approximately 0.25 to 0.40 during compression up to 30% strain, whereas in our HNPG samples, it varies only from 0.12 to 0.25, exhibiting minimal overlap with the NPG data regime. Previous work by Shi et al. [22] has shown that deformation in HNPG induces hierarchical, level-specific microstructural changes. Specifically, the upper level network undergoes more pronounced plastic deformation and densification compared to the lower level ligaments. This hierarchical heterogeneity may explain why ν_E remains relatively invariant in HNPG, despite ongoing structural evolution. The decline of ν_E with strain observed by Bürckert et al. was interpreted as a consequence of progressive ligament yielding, which reduces the number of load-bearing elements contributing to lateral elastic response. This mechanism likely applies to the lower level structure in HNPG. Conversely, the increase in ν_E at large compressive strains reported by Lührs et al. reflects substantial densification, reorientation and topological reconfiguration of the ligament network, which in HNPG predominantly occurs at the upper hierarchical level. Given these hierarchical differences, direct extrapolation of mechanical trends from unimodal NPG to HNPG is not straightforward. The non-uniform microstructural evolution across different hierarchical levels fundamentally alters the mechanical response and thus conclusions derived from monolithic microstructures must be revisited in the context of hierarchical porous systems.

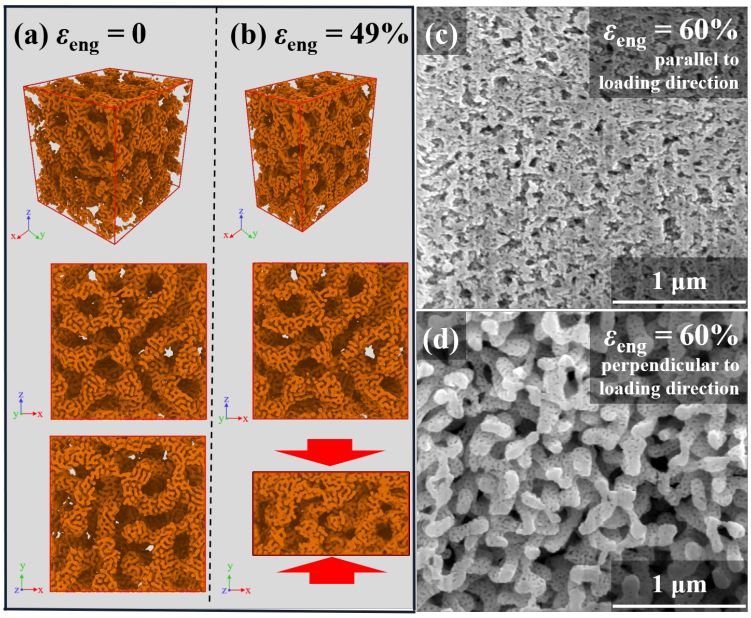


Figure 4.13: Microstructure evolution during compression. Molecular dynamics (MD) simulated microstructure of virtual HNPG at a compressive strain of (a) ε_{eng}=0 and (b) ε_{eng} =49% [22], Top: a three-dimensional overview, middle: cross section perpendicular to the compression direction, bottom cross-section parallel to the compression direction. The loading direction is indicated by red arrows. Reprinted with permission from Ref [22]. SEM images of the cross sections (c) parallel and (d) perpendicular to the compression direction of HNPG samples at ε_{eng}=60%.

In addition, we hypothesize that the ν_E is predominantly governed by the microstructural evolution in the cross section perpendicular to the loading direction. This hypothesis is supported by both experimental observations and molecular dynamics (MD) simulations. As shown in Figure 4.13a and b, MD simulations of virtual HNPG [22]

reveal that, under compressive strain up to 49%, the cross section perpendicular to the loading direction undergoes minimal structural change, whereas the cross section parallel to the loading axis exhibits substantial densification, particularly at the upper hierarchical level.

This anisotropic evolution is corroborated by SEM images of actual HNPG samples compressed to $\varepsilon_{\text{eng}} = 60\%$, shown in Fig. 4.13c and d. The cross section perpendicular to the loading direction retains a relatively open, undeformed ligament network, while significant densification and structural compaction are evident in the parallel cross section. These observations support the notion that lateral expansion and therefore Poisson's effect is primarily dictated by the structure perpendicular to the loading direction, which remains relatively stable during deformation. Consequently, this morphological anisotropy helps to explain the near-constancy of ν_{E} despite ongoing densification in other parts of the microstructure.

4.3 Chapter Summary

In this chapter, we systematically investigated the scaling behaviors of both ν_{E} and ν_{P} in HNPG. By leveraging hierarchical control over ligament sizes and solid volume fraction, we demonstrated that HNPG exhibits nearly invariant Poisson's ratios across a wide structural range, a behavior distinct from uni-modal NPG. We introduced a generalized scaling law that captures the dependence of ν_{E} on network porosity and hierarchy and we showed that the scaling remains valid across different deformation regimes.

These findings establish a clear link between hierarchical microstructure and Poisson's ratio. In particular, they demonstrate that Poisson's ratio can be tuned through structural design by introducing structural hierarchy. However, such structural tuning is inherently fixed once the material is fabricated and therefore not reversible during operation. In the next chapter, we shift focus from purely structural control to chemo-mechanical coupling in nanoporous Pd-based systems, where Poisson's ratio can be modulated reversibly through electrochemically controlled hydrogen sorption.

Chapter 5

Hydrogen-induced Tunable Poisson's Ratio in np Pd

Building on the preceding discussion of structural control, this chapter examines an alternative route for tuning Poisson's ratio based on chemo-mechanical coupling. In contrast to the structural approach presented in Chapter 2, where the mechanical response is fixed once the structure is fabricated, the use of a mobile interstitial solute enables reversible modulation of elastic properties under electrochemical control.

Here, np Pd-H and np PdAu-H systems are employed as model materials, in which the hydrogen chemical potential can be adjusted via the applied electrode potential. This provides access to conditions approaching the open-system limit, allowing the elastic response to be probed under near-constant chemical potential. The central objective of this chapter is to quantify the evolution of the elastic Poisson's ratio with hydrogen concentration and to assess its consistency with the open-system elasticity framework introduced previously.

Np Pd and np PdAu were fabricated by electrochemical dealloying and characterized in terms of ligament size and phase constitution. Hydrogen sorption was controlled potentiostatically and the elastic response was evaluated by cyclic compression combined with full-field DIC. ν_{E} is extracted from unloading segments under near-equilibrium conditions (interpreted as ν_{E}^{μ} when discussing the within open-system condition). The Results section first establishes the microstructural and crystallographic baseline of both materials, then presents the evolution of ν_{E}^{μ} with hydrogen concentration x_{H} and finally compares the experimental trends with open-system predictions using hydrogen-dependent elastic input from the literature. The subsequent Discussion connects the observed behaviour to phase stability (miscibility gap suppression by Au), thermodynamic susceptibility and solute-strain coupling and clarifies the conditions under which open-system elasticity is expected to hold in nanoporous Pd-based hydrides.

5.1 Results

5.1.1 Microstructure and Phase Composition

Figure 5.1 presents the microstructural characterization of np Pd and np PdAu. Figure 5.1a shows a representative SEM image of np Pd, revealing the characteristic bicontinuous hierarchical nanoporous structure, with average ligament sizes L of approximately 40 nm for the upper hierarchical levels with a finer level structure embedded in the upper level. In contrast, the nanoporous morphology of np PdAu is not fully resolved in SEM due to its substantially finer feature size (Figure 5.1b). Nevertheless, it is evident that the ligament size in np PdAu is significantly smaller than in np Pd. To quantify the precise ligament sizes in np PdAu and ensure a consistent comparison, TEM was performed on both materials.

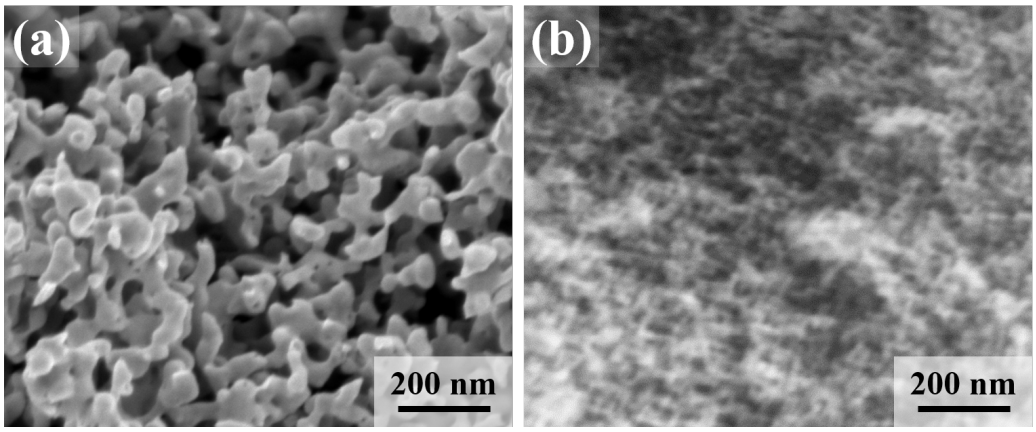


Figure 5.1: SEM pictures show the microstructure morphology of np Pd and np PdAu samples. (a) np Pd; (b) np PdAu.

The elemental compositions of the dealloyed samples were determined by energy-dispersive X-ray spectroscopy (EDX), as described in Section 3.3.1. The corresponding quantitative results are summarized in Table 5.1. For np Pd, the EDX measurements reveal a predominantly Pd-rich composition with approximately 5 at.% residual Cu. For np PdAu, the measured composition is approximately 77 at.% Pd, 16 at.% Au, and 7 at.% Cu. These results confirm that a small amount of Cu remains in both nanoporous materials after electrochemical dealloying. However, since SEM-EDX provides an average composition over the analyzed volume, these measurements do not directly establish the spatial distribution of residual Cu within individual ligaments.

Table 5.1: Approximate elemental compositions of np Pd and np PdAu after dealloying, determined by SEM-EDX measurements on fracture surfaces. Values are reported in atomic percent (at.%). The Pd concentration of np Pd is estimated by difference from the reported residual Cu content.

Sample	Pd (at.%)	Au (at.%)	Cu (at.%)
np Pd	~95	–	~5
np PdAu	~77	~16	~7

Figure 5.2 presents the microstructural characterization of np Pd and np PdAu. High-angle annular dark-field scanning transmission electron microscopy (HAADF-STEM) images (Figure 5.2a and b) reveal the characteristic bicontinuous ligament-pore network formed by electrochemical dealloying in both materials. A pronounced difference is observed in ligament size L. For np Pd (Figure 5.2a), consistent with the SEM observations, the ligament sizes are 40 nm with an embedded pore-ligament structure. For np PdAu (Figure 5.2b), the network is substantially finer, with an average ligament size of $L \approx 5$ nm. The ligament size analysis was performed on HAADF-STEM images using the same procedure for both samples and is representative of multiple image regions.

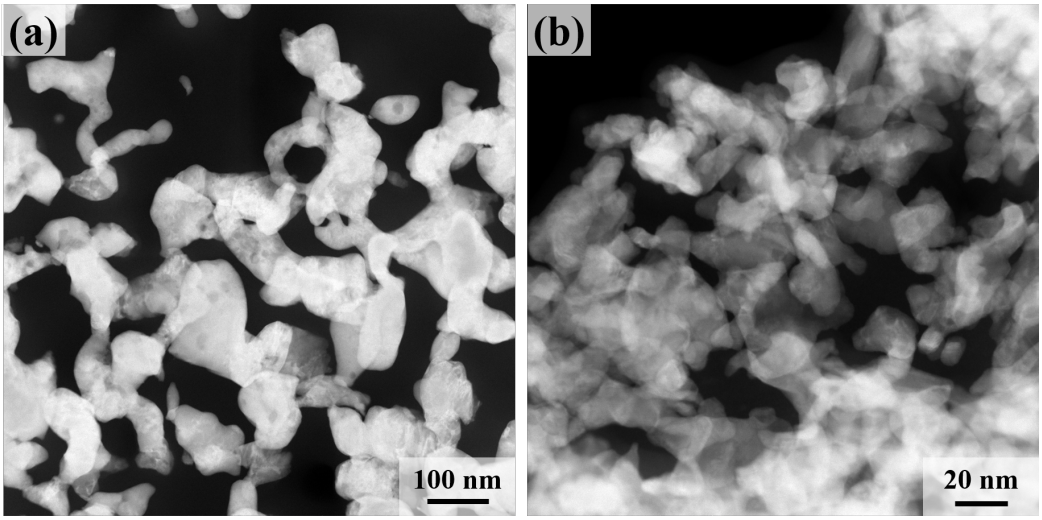


Figure 5.2: High-angle annular dark-field scanning transmission electron microscopy (HAADF-STEM) images of np Pd and np PdAu samples, revealing the nanoscale bicontinuous ligament structure. (a) np Pd; (b) np PdAu. The high atomic number contrast in HAADF mode enhances the visualization of ligament connectivity and size variations between the two samples.

Figure 5.3a shows XRD patterns of the $Pd_{15}Cu_{85}$ and $Pd_{12.5}Au_{2.5}Cu_{85}$ master alloys used as precursors for np Pd and np PdAu. In both cases, the diffraction peaks can be indexed to a single fcc solid-solution phase, with reflections corresponding to the (111), (200), (220), (311) and (222) planes. No secondary phases such as ordered Pd–Cu intermetallics are detected, which is consistent with the full miscibility of Pd–Cu and Pd–Au binary alloys at elevated temperatures [176–178], suggesting that a single-phase solid solution can also be expected in the corresponding Pd–Au–Cu ternary system. The presence of a single fcc phase in both master alloys confirms that homogenization annealing was effective and ensures uniform chemical environments during dealloying. This single-phase condition is crucial, as multiphase precursor alloys can give rise to heterogeneous dissolution pathways, uneven porosity development and phase-selective corrosion, all of which can compromise ligament continuity and mechanical integrity [42, 46].

Figure 5.3b shows the XRD patterns of np Pd and np PdAu. All diffraction peaks can be indexed to a face-centered cubic (fcc) structure, with reflections corresponding to the (111), (200), (220), (311) and (222) planes, indicating that both materials retain a single-phase solid solution after dealloying. The diffraction peaks of np Pd are

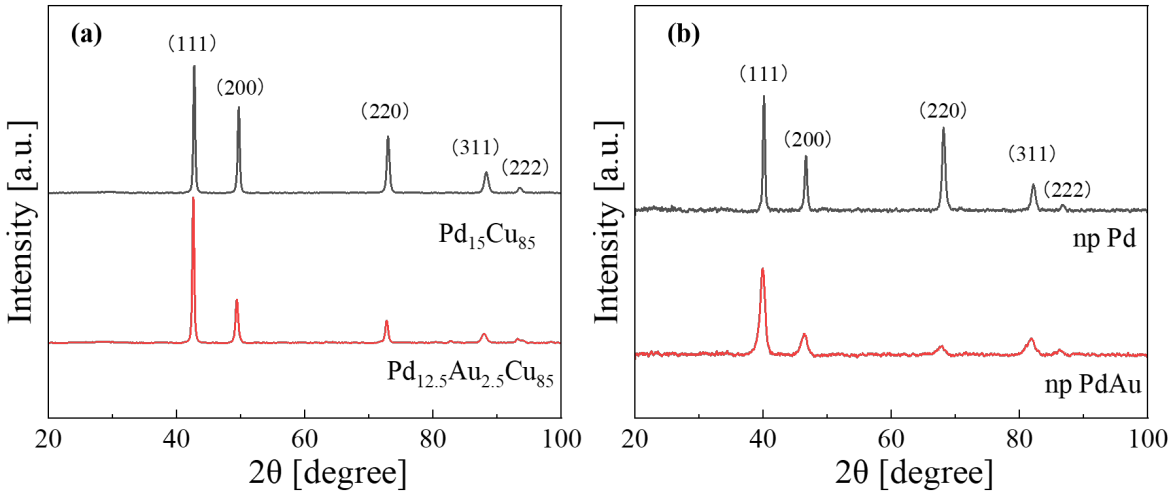


Figure 5.3: X-ray diffraction patterns of the precursor master alloys and the corresponding nanoporous samples. (a) XRD patterns of $Pd_{15}Cu_{85}$ and $Pd_{12.5}Au_{2.5}Cu_{85}$ (at.%) master alloy; (b) XRD patterns of np Pd and np PdAu.

broadened, a characteristic feature commonly observed in nanoporous metals. In such systems, peak broadening does not primarily originate from grain refinement, but from the presence of nanoscale porosity, which limits the coherent scattering length even when the ligaments themselves remain crystalline, as demonstrated for nanoporous gold by Graf *et al.* [179]. Compared to np Pd, np PdAu exhibits a further increase in peak broadening together with a slight shift of the (111) reflection toward lower diffraction angles. The additional broadening is consistent with the finer ligament size observed in np PdAu.

The peak shift reflects lattice expansion due to Au incorporation into the Pd lattice and follows Vegard's law for Pd-Au solid solutions.

Using Bragg's law:

$$2d \sin\theta = \lambda \tag{5.1}$$

where $\lambda = 1.5406$ Å (Cu Kα radiation), θ is the Bragg angle and d is the interplanar spacing.

For an fcc crystal:

$$d_{hkl} = \frac{a}{\sqrt{h^2 + k^2 + l^2}} \tag{5.2}$$

and for the (111) reflection:

$$a = \sqrt{3}\, d_{111} \tag{5.3}$$

The (111) peak of np Pd appears at $2\theta = 40.2°$, giving:

$$\theta_{\mathrm{Pd}} = 20.1°$$

Then:

$$d_{\mathrm{Pd}} = \frac{\lambda}{2\sin\theta_{\mathrm{Pd}}} = \frac{1.5406}{2\sin 20.1°} = 2.237 \text{ Å} \tag{5.4}$$

$$a_{\mathrm{Pd}} = \sqrt{3}\, d_{\mathrm{Pd}} = 1.732 \times 2.237 = 3.877 \text{ Å} \tag{5.5}$$

This value is in good agreement with the known bulk Pd lattice constant ($a_{\mathrm{Pd}}^{\mathrm{bulk}} = 3.890\,\text{Å}$).

Consequently, the (111) peak of np PdAu appears at $2\theta = 39.8°$, yielding

$$\theta_{\mathrm{PdAu}} = 19.9°$$

Thus:

$$d_{\mathrm{PdAu}} = \frac{1.5406}{2\sin 19.9°} = 2.268\ \text{Å} \tag{5.6}$$

$$a_{\mathrm{PdAu}} = \sqrt{3}\, d_{\mathrm{PdAu}} = 1.732 \times 2.268 = 3.926\ \text{Å} \tag{5.7}$$

Vegard's law predicts a linear variation of lattice parameter with Au concentration x in $\mathrm{Pd}_{1-x}\mathrm{Au}_x$(neglecting the influence of residual Cu):

$$a(x) = (1-x)\, a_{\mathrm{Pd}} + x\, a_{\mathrm{Au}} \tag{5.8}$$

Using $a_{\mathrm{Pd}} = 3.890\,\text{Å}$ and $a_{\mathrm{Au}} = 4.078\,\text{Å}$and the measured composition of np $\mathrm{Pd}_{1-x}\mathrm{Au}_x$ ($x = 0.167$):

$$a_{\mathrm{Vegard}} = (1 - 0.167) \times 3.890 + 0.167 \times 4.078 \tag{5.9}$$

$$= 3.240 + 0.681 = 3.921\ \text{Å} \tag{5.10}$$

The measured lattice constant:

$$a_{\mathrm{PdAu}}^{\mathrm{exp}} = 3.926\ \text{Å}$$

is consistent with the Vegard prediction:

$$a_{\mathrm{Vegard}} = 3.921\ \text{Å}$$

Take residual Cu into account, Vegard's law for the chemical composition $\mathrm{Pd}_{77}\mathrm{Au}_{16}\mathrm{Cu}_7$ predicts

$$a_{\mathrm{Pd_{77}Au_{16}Cu_7}} \approx 3.901\ \text{Å}$$

using the lattice parameters of pure Pd ($a_{\mathrm{Pd}} = 3.890\,\text{Å}$), Au ($a_{\mathrm{Au}} = 4.078\,\text{Å}$) and Cu ($a_{\mathrm{Cu}} = 3.615\,\text{Å}$). From the position of the (111) peak, a lattice parameter of $a \approx 3.926\,\text{Å}$ is obtained for np PdAu, in good agreement with the expected value for a $\mathrm{Pd}_5\mathrm{Au}_1$ composition based on interpolation between pure Pd and Au lattice constants [176]. Including Cu in a simple linear mixture gives a somewhat lower estimate (3.901 Å), suggesting that Cu is not uniformly incorporated in the Pd fcc lattice but maybe in the form of cluster inside the ligaments.

5.1.2 Poisson's ratio variation with hydrogen concentration

Figure 5.4a shows cyclic voltammograms of np Pd and np PdAu recorded in 1 mol/L H_2SO_4 at a scan rate of 1 mV /s and room temperature. Both materials exhibit the characteristic sequence of hydrogen electrochemical processes: hydrogen under potential deposition (UPD) on the internal surfaces, followed by hydrogen absorption into the bulk (presented as α and α' phases) at more negative potentials and desorption on the reverse scan. The onset of bulk absorption is indicated by a cathodic current rise near

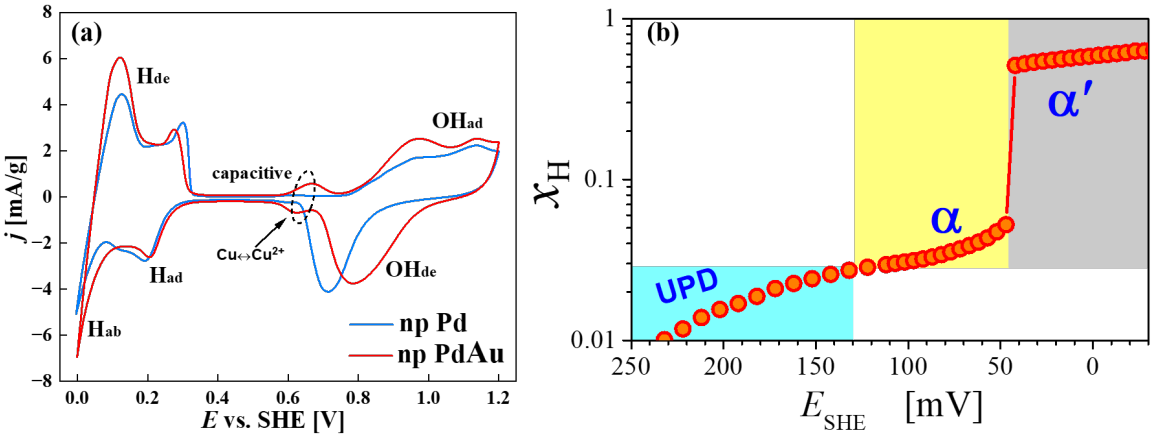


Figure 5.4: Cyclic voltammograms (CV) and H sorption (a) CV patterns of np Pd (blue) and np PdAu (red) recorded in 1 mol/L H_2SO_4 at a scan rate of 1 mV/s. (b) Net (including surface adsorption plus bulk absorption) hydrogen concentration (x_H) vs. electrode potential (vs. SHE) for np Pd. Regimes of hydrogen under potential deposition (UPD) on the pore surfaces and of bulk hydrogen sorption in the dilute α and concentrated α' phase are marked. Reprinted with permission from Ref [25]

100 mV (vs. SHE), while the transition towards the hydrogen-concentrationed α' phase is observed below approximately 50 mV.

The CV of np Pd is smooth and contentious, indicating consistent and reversible surface adsorption and bulk absorption processes. In np PdAu, additional minor current features appear between the capacity region and OH sorption. These are attributed to residual Cu, consistent with the slightly higher Cu content determined by EDX. The OH desorption peak on the reverse scan is shifted towards slightly more positive potentials in np PdAu compared to np Pd. This shift is consistent with a change in the electronic structure upon alloying Pd with Au, which typically lowers the d-band center and weakens the binding of oxygenated species [180, 181]. Similar cathodic shifts of OH-related features have been reported for Au-modified Pd surfaces and thin films [182], supporting the conclusion that Au incorporation alters the surface chemistry in addition of residual Cu.

Figure 5.4b (reproduced from Ref. [25]) shows the net hydrogen concentration x_H (including surface adsorption and bulk absorption) in nanoporous Pd as a function of electrode potential. Three regimes can be distinguished: (i) a surface-dominated hydrogen UPD regime for $E \gtrsim 100$ mV (vs. SHE); (ii) bulk absorption into the dilute α phase for approximately 50–100 mV; and (iii) a steep rise in x_H at $E \lesssim 50$ mV associated with the onset of the α' phase. The sharp increase in x_H in regime (iii) is accompanied by large volumetric expansion and a substantial risk of mechanical instability.

Figure 5.5 shows the relationship between electrochemical potential and x_H for the two nanoporous systems. Under potentiostatic conditions, the applied potential fixes the hydrogen chemical potential μ_H, while the equilibrium x_H adjusts according to the thermodynamic response of the material. Accordingly, x_H is not an independent control parameter but is assigned based on this independently measured potential–composition relation. In practice, x_H was determined from electrochemical charge measurements associated with hydrogen extraction. For each target potential (e.g. 100, 80, 60 mV

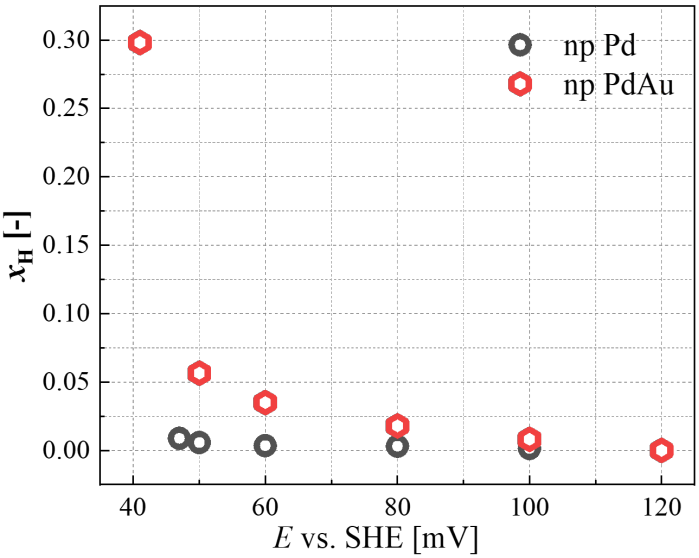


Figure 5.5: Relation between applied electrochemical potential and equilibrium x_H for np Pd and np PdAu under potentiostatic conditions. x_H were determined independently from electrochemical sorption measurements performed under identical conditions as the mechanical tests.

vs. SHE), the sample was first equilibrated and then stepped back to 380 mV, where hydrogen is fully desorbed. The charge released during this potential step corresponds to the total hydrogen content stored in the sample. To isolate the contribution from bulk hydrogen absorption, the charge associated with hydrogen underpotential deposition (UPD) on the surface was subtracted. This reference charge was obtained from a corresponding potential step between 120 mV and 380 mV, where hydrogen is predominantly present in the underpotential deposition (UPD) regime. Although the transition from surface adsorption to bulk absorption is gradual, this potential range provides a reasonable approximation for separating surface and bulk contributions, following the approach of Shi *et al.* [25]. As shown, decreasing the applied potential E leads to an increase in the equilibrium x_H for both np Pd and np PdAu. For np Pd, x_H increases rapidly at relatively high E and saturates at low values, reflecting the limited hydrogen solubility in the dilute α phase. In contrast, np PdAu exhibits a continuous increase in x_H over a much wider E range, reaching substantially higher x_H under otherwise identical electrochemical conditions.

Mechanical tests were performed on both np Pd and np PdAu under potentiostatic control to examine the dependence of the elastic Poisson's ratio ν_E. For each applied potential, the system was allowed to equilibrate prior to loading, and the corresponding hydrogen concentration x_H was obtained from independent electrochemical absorption measurements.

Figure 5.6a and b present representative engineering stress–strain (σ–ε_{eng}) curves for np Pd and np PdAu samples subjected to stepwise potentiostatic control. Each curve corresponds to a cyclic loading–unloading test with a maximum engineering strain of 3%. The loading segments show the overall mechanical response of the nanoporous network, while the unloading segments are nearly linear and reflect predominantly elastic recovery, indicating that plastic deformation is limited under the chosen testing

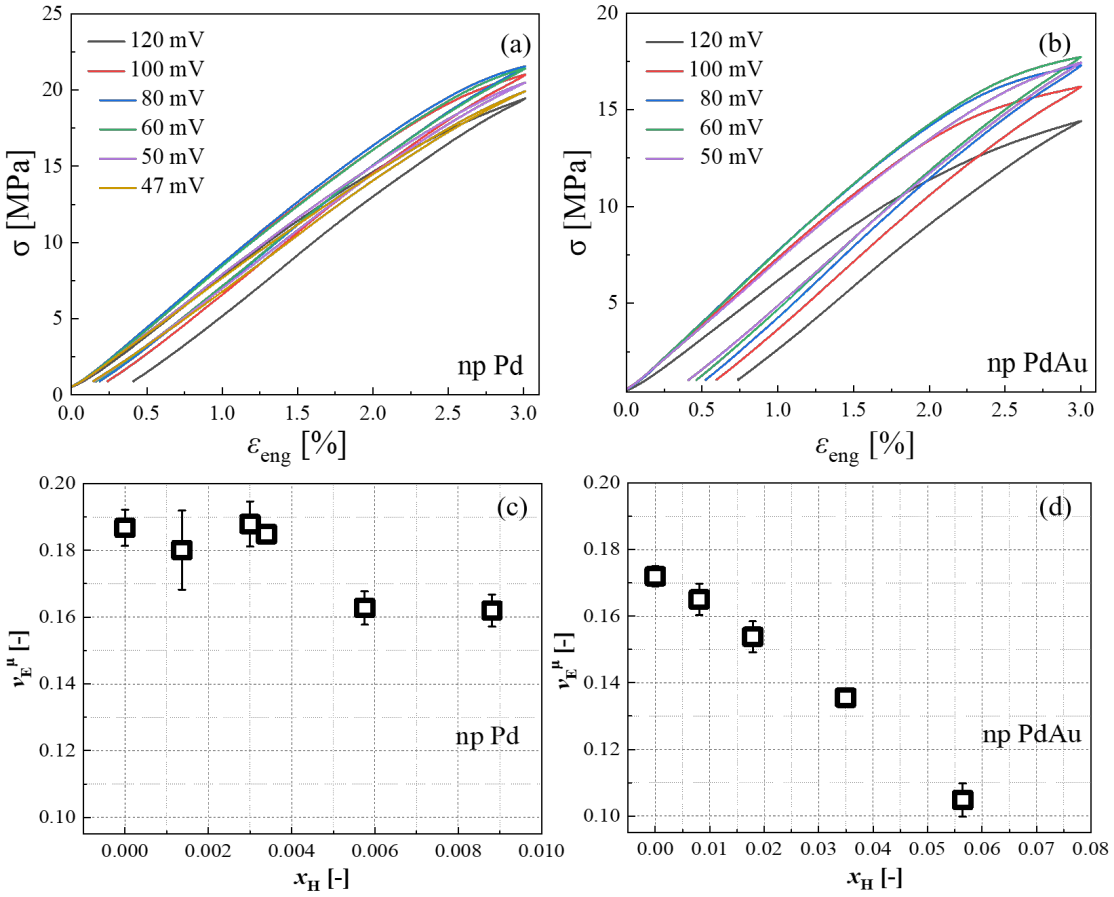


Figure 5.6: Mechanical test results and elastic Poisson's ratio (ν_E) vs. hydrogen concentration (x_H) for representative np Pd and PdAu samples with the corresponding engineering strain for the 3 % loading-unloading test. (a) Engineering stress-strain (σ - ε_{eng}) curve for the np Pd sample; (b) σ - ε_{eng} curve for the np PdAu sample; (c) ν_E as a function of x_H for the np Pd sample and (d) ν_E as a function of x_H for the np PdAu sample.

conditions. The measurements were performed sequentially at decreasing potentials. Starting from 120 mV (vs. SHE), the sample was equilibrated at each target potential and mechanically tested. After each loading–unloading cycle, the potential was stepped back to 380 mV to fully desorb hydrogen before proceeding to the next, lower potential. This procedure ensures that each σ–ε_{eng} curve corresponds to a well-defined hydrogen state. The charge released during the potential step back to 380 mV was used to determine the hydrogen content, as described above, with subtraction of the reference charge associated with hydrogen UPD.

For np Pd, the applied potentials ranged from 120 mV down to 47 mV (vs. SHE), i.e. close to the $\alpha \rightarrow \alpha'$ boundary; therefore measurements were restricted to $x_H < 0.01$ to avoid hydride nucleation under load. The ν_E was extracted from the unloading segments using full-field strain analysis based on DIC, as shown in Figure 5.6c. ν_E exhibits a clear dependence on x_H. ν_E decreased from around 0.19 to 0.16 in the range of x_H from 0 to around 0.01. In np PdAu (Figure 5.6d), ν_E decreases sharply at low x_H and reaches a minimum at $x_H \approx 0.06$, from 0.17 to nearly 0.1, which is a significant decrease.

To emphasize the experimental observation, we first report the elastic Poisson's ratio

extracted from unloading segments as ν_E. Under potentiostatic control with sufficient equilibration, the electrode potential fixes μ_H and hydrogen redistribution can follow the applied stress during quasi-static loading (see Section 5.2.3). In this near-equilibrium limit, the unloading-based ν_E provides an experimental estimate of the open-system response and we therefore compare it with the open-system prediction by treating $\nu_E \approx \nu_E^\mu$. To interpret these observations within the framework of open-system elasticity, a comparison between the experimental data and the theoretical model is presented in the following Discussion section.

5.2 Discussion

5.2.1 Comparison with open-system elasticity model

To examine whether the observed evolution of Poisson's ratio can be interpreted within the Larché–Cahn open-system elasticity framework, the experimental data are compared with theoretical predictions in Fig. 5.7.

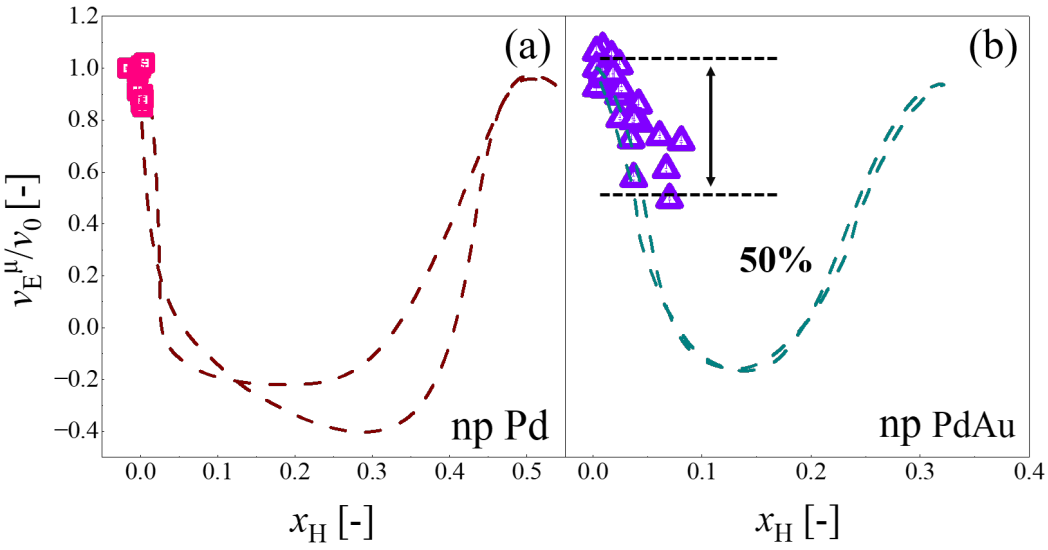


Figure 5.7: Normalized elastic Poisson's ratio under potentiostatic (fixed-μ_H) conditions, shown as ν_E^μ/ν_0 versus x_H. (a) np Pd; (b) np PdAu. Symbols: experimental unloading-based ν_E obtained from in-situ DIC (same data as in Fig. 5.6). Lines: open-system prediction calculated from Eq. 2.30 using hydrogen-dependent Young's modulus from Ref. [25]. For the purpose of comparison, the measured ν_E is treated as an estimate of ν_E^μ in the near-equilibrium.

Figure 5.7a and b show the normalized open-system elastic Poisson's ratio ν_E^μ/ν_0 as a function of x_H for np Pd and np PdAu, respectively. While these plots illustrate the overall evolution of ν_E^μ with x_H, a quantitative comparison between experiment and open-system elasticity theory is only meaningful in the dilute regime. In the Larché–Cahn framework, the open-system elastic response depends on the closed-system elastic constants Y^x and ν^x in closed system. Because Y^x and ν^x are not available experimentally over the full x_H range, they are approximated by the hydrogen-free values $Y_{Pd/PdAu}$ and $\nu_{Pd/PdAu}$, following the approach adopted by Shi *et al.* [25].

This approximation is only valid at low x_H, where changes in the closed-system elastic constants remain small.

The theoretical curves shown in Figures 5.7 and 5.8 were generated from the open-system elasticity relation given in Eq. (2.30), using the hydrogen-dependent Young's modulus reported in Ref. [25]. In the dilute hydrogen regime, the closed-system elastic constants were approximated by their hydrogen-free values, $Y^x \approx Y_0$ and $\nu^x \approx \nu_0$. Consequently, the normalized open-system Poisson's ratio can be expressed as

$$\frac{\nu^\mu(x_H)}{\nu_0} = \frac{1}{\nu_0}\left[(1+\nu_0)\frac{Y^\mu(x_H)}{Y_0} - 1\right] \tag{5.11}$$

Figure 5.8 presents an enlarged view of the dilute-hydrogen region of the same theoretical predictions shown in Figure 5.7, restricted to $x_H < 0.01$ for np Pd and $x_H < 0.04$ for np PdAu. The theoretical curves were calculated directly from the above relation, without manual adjustment of their shapes.

Accordingly, Figure 5.8 compares experimental data and theoretical predictions for ν_E^μ/ν_0 in the dilute regime for both np Pd ($x_H < 0.01$) and np PdAu ($x_H < 0.04$). The symbols represent experimental values obtained from in-situ DIC measurements during elastic unloading, while the lines correspond to theoretical predictions calculated using Equation 2.30. Within this dilute x_H range, the model captures the experimentally observed decrease of ν_E^μ/ν_0 with increasing x_H in both systems, showing good agreement with the open-system elasticity prediction in the dilute regime.

Notably, the range of accessible x_H differs greatly between the two systems, as shown in Figure 5.7. In np Pd, hydrogen absorption in the α phase saturates below $x_H \approx 0.01$, whereas in np PdAu, $x_H \approx 0.3$ can be reached under potentiostatic control. This difference originates from the modification of hydrogen thermodynamics by Au alloying; the underlying electronic and thermodynamic mechanisms are discussed in Section 5.2.2. In contrast, pure Pd exhibits a flat μ_H–x_H region associated with the α–α' miscibility gap.

As shown in Figure 5.7, the experimental data points fall close to the theoretical predictions within the hydrogen diluted range. In addition, reversible recovery of ν_E during hydrogen charging–discharging was observed, indicating that deformation during testing is dominated by reversible, composition-dependent elastic response rather than plasticity or irreversible damage. This reversibility and tunability of ν_E^μ with x_H are consistent with the interpretation based on open-system elasticity. Figure 5.8 further illustrates that the Larché–Cahn open-system elasticity model ceases to be applicable as the system approaches the conditions for phase transformation (for np Pd at $x_H \approx 0.01$ and for np PdAu at $x_H \approx 0.04$).

In summary, the present results extend the experimental verification of the Larché–Cahn open-system elasticity framework by explicitly demonstrating the tunability of the elastic Poisson's ratio under fixed chemical potential conditions. Together with previous validation based on Young's modulus [25], this work provides a more complete experimental picture of open-system elastic behavior in metal–hydrogen systems. Moreover, the pronounced composition-dependent variation of ν_E^μ observed here is not unique to Pd-based materials. Phase-field and finite-element studies have predicted analogous concentration-dependent elastic responses in a variety of interstitial systems, including Li–Si electrodes and related energy materials [121, 122]. In these systems, the

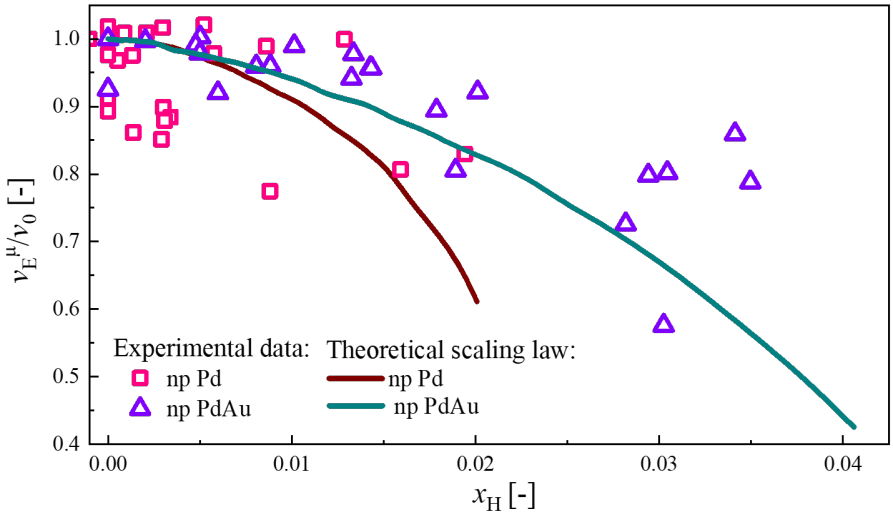


Figure 5.8: Comparison of the normalized open-system elastic Poisson's ratio, ν_E^μ/ν_0, with experimental measurements in the dilute hydrogen regime for np Pd (pink squares) and np PdAu (purple triangles). The theoretical curves were calculated directly from Eq. 5.11, using the hydrogen-dependent Young's modulus reported in Ref. [25] and approximating the closed-system elastic constants by their hydrogen-free values. The curves represent enlarged low-concentration portions of the theoretical predictions shown in Figure 5.7, with $x_H < 0.01$ for np Pd and $x_H < 0.04$ for np PdAu.

elastic properties, such as Young's modulus and, in some cases, Poisson's ratio, evolve with solute concentration as a result of chemo-mechanical coupling. These cross-system consistencies suggest that open-system elasticity provides a general framework for describing solute–strain coupling in metals with mobile interstitials.

5.2.2 Hydrogen-Mechanics Coupling in np Pd vs. np PdAu

The experimental results establish that electrochemical hydrogen sorption provides an effective means of tuning the elastic response of nanoporous Pd-based metals. In both np Pd and np PdAu, hydrogen sorption leads to a reduction of the open-system elastic Poisson's ratio ν_E^μ and the open-system Young's modulus Y^μ, while the extent and reversibility of this tunability depend strongly on alloy composition and phase stability. The contrast between np Pd and np PdAu is particularly instructive.

In np Pd, hydrogen absorption is limited by the well-known α–α' miscibility gap of the Pd–H system at room temperature. As the potential is lowered toward the phase transition, the chemical potential–composition isotherm steepens and large volumetric strains develop. Under the additional constraint of an externally applied compressive load, these strains lead to stress concentrations, hydride nucleation and ultimately ligament cracking. This restricts the accessible hydrogen concentration to the dilute regime and prevents a full exploration of the ν_E^μ behaviour.

By contrast, Au alloying substantially modifies the hydrogen thermodynamics. Even at moderate Au contents, the miscibility gap is suppressed and the single-phase α solid solution is stabilized over a wider composition range [25, 183]. The resulting

flattening of the chemical potential–composition isotherm reduces the driving force for phase transition and lowers the elastic energy cost of hydrogen insertion. As a result, np PdAu can be hydrogenated to much higher x_{H} without triggering phase coexistence or irreversible damage, allowing the full evolution of ν_{E}^{μ} and Y^{μ} to be observed.

The mechanism by which Au alloying improves sample performance has three closely related aspects. First, Au affects the electronic structure of the Pd matrix in a way that is directly relevant to hydrogen thermodynamics. On the electronic level, Au incorporation dilutes the Pd *d*-band and shifts its center to lower energy, which weakens the Pd–H interaction and reduces the enthalpy gain associated with hydrogen occupying octahedral interstitial sites [180, 181, 183]. In the language of regular-solution thermodynamics, this corresponds to a reduction of the effective interaction parameter that drives ordering and phase transition. As a consequence, the μ–x_{H} isotherm in PdAu becomes less S-shaped and more convex, the critical temperature T_{c} is lowered (Figure 2.5a) and the α–α' miscibility gap is strongly narrowed or even eliminated at room temperature [25, 183]. Physically, this means that hydrogen atoms in PdAu experience a smoother energetic landscape: adding additional H no longer produces a strong cooperative tendency to form a high-x_{H} hydride phase but instead leads to a more gradual, nearly ideal increase in concentration.

Second, there is a geometric and statistical effect. Au does not accommodate hydrogen as readily as Pd, so each Au atom effectively acts as a blocked site in the Pd lattice. This dilution of available interstitial environments further suppresses the cooperative Pd–H interactions that favour phase transition and thereby extends the single-phase α region to higher x_{H} at a given temperature. From the perspective of the Larché–Cahn framework, this corresponds to a smoother, bounded susceptibility $\chi = \frac{1}{\rho_0}(\partial x/\partial \mu)_T$ over a wide composition range, avoiding the divergence of χ that occurs near the spinodal in pure Pd.

Third, there is a kinetic effect. Au has been shown experimentally to accelerate hydrogen surface exchange and absorption in PdAu alloys [184], which increases the rate at which hydrogen can equilibrate under potentiostatic control and during mechanical loading. Although nanoporosity itself tends to reduce the absolute stiffness and np PdAu has smaller ligaments than np Pd, the dominant factor for the observed differences in tunability is not the geometry but the alloy-induced changes in the μ–x_{H} landscape and in hydrogen transport kinetics. These combined electronic, thermodynamic and kinetic effects are essential for stabilizing open-system elasticity over an extended composition window and for enabling the large, reversible changes in ν_{E} observed in np PdAu.

The experimental data in Figures 5.7 and 5.8 are consistent with the open-system interpretation within the single-phase regime, where the assumptions underlying Eq. (2.30) (rapid equilibration and an effective isotropic response) are best satisfied. In both np Pd and np PdAu, $\nu_{\mathrm{E}}^{\mu}/\nu_0$ initially decreases with increasing x_{H}, consistent with an increased open-system compliance contribution in the concentration range where $\chi(x_{\mathrm{H}})$ is large. In np PdAu, a pronounced minimum is observed around $x_{\mathrm{H}} \approx 0.05$, followed by a partial recovery at higher x_{H}. Within the present framework, this trend is naturally explained by a reduction of the incremental compositional response away from the most susceptible concentration range (i.e. an effective decrease of χ), while additional concentration-dependent changes of the intrinsic (closed-system) stiffness may also contribute through $Y^{x}(x_{\mathrm{H}})$ and $\nu^{x}(x_{\mathrm{H}})$.

In np Pd, agreement between the open-system picture and experiment is good in the dilute regime but deteriorates as the miscibility gap is approached. This behavior is expected: close to phase coexistence, the single-phase assumption breaks down and eigenstrains associated with two-phase mixtures can introduce additional internal stresses and irreversibility, making deviations from the single-phase open-system relations unavoidable.

For better discussion of the regime-wise interpretation, the observed evolution of ν_{E}^{μ} can be separated into three regimes, described here in terms of hydrogen concentration and the associated chemo-mechanical response.

(i) Hydrogen-diluted regime: At low hydrogen concentration, the experiments probe a regime where stress-assisted solute redistribution contributes appreciably to the apparent compliance. Within the open-system framework, the observed decrease in ν_{E}^{μ} is consistent with a significant open-system contribution, associated with a pronounced compositional response to the applied chemical potential.

(ii) Intermediate concentration regime: With increasing x_{H}, ν_{E}^{μ} reaches a minimum and then partially recovers. This behavior can be interpreted as a reduction in the incremental response of x_{H} to μ, i.e. an effective decrease of the open-system contribution associated with χ. In addition, concentration-dependent changes in the intrinsic closed-system elastic constants may also become relevant in this regime.

(iii) Hydrogen-concentrated regime: At higher hydrogen concentration, approaching the limit of the stable single-phase region, the assumptions underlying Eq. (2.30) become progressively less reliable. The onset of phase separation, associated eigenstrains, and internal stress heterogeneity can lead to deviations from ideal open-system behavior, and may promote irreversible microstructural changes.

Finally, it is instructive to place the observed tunability of ν_{E}^{μ} in a broader context. Similar composition-dependent elastic effects have also been predicted in other interstitial-solute systems. For example, first-principles calculations for Fe-based alloys indicate that interstitial hydrogen can reduce both Young's modulus and Poisson's ratio in a concentration- and orientation-dependent manner [185]. These results support the broader view that composition-dependent elastic constants, including Poisson's ratio, can emerge in solids with mobile interstitial solutes and significant eigenstrain. Whether a similarly strong and reversible tunability can be achieved depends on diffusion kinetics and on the width of the mechanically accessible single-phase region in the relevant phase diagram.

5.2.3 Equilibration, Gorsky limit and validity of open-system parameters

The current findings are also related to the classical Gorsky effect. The Gorsky effect describes the time-dependent relaxation of stress in solids containing mobile solutes, driven by stress-induced solute diffusion [125, 128]. In a bent or axially loaded specimen with spatially varying stress, gradients in chemical potential μ cause solute atoms to migrate from regions of high chemical potential to regions of lower chemical potential, thereby redistributing solute and reducing the overall elastic energy.

Open-system elasticity corresponds to the equilibrium limit of the same coupled process. If the characteristic diffusion time across the relevant microstructural length

scale L,

$$\tau_{\mathrm{diff}} \sim \frac{L^2}{D} \tag{5.12}$$

is much shorter than the time scale of mechanical loading τ_{mech}, then solute redistribution can keep pace with the applied stress. In this limit, the material does not exhibit a slow, time-dependent Gorsky relaxation; instead, it responds with modified elastic constants that already incorporate the equilibrium solute redistribution at fixed chemical potential. In other words, the open-system Young's modulus Y^{μ} and Poisson's ratio ν^{μ} encode the final state toward which a Gorsky relaxation would evolve.

Nanoporous metals provide an ideal microstructure. Ligament diameters of a few to a few tens of nanometers imply diffusion lengths that are sufficiently small for hydrogen to equilibrate on timescales far shorter than those of the quasi-static mechanical tests and far below the typical periods of dynamic mechanical analysis used in related studies [25]. As a result, the behaviour of the nanoporous Pd and PdAu samples is well described by equilibrium open-system elasticity, rather than by kinetic Gorsky relaxation.

The applicability of Larché–Cahn open-system elasticity to the present experiments relies on the assumption of local thermodynamic equilibrium with respect to hydrogen redistribution. Several aspects of the experimental design were chosen to ensure that this condition is met as closely as possible.

First, the nanoporous microstructure provides short diffusion paths. With ligament sizes on the order of a few to a few tens of nanometers ($\sim 40\,\mathrm{nm}$ with hierarchical pores for np Pd and $\sim 5\,\mathrm{nm}$ for np PdAu, Figures 5.1 and 5.2), the diffusion time for hydrogen across an individual ligament is extremely small compared to the timescale of the mechanical loading–unloading cycles. Second, hydrogen concentrations were imposed electrochemically by stepwise potentiostatic control, with long equilibration periods at each potential to allow the system to approach a stationary state. Third, the elastic properties were determined from the unloading segments of small-strain (3%) cyclic tests (Figure 5.6), where deformation is fully reversible and plasticity is negligible. Finally, full-field DIC analysis was used to verify that strains were homogeneous at the macroscopic specimen scale and that the Poisson's ratio could be reliably extracted.

Within the x_{H} range that remains in the single-phase α region, the mechanical response of np PdAu is highly reproducible and reversible, and shows no discernible dependence on loading history. The agreement with open-system elasticity predictions in this regime (Figures 5.7 and 5.8) indicates that hydrogen redistribution is effectively equilibrated on the timescale of the tests. At higher x_{H} in np Pd, deviations from the model are observed. These deviations coincide with electrochemical and mechanical signatures associated with the onset of the α–α' transition and the development of two-phase regions. In this regime, the assumptions underlying the single-phase open-system description, in particular local equilibrium and homogeneous composition, are no longer strictly satisfied. As a result, deviations from the ideal Larché–Cahn open-system response are expected.

Overall, the combination of nanoscale ligament dimensions, carefully chosen potential steps and small elastic strain amplitudes provides favorable conditions for testing open-system elasticity in nanoporous Pd-based metals.

5.3 Chapter Summary

This chapter has demonstrated that the elastic Poisson's ratio of nanoporous metals, quantified as open-system properties ν_{E}^{μ}, can be reversibly and continuously modulated through electrochemical hydrogenation. Systematic experiments on np Pd and np PdAu revealed a distinct dependence of both Young's modulus and Poisson's ratio on x_{H}: an initial suppression at low x_{H} followed by partial recovery at higher concentrations. This behaviour is strongly composition-dependent—np Pd exhibits limited tunability and irreversible softening due to proximity to the α–α' miscibility gap, whereas np PdAu displays broad, reversible modulation across a wider hydrogen range, with a maximum reduction in $\nu_{\mathrm{E}}^{\mu}/\nu_0$ approaching 50 %.

The experimental trends are in quantitative agreement with the Larché-Cahn theory of open-system elasticity, which accounts for solute-strain coupling under fixed chemical potential conditions. The observed transitions in ν_{E}^{μ} can be rationalized by the concentration-dependent open-system compliance: in the dilute regime, stress-assisted redistribution amplifies the compliance increase and drives a pronounced reduction of ν_{E}^{μ}; at higher x_{H}, thermodynamic and configurational constraints suppress further softening and enable partial mechanical recovery. These effects are intrinsic to open-system thermodynamics and cannot be captured by conventional closed-system elasticity models.

Au alloying is shown to be a particularly effective means to expand and stabilize the regime in which open-system elasticity can be observed. By modifying the Pd electronic structure, suppressing the α–α' miscibility gap and enhancing hydrogen kinetics, PdAu provides a wide, mechanically robust single-phase window in which composition-dependent elastic constants can be probed and utilized. In this sense, np PdAu–H acts as a chemically adjustable model system for stress–solute coupling in nanostructured metals.

Collectively, these results provide further experimental validation in nanoporous metals and demonstrate that mechanical response can be tuned by electrochemical means. The np PdAu–H system serves as a chemically adjustable model for studying stress–solute coupling in nanostructured materials, offering new design ideas for applications in hydrogen sensing, soft robotics, adaptive actuation and energy conversion systems.

Chapter 6

Summary and Outlook

6.1 Summary

This dissertation demonstrates two complementary routes for tuning Poisson's ratio in nanoporous metal materials: structural hierarchy and chemo-mechanical coupling.

The first part of this work focused on hierarchical network microstructures. Monolithic, crack-free hierarchical nanoporous gold samples with nested bicontinuous structures were synthesized using a three-step dealloying-annealing-dealloying route. This approach enabled independent control of two ligament length scales. The upper-level ligament size was systematically varied from 60 nm to 180 nm, while the lower-level ligament size was tuned in < 20 nm, 20 nm and 40 nm. In situ DIC and strain mapping were employed during uniaxial compression to quantify both axial and transverse strains. From axial and transverse strains the elastic and plastic Poisson's ratios (ν_{E} and ν_{P}) were calculated. The results revealed that both ν_{E} and ν_{P} are relatively insensitive to the upper-level ligament size. This indicates that multiscale structuring does not disrupt the underlying scaling between relative density (solid volume fraction φ_{net}) and effective elastic response. Building on these findings, a scaling law was proposed and experimentally validated to describe the dependence of ν_{E} on φ_{net} in multi-level network materials. These results address an important knowledge gap in the mechanics of hierarchical nanoporous networks and provides an experimentally grounded guideline for designing porous materials with predictable lateral deformation behavior.

The second part of this work examined chemo-mechanical tuning by a mobile interstitial solute. Specifically, the hydrogen content x_{H} was used to dynamically and reversibly modulate the elastic response of nanoporous Pd and nanoporous PdAu under electrochemical control. Combining potentiostatic hydrogenation with in situ DIC during small-strain cyclic compression, we obtain unloading-based elastic Poisson's ratios under near-equilibrium conditions. In the potentiostatic, sufficiently equilibrated limit, these values provide an experimental estimate of the open-system response, enabling a quantitative comparison with predictions from the Larché-Cahn open-system elasticity framework. In both systems, the measured ν_{E} shows a strong and reversible dependence on x_{H}, consistent with open-system theory. Notably, for nanoporous PdAu the normalized open-system Poisson's ratio $\nu_{\mathrm{E}}^{\mu}/\nu_0$ is reduced by nearly 50% at intermediate x_{H} and partially recovers at higher x_{H}, demonstrating pronounced tunability of the lateral elastic response. Au alloying stabilizes the single-phase α solid

solution over an extended composition range, improves mechanical reversibility and provides access to a broader range of x_{H}. Altogether, these findings extend experimental validation of open-system elasticity beyond Young's modulus to include Poisson's ratio and establish a controlled model system for studying solute-mediated mechanical phenomena under electrochemical control.

Taken together, the findings of this dissertation demonstrate that the Poisson's ratio of nanoporous metal materials is not an immutable material constant but can be systematically tuned through structural and compositional design. Structural hierarchy provides a static yet robust route for elastic tailoring, whereas solute-controlled coupling enables dynamic and reversible modulation. These strategies provide practical design guidelines for tailoring the lateral elastic response of porous metals through structural structure and solute-controlled coupling.

6.2 Outlook

First, although the HNPG systems studied in Chapter 4 reveal clear links between microstructure and Poisson's ratio, the present work explores only a limited region of the design space. In particular, the investigated hierarchy and solid fractions remain far from topological transition points and the geometric anisotropy is modest. Consequently, the proposed scaling law has not yet been tested in regimes where lateral deformation is governed primarily by topology rather than density. Extending this work to microstructures with deliberately controlled anisotropy (such as spinoline-inspired structures, re-entrant topologies, or stretch-dominated frameworks) will help determine the limits of the proposed density-Poisson's ratio scaling relationship. Moreover, the present homogenized analyses cannot resolve mesoscale strain localization, which is expected in hierarchical networks. Combining high-resolution finite element modeling with in situ DIC would enable spatially resolved comparisons between predicted and measured deformation modes, thereby probing how local ligament geometry controls the macroscopic Poisson's ratio.

Second, this dissertation has treated structural design and solute-tunable elasticity largely as separate control parameters. A key challenge is to understand how stress-assisted solute redistribution interacts with structural anisotropy to generate spatially heterogeneous elastic responses. In networks with oriented ligaments, graded porosity, or anisotropic connectivity, the stress field is inherently non-uniform; consequently, solute transport is expected to become directionally biased in ways that remain largely unquantified. Progress will require experimental tools capable of mapping hydrogen concentration and strain simultaneously in deforming microstructures. Techniques such as in situ X-ray diffraction or hydrogen-sensitive optical microscopy could be integrated with DIC to visualize stress-guided solute migration. Such datasets are essential for validating emerging multiphysics models that couple diffusion, elasticity and microstructure-dependent load redistribution. Ultimately, these insights could motivate topology-informed design approaches, including topology optimization that explicitly incorporates open-system constitutive behavior to achieve target stiffness gradients and chemo-mechanically switchable deformation modes.

Third, the theoretical description of open-system elasticity remains incomplete for architected metals and for high-solute-loading conditions. The classical Larché-

Cahn formulation assumes infinitesimal strain, local thermodynamic equilibrium and isotropic solute-strain coupling; these assumptions are only approximately satisfied in nanoporous networks. Finite-strain kinematics, ligament-level anisotropy and interfacial or confinement effects can substantially modify the local chemical potential landscape, yet they are not captured by current models. Furthermore, the time dependence of solute migration, especially under stress gradients or during rapid potential steps, must also be addressed beyond the equilibrium (susceptibility-based) limit. Developing constitutive laws that incorporate finite strain, anisotropic coupling coefficients and transport kinetics would provide a physically grounded basis for predicting both transient and steady-state responses under realistic loading conditions. Embedding such laws into continuum and multiscale simulation tools is a necessary step toward predictive design of mechanically tunable structures rather than post-hoc interpretation of experimental observations.

Finally, extending solute-modulated elasticity beyond the Pd-H system would be highly meaningful, although it will require reassessing the underlying thermodynamic and kinetic assumptions. Interstitial solutes such as Li, Na, B, C and N in transition-metal alloys and high-entropy alloys introduce additional complexity, including stronger solute-solute interactions, multiple occupancy sites, sluggish diffusion and competing phase transformations. These effects challenge existing open-system formulations but may also enable unusual or strongly nonlinear elastic responses, including direction-dependent auxeticity, stress-amplified softening, or negative linear compressibility. Realizing such behavior will depend on integrating improved chemo-mechanical theories with alloy and microstructure design strategies that explicitly leverage solute–structure interactions.

Overall, this dissertation establishes a mechanistic foundation for understanding and controlling Poisson's ratio in nanoporous metals through the combined effects of microstructure and solute redistribution. The framework developed here links nanoscale geometry, thermodynamics and mechanics and offers a pathway toward predictive design of chemically adaptive architected materials, while also identifying the experimental and theoretical advances required to fully exploit solute-modulated elasticity.

Bibliography

[1] Sebastian Polarz and Bernd Smarsly. Nanoporous materials. *Journal of nanoscience and nanotechnology*, 2(6):581–612, 2002.

[2] Yi Ding and Zhonghua Zhang. Nanoporous metals. In *Springer Handbook of Nanomaterials*, pages 779–818. Springer, 2013.

[3] GQ Lu and XS Zhao. Nanoporous materials: An overview. *Nanoporous materials: science and engineering*, 4:1–12, 2004.

[4] Theresa Juarez, Juergen Biener, Jörg Weissmüller, and Andrea M Hodge. Nanoporous metals with structural hierarchy: A review. *Advanced Engineering Materials*, 19(12):1700389, 2017.

[5] Yi Ding and Zhonghua Zhang. *Nanoporous metals for advanced energy technologies*. Springer, 2016.

[6] Erkin Seker, Michael L Reed, and Matthew R Begley. Nanoporous gold: Fabrication, characterization, and applications. *Materials*, 2(4):2188–2215, 2009.

[7] Masataka Hakamada and Mamoru Mabuchi. Fabrication of nanoporous palladium by dealloying and its thermal coarsening. *Journal of Alloys and Compounds*, 479 (1-2):326–329, 2009.

[8] Shan Shi, Jürgen Markmann, and Jörg Weissmüller. Synthesis of uniform bulk nanoporous palladium with tunable structure. *Electrochimica acta*, 285:60–69, 2018.

[9] Haonan Sun, Yizhou Huang, and Shan Shi. Bulk nanoporous platinum for electrochemical actuation. *Energy Materials and Devices*, 2023.

[10] Nadiia Mameka, Ke Wang, Jürgen Markmann, Erica T Lilleodden, and Jörg Weissmüller. Nanoporous gold—testing macro-scale samples to probe small-scale mechanical behavior. *Materials Research Letters*, 4(1):27–36, 2016.

[11] Hai-Jun Jin, Xiao-Lan Wang, Smrutiranjan Parida, Ke Wang, Masahiro Seo, and Jörg Weissmüller. Nanoporous au- pt alloys as large strain electrochemical actuators. *Nano letters*, 10(1):187–194, 2010.

[12] Shan Shi, Jürgen Markmann, and Jörg Weissmüller. Actuation by hydrogen electrosorption in hierarchical nanoporous palladium. *Philosophical Magazine*, 97 (19):1571–1587, 2017.

[13] Rong Li and Karl Sieradzki. Ductile-brittle transition in random porous au. *Physical Review Letters*, 68(8):1168, 1992.

[14] Hai-Jun Jin, Lilia Kurmanaeva, Jörg Schmauch, Harald Rösner, Yulia Ivanisenko, and Jörg Weissmüller. Deforming nanoporous metal: Role of lattice coherency. *Acta Materialia*, 57(9):2665–2672, 2009.

[15] Nilesh Badwe, Xiying Chen, and Karl Sieradzki. Mechanical properties of nanoporous gold in tension. *Acta Materialia*, 129:251–258, 2017.

[16] Nicolas J Briot, Tobias Kennerknecht, Christoph Eberl, and T John Balk. Mechanical properties of bulk single crystalline nanoporous gold investigated by millimetre-scale tension and compression testing. *Philosophical Magazine*, 94(8): 847–866, 2014.

[17] Jörg Weissmüller and Karl Sieradzki. Dealloyed nanoporous materials with interface-controlled behavior. *Mrs Bulletin*, 43(1):14–19, 2018.

[18] Hai-Jun Jin, Jörg Weissmüller, and Diana Farkas. Mechanical response of nanoporous metals: A story of size, surface stress, and severed struts. *Mrs Bulletin*, 43(1):35–42, 2018.

[19] Hai-Jun Jin and Jörg Weissmüller. A material with electrically tunable strength and flow stress. *Science*, 332(6034):1179–1182, 2011.

[20] Shaofeng Sun, Xiying Chen, Nilesh Badwe, and Karl Sieradzki. Potential-dependent dynamic fracture of nanoporous gold. *Nature materials*, 14(9):894–898, 2015.

[21] Nadiia Mameka, Jürgen Markmann, Hai-Jun Jin, and Jörg Weissmüller. Electrical stiffness modulation—confirming the impact of surface excess elasticity on the mechanics of nanomaterials. *Acta materialia*, 76:272–280, 2014.

[22] Shan Shi, Yong Li, Bao-Nam Ngo-Dinh, Jürgen Markmann, and Jörg Weissmüller. Scaling behavior of stiffness and strength of hierarchical network nanomaterials. *Science*, 371(6533):1026–1033, 2021.

[23] Hai-Jun Jin and Jörg Weissmüller. Bulk nanoporous metal for actuation. *Advanced engineering materials*, 12(8):714–723, 2010.

[24] Xinxin Xiao, Pengchao Si, and Edmond Magner. An overview of dealloyed nanoporous gold in bioelectrochemistry. *Bioelectrochemistry*, 109:117–126, 2016.

[25] Shan Shi, Jürgen Markmann, and Jörg Weissmüller. Verifying larché–cahn elasticity, a milestone of 20th-century thermodynamics. *Proceedings of the National Academy of Sciences*, 115(43):10914–10919, 2018.

[26] Shan Shi. *Chemo-mechanical coupling in nanoporous palladium-hydrogen*. PhD thesis, Dissertation, Hamburg, Technische Universität Hamburg, 2019, 2019.

[27] Lukas Lührs, Celal Soyarslan, Jürgen Markmann, Swantje Bargmann, and Jörg Weissmüller. Elastic and plastic poisson's ratios of nanoporous gold. *Scripta Materialia*, 110:65–69, 2016.

[28] Lukas Lührs, Birthe Zandersons, Norbert Huber, and Jörg Weissmüller. Plastic poisson's ratio of nanoporous metals: A macroscopic signature of tension–compression asymmetry at the nanoscale. *Nano letters*, 17(10):6258–6266, 2017.

[29] Nadiia Mameka. *Surface-controlled mechanical properties of bulk nanoporous gold*. PhD thesis, Technische Universität Hamburg-Harburg, 2016.

[30] FD Manchester, A San-Martin, and John M Pitre. The h-pd (hydrogen-palladium) system. *Journal of phase equilibria*, 15(1):62–83, 1994.

[31] Ted B Flanagan and WA Oates. The palladium-hydrogen system. In *Proceedings: EPRI-NSF Workshop on Anomalous Effects in Deuterided Metals*, 1991.

[32] Brian D Adams and Aicheng Chen. The role of palladium in a hydrogen economy. *Materials today*, 14(6):282–289, 2011.

[33] Peter H Mott, John R Dorgan, and CM Roland. The bulk modulus and poisson's ratio of "incompressible" materials. *Journal of Sound and Vibration*, 312(4-5): 572–575, 2008.

[34] James M Gere and SP Timoshenko. Mechanics of materials. ed. *Boston, MA: PWS*, 1997.

[35] Raymond W Ogden. *Non-linear elastic deformations*. Courier Corporation, 1997.

[36] Norbert Huber, RN Viswanath, Nadiia Mameka, Jürgen Markmann, and Jörg Weißmüller. Scaling laws of nanoporous metals under uniaxial compression. *Acta materialia*, 67:252–265, 2014.

[37] Celal Soyarslan, Swantje Bargmann, Marc Pradas, and Jörg Weissmüller. 3d stochastic bicontinuous microstructures: Generation, topology and elasticity. *Acta materialia*, 149:326–340, 2018.

[38] Haonan Sun, Lukas Lührs, Wei-Che Chang, and Shan Shi. Scaling behaviour of poisson's ratio in hierarchical nanoscale network materials. *Acta Materialia*, page 121393, 2025.

[39] Francis Larché and John W Cahn. A linear theory of thermochemical equilibrium of solids under stress. *Acta metallurgica*, 21(8):1051–1063, 1973.

[40] Francis Larché and John W Cahn. A nonlinear theory of thermochemical equilibrium of solids under stress. *Acta Metallurgica*, 26(1):53–60, 1978.

[41] Hai-Jun Jin, Jiuhui Han, and Qing Chen. Nontraditional dealloying methods, novel nanoporous materials, and new opportunities: H.-j. jin et al. *MRS Bulletin*, 50(5):608–617, 2025.

[42] Jonah Erlebacher, Michael J Aziz, Alain Karma, Nikolay Dimitrov, and Karl Sieradzki. Evolution of nanoporosity in dealloying. *nature*, 410(6827):450–453, 2001.

[43] Jörg Weissmüller, Roger C Newman, Hai-Jun Jin, Andrea M Hodge, and Jeffrey W Kysar. Nanoporous metals by alloy corrosion: formation and mechanical properties. *Mrs Bulletin*, 34(8):577–586, 2009.

[44] Erkin Şeker, Wei-Chuan Shih, and Keith J Stine. Nanoporous metals by alloy corrosion: Bioanalytical and biomedical applications. *MRS bulletin*, 43(1):49–56, 2018.

[45] Ian McCue, Alain Karma, and Jonah Erlebacher. Pattern formation during electrochemical and liquid metal dealloying. *Mrs Bulletin*, 43(1):27–34, 2018.

[46] S Parida, D Kramer, CA Volkert, H Rösner, J Erlebacher, and J Weissmüller. Volume change during the formation of nanoporous gold by dealloying. *Physical Review Letters*, 97(3):035504, 2006.

[47] Yi Zhong, Jürgen Markmann, Hai-Jun Jin, Yulia Ivanisenko, Lilia Kurmanaeva, and Jörg Weissmüller. Crack mitigation during dealloying of $Au_{25}Cu_{75}$. *Advanced Engineering Materials*, 16(4):389–398, 2014.

[48] A Dursun, DV Pugh, and SG Corcoran. Dealloying of ag-au alloys in halide-containing electrolytes: affect on critical potential and pore size. *Journal of the Electrochemical Society*, 150(7):B355, 2003.

[49] LH Qian and MW Chen. Ultrafine nanoporous gold by low-temperature dealloying and kinetics of nanopore formation. *Applied Physics Letters*, 91(8), 2007.

[50] Zhen Qi and Jörg Weissmüller. Hierarchical nested-network nanostructure by dealloying. *Acs Nano*, 7(7):5948–5954, 2013.

[51] Ian McCue, Ellen Benn, Bernard Gaskey, and Jonah Erlebacher. Dealloying and dealloyed materials. *Annual review of materials research*, 46:263–286, 2016.

[52] Ling-Zhi Liu, Xing-Long Ye, and Hai-Jun Jin. Interpreting anomalous low-strength and low-stiffness of nanoporous gold: Quantification of network connectivity. *Acta Materialia*, 118:77–87, 2016.

[53] Nadiia Mameka, Jürgen Markmann, and Jörg Weissmüller. On the impact of capillarity for strength at the nanoscale. *Nature communications*, 8(1):1976, 2017.

[54] Yan Zhang, Xinjiang Cui, Feng Shi, and Youquan Deng. Nano-gold catalysis in fine chemical synthesis. *Chemical Reviews*, 112(4):2467–2505, 2012.

[55] Li Wang, Xingyuan Xu, Jun Chen, Weiguang Su, Feng Zhang, Anqing Li, Chao Li, Chonghai Xu, and Yu Sun. Crack sensing of cardiomyocyte contractility with high sensitivity and stability. *ACS nano*, 16(8):12645–12655, 2022.

[56] Fanhui Meng and Yi Ding. Sub-micrometer-thick all-solid-state supercapacitors with high power and energy densities. *Advanced Materials (Weinheim)*, 23, 2011.

[57] Stefan Wild, Christoph Mahr, Andreas Rosenauer, Thomas Risse, Sergey Vasenkov, and Marcus Bäumer. New perspectives for evaluating the mass transport in porous catalysts and unfolding macro-and microkinetics. *Catalysis Letters*, 153(11):3405–3422, 2023.

[58] Tianshui Yu, Xiangji Zhou, Yu Chen, Jin Chen, Songliu Yuan, Lihua Qian, Xianglong Lu, Pan Liu, Pengxiang Lei, and Xiuhong Li. Intrinsic contribution of mass transport within nanoscale channels of nanoporous gold for co2 electrochemical reduction. *Advanced Materials Interfaces*, 9(24):2200895, 2022.

[59] Congcheng Wang, Anson Tsang, Yingji Sang, Diwen Xiao, Yuan Xu, Shida Yang, Ling-Zhi Liu, Qiang Zheng, Pan Liu, Hai-Jun Jin, et al. The microstructural dependence of ionic transport in bi-continuous nanoporous metal. *Acta Materialia*, 276:120134, 2024.

[60] Maryanne M Collinson. Nanoporous gold electrodes and their applications in analytical chemistry. *International Scholarly Research Notices*, 2013(1):692484, 2013.

[61] Zhen Qi, Steven A Hawks, Corie Horwood, Juergen Biener, and Monika M Biener. Mitigating mass transport limitations: Hierarchical nanoporous gold flow-through electrodes for electrochemical co 2 reduction. *Materials Advances*, 3(1):381–388, 2022.

[62] Yi Ding and Jonah Erlebacher. Nanoporous metals with controlled multimodal pore size distribution. *Journal of the American Chemical Society*, 125(26):7772–7773, 2003.

[63] Huimei Duan, Qin Hao, and Caixia Xu. Hierarchical nanoporous ptti alloy as highly active and durable electrocatalyst toward oxygen reduction reaction. *Journal of Power Sources*, 280:483–490, 2015.

[64] Jie Zhang, Qingguo Bai, and Zhonghua Zhang. Dealloying-driven nanoporous palladium with superior electrochemical actuation performance. *Nanoscale*, 8(13): 7287–7295, 2016.

[65] Qingquan Kong, Lixian Lian, Ying Liu, Jing Zhang, Li Wang, and Wei Feng. Bulk hierarchical nanoporous palladium prepared by dealloying pdal alloys and its electrochemical properties. *Microporous and Mesoporous Materials*, 208:152–159, 2015.

[66] Qingquan Kong, Lixian Lian, Ying Liu, and Jing Zhang. Fabrication and compression properties of bulk hierarchical nanoporous copper with fine ligament. *Materials Letters*, 127:59–62, 2014.

[67] H-J Qiu, Y Ito, and MW Chen. Hierarchical nanoporous nickel alloy as three-dimensional electrodes for high-efficiency energy storage. *Scripta Materialia*, 89: 69–72, 2014.

[68] Xuequan Li, Baisheng Huang, Cuicui Qiu, Zhou Li, Li-Hua Shao, and Hong Liu. Hierarchical nested-network porous copper fabricated by one-step dealloying for glucose sensing. *Journal of Alloys and Compounds*, 681:109–114, 2016.

[69] Neil Gaspar, XJ Ren, Chris W Smith, JN Grima, and Ken E Evans. Novel honeycombs with auxetic behaviour. *Acta Materialia*, 53(8):2439–2445, 2005.

[70] M Bianchi, F Scarpa, and CW Smith. Shape memory behaviour in auxetic foams: Mechanical properties. *Acta Materialia*, 58(3):858–865, 2010.

[71] Kenneth E Evans and Andrew Alderson. Auxetic materials: functional materials and structures from lateral thinking! *Advanced materials*, 12(9):617–628, 2000.

[72] Roderic Lakes. Foam structures with a negative poisson's ratio. *Science*, 235 (4792):1038–1040, 1987.

[73] Kenneth E Evans, MA Nkansah, IJ Hutchinson, and SC Rogers. Molecular network design. *Nature*, 353(6340):124–124, 1991.

[74] George Neville Greaves, A Lindsay Greer, Roderic S Lakes, and Tanguy Rouxel. Poisson's ratio and modern materials. *Nature materials*, 10(11):823–837, 2011.

[75] Zbigniew D Jastrzebski. *Nature and properties of engineering materials*. John Wiley and Sons, Inc., New York, 1976.

[76] Hao Wu, Minghui Fu, Mingming Chen, Wen Jiang, Rongchang Zhong, Binbin Zheng, and Jingxiang Huang. A novel metamaterial with instantaneously sign-switchable coefficient of thermal expansion and poisson's ratio. *Mechanics of Materials*, 192:104974, 2024.

[77] Ye Zhou, Qidong Yang, and Kai Wei. Additively manufactured multi-functional metamaterials: low coefficient of thermal expansion and programmable poisson's ratio. *Virtual and Physical Prototyping*, 19(1):e2303714, 2024.

[78] Angelina Müller, Matthias C Wapler, and Ulrike Wallrabe. A quick and accurate method to determine the poisson's ratio and the coefficient of thermal expansion of pdms. *Soft Matter*, 15(4):779–784, 2019.

[79] L Ai and X-L Gao. Metamaterials with negative poisson's ratio and non-positive thermal expansion. *Composite Structures*, 162:70–84, 2017.

[80] Jie-Hua Zhao, Yong Du, Michael Morgen, and Paul S Ho. Simultaneous measurement of young's modulus, poisson ratio, and coefficient of thermal expansion of thin films on substrates. *Journal of Applied Physics*, 87(3):1575–1577, 2000.

[81] Luca D'Andrea, Roberta Gabrieli, Lorenzo Milano, Luca Magagnin, Anna De Cet, Dario Alidoost, Martin Schwentenwein, Enrica Verné, Francesco Baino, and Pasquale Vena. Elastic and failure characterization of hydroxyapatite tpms scaffolds using a combined approach of ultrasound, compression tests and micro-ct based numerical models. *Acta Materialia*, page 120776, 2025.

[82] MJ Bamber, KE Cooke, AB Mann, and B Derby. Accurate determination of young's modulus and poisson's ratio of thin films by a combination of acoustic microscopy and nanoindentation. *Thin Solid Films*, 398:299–305, 2001.

[83] Barbara Howell, Pat Prendergast, and Larry Hansen. Examination of acoustic behavior of negative poisson's ratio materials. *Applied Acoustics*, 43(2):141–148, 1994.

[84] Johannes Ast, Mathias Göken, and Karsten Durst. Size-dependent fracture toughness of tungsten. *Acta Materialia*, 138:198–211, 2017.

[85] SV Madge, DV Louzguine-Luzgin, JJ Lewandowski, and AL Greer. Toughness, extrinsic effects and poisson's ratio of bulk metallic glasses. *Acta Materialia*, 60 (12):4800–4809, 2012.

[86] JP Donoghue, KL Alderson, and KE Evans. The fracture toughness of composite laminates with a negative poisson's ratio. *physica status solidi (b)*, 246(9):2011–2017, 2009.

[87] Xuhui Zhang, Xun Wu, Wenpeng Wu, and Lei Wang. Mechanical response and energy absorption of bridge block with negative poisson's ratio. *Soil Dynamics and Earthquake Engineering*, 171:107972, 2023.

[88] Leslie G Jaeger and Baidar Bakht. Effect of poisson's ratio and beam spacing on grillage analysis of slab bridges. *Canadian Journal of Civil Engineering*, 15(5): 821–827, 1988.

[89] Roy Edward Rowe. A load distribution theory for bridge slabs allowing for the effect of poisson's ratio. *Magazine of Concrete Research*, 7(20):69–78, 1955.

[90] Tao Wang, Junhan An, Huan He, Xin Wen, and Xulong Xi. A novel 3d impact energy absorption structure with negative poisson's ratio and its application in aircraft crashworthiness. *Composite Structures*, 262:113663, 2021.

[91] Shubo Xu, Xue Yanga, Xinzhi Hua, Hailong Maa, Jianing Lia, and Guocheng Rena. Preparation of negative poisson's ratio 316l stainless steel porous bone scaffolds based on finite element analysis and 3d printing technology. *Materials Research*, 28:e20240479, 2025.

[92] Wande Zhang, Pranav Soman, Kyle Meggs, Xin Qu, and Shaochen Chen. Tuning the poisson's ratio of biomaterials for investigating cellular response. *Advanced functional materials*, 23(25):3226–3232, 2013.

[93] Georg Watzl, Christian Kerschbaummayr, Martin Schagerl, Thomas Mitter, Bernhard Sonderegger, and Clemens Grünsteidl. In situ laser-ultrasonic monitoring of poisson's ratio and bulk sound velocities of steel plates during thermal processes. *Acta Materialia*, 235:118097, 2022.

[94] Hao Zhan, Dan Guo, and GuoXin Xie. Two-dimensional layered materials: from mechanical and coupling properties towards applications in electronics. *Nanoscale*, 11(28):13181–13212, 2019.

[95] Jong Hun Kim, Jae Hwan Jeong, Namwon Kim, Rakesh Joshi, and Gwan-Hyoung Lee. Mechanical properties of two-dimensional materials and their applications. *Journal of Physics D: Applied Physics*, 52(8):083001, 2018.

[96] R De Borst, Lambertus J Sluys, H-B Muhlhaus, and Jerzy Pamin. Fundamental issues in finite element analyses of localization of deformation. *Engineering computations*, 10(2):99–121, 1993.

[97] M Sevimay, F Turhan, MA Kiliçarslan, and G Eskitascioglu. Three-dimensional finite element analysis of the effect of different bone quality on stress distribution in an implant-supported crown. *The Journal of prosthetic dentistry*, 93(3):227–234, 2005.

[98] Kaixiong Hu, Markus Ziehmer, Ke Wang, and Erica T Lilleodden. Nanoporous gold: 3d structural analyses of representative volumes and their implications on scaling relations of mechanical behaviour. *Philosophical Magazine*, 96(32-34): 3322–3335, 2016.

[99] Tereza Uhlířová and Willi Pabst. Poisson's ratio of porous and cellular materials with randomly distributed isometric pores or cells. *Journal of the American Ceramic Society*, 103(12):6961–6977, 2020.

[100] Hansol Jeon, Jürgen Markmann, and Shan Shi. Effects of structural hierarchy and size on mechanical behavior of nanoporous gold. *Acta Materialia*, 273:119954, 2024.

[101] Zhengqing John Qi, Colin Daniels, Sung Ju Hong, Yung Woo Park, Vincent Meunier, Marija Drndic, and AT Charlie Johnson. Electronic transport of recrystallized freestanding graphene nanoribbons. *ACS nano*, 9(4):3510–3520, 2015.

[102] Lukas Riedel, Jürgen Markmann, Jörg Weissmüller, and Shan Shi. Tailoring hierarchical nanoporous gold on dual length scales. *Physical review materials*, 7 (11):116001, 2023.

[103] Anthony P Roberts and Edward J Garboczi. Computation of the linear elastic properties of random porous materials with a wide variety of microstructure. *Proceedings of the Royal Society of London. Series A: Mathematical, Physical and Engineering Sciences*, 458(2021):1033–1054, 2002.

[104] Ken E Evans. Auxetic polymers: a new range of materials. *Endeavour*, 15(4): 170–174, 1991.

[105] Vijay A Sethuraman, Venkat Srinivasan, Allan F Bower, and Pradeep R Guduru. In situ measurements of stress-potential coupling in lithiated silicon. *Journal of the Electrochemical Society*, 157(11):A1253, 2010.

[106] Zhiwei Cui, Feng Gao, and Jianmin Qu. A finite deformation stress-dependent chemical potential and its applications to lithium ion batteries. *Journal of the Mechanics and Physics of Solids*, 60(7):1280–1295, 2012.

[107] MP Gururajan and Arka Lahiri. Elastic stress effects on microstructural instabilities. *arXiv preprint arXiv:1607.00599*, 2016.

[108] Nitin Muralidharan, Casey N Brock, Adam P Cohn, Deanna Schauben, Rachel E Carter, Landon Oakes, D Greg Walker, and Cary L Pint. Tunable mechanochemistry of lithium battery electrodes. *ACS nano*, 11(6):6243–6251, 2017.

[109] FA Lewis, JP Magennis, SG McKee, and PJM Ssebuwufu. Hydrogen chemical potentials and diffusion coefficients in hydrogen diffusion membranes. *Nature*, 306 (5944):673–675, 1983.

[110] JL Waisman, George Sines, and LB Robinson. Diffusion of hydrogen in titanium alloys due to composition, temperature, and stress gradients. *Metallurgical transactions*, 4(1):291–302, 1973.

[111] S Morito, H Tanaka, R Konishi, T Furuhara, and Maki. The morphology and crystallography of lath martensite in fe-c alloys. *Acta materialia*, 51(6):1789–1799, 2003.

[112] T Grosdidier, A Hazotte, and A Simon. Precipitation and dissolution processes in γ/γ' single crystal nickel-based superalloys. *Materials Science and Engineering: A*, 256(1-2):183–196, 1998.

[113] Tresa M Pollock and Sammy Tin. Nickel-based superalloys for advanced turbine engines: chemistry, microstructure and properties. *Journal of propulsion and power*, 22(2):361–374, 2006.

[114] RC Reed. The superalloys: Fundamentals and applications, cambridge university press, cambridge, 2006, 2006.

[115] J Völkl and G Alefeld. Diffusion of hydrogen in metals. In *Hydrogen in metals I: basic properties*, pages 321–348. Springer, 2005.

[116] Y Mishin. Calculation of open and closed system elastic coefficients for multicomponent solids. *Physical Review B*, 91(22):224107, 2015.

[117] Perry H Leo and RF Sekerka. The effect of elastic fields on the morphological stability of a precipitate grown from solid solution. *Acta metallurgica*, 37(12): 3139–3149, 1989.

[118] ME Thompson, CS Su, and Peter W Voorhees. The equilibrium shape of a misfitting precipitate. *Acta metallurgica et materialia*, 42(6):2107–2122, 1994.

[119] Peter Fratzl, Oliver Penrose, and Joel L Lebowitz. Modeling of phase separation in alloys with coherent elastic misfit. *Journal of Statistical Physics*, 95(5):1429–1503, 1999.

[120] R Mukherjee, TA Abinandanan, and MP Gururajan. Phase field study of precipitate growth: Effect of misfit strain and interface curvature. *Acta Materialia*, 57 (13):3947–3954, 2009.

[121] Matthew T McDowell, Seok Woo Lee, William D Nix, and Yi Cui. 25th anniversary article: understanding the lithiation of silicon and other alloying anodes for lithium-ion batteries. *Advanced materials*, 25(36):4966–4985, 2013.

[122] Lei Chen, Feifei Fan, Liang Hong, James Chen, Yanzhou Z Ji, SL Zhang, T Zhu, and LQ Chen. A phase-field model coupled with large elasto-plastic deformation: application to lithiated silicon electrodes. *Journal of The Electrochemical Society*, 161(11):F3164, 2014.

[123] Eva-Maria Steyskal, Christopher Wiednig, Norbert Enzinger, and Roland Würschum. In situ characterization of hydrogen absorption in nanoporous palladium produced by dealloying. *Beilstein Journal of Nanotechnology*, 7(1):1197–1201, 2016.

[124] RN Viswanath and Jörg Weissmüller. Electrocapillary coupling coefficients for hydrogen electrosorption on palladium. *Acta materialia*, 61(16):6301–6309, 2013.

[125] WS Gorski. Theorie der elastischen nachwirkung in ungeordneten mischkristallen zweiter. *Phys. Z. Sowj*, 8:457–471, 1935.

[126] Olivier Hardouin Duparc and Alexander Krajnikov. Vadim gorsky, a forgotten physics pioneer. *physics today*, 2017.

[127] G Alefeld, G Schaumann, J Tretkowski, and J Völkl. Ferroelasticity of niobium due to hydrogen as a lattice gas. *Physical Review Letters*, 22(14):697, 1969.

[128] J Völkl. The gorsky effect. *Berichte der Bunsengesellschaft für physikalische Chemie*, 76(8):797–805, 1972.

[129] K Kandasamy and FA Lewis. Important gorsky effect influences on diffusion coefficients in metal–hydrogen systems. *International journal of hydrogen energy*, 24(8):763–769, 1999.

[130] Walther Nernst. Die elektromotorische Wirksamkeit der Jonen. *Zeitschrift für physikalische Chemie*, 4(1):129–181, 1889.

[131] Karl Sieradzki, N Dimitrov, C McCall, N Vasiljevic, and J Erlebacher. The dealloying critical potential. *Journal of the Electrochemical Society*, 149(8):B370, 2002.

[132] DM Artymowicz, J Erlebacher, and RC Newman. Relationship between the parting limit for de-alloying and a particular geometric high-density site percolation threshold. *Philosophical Magazine*, 89(21):1663–1693, 2009.

[133] G Tammann. Zum Gedächtnis der Entdeckung des Isomorphismus vor 100 Jahren. Die chemischen und galvanischen Eigenschaften von Mischkristallreihen und ihre Atomverteilung. *Zeitschrift für anorganische und allgemeine Chemie*, 107(1): 1–239, 1919.

[134] Dietrich Stauffer and Ammon Aharony. *Introduction to percolation theory*. Taylor & Francis, 2018.

[135] K Sieradzki, RR Corderman, K Shukla, and RC Newman. Computer simulations of corrosion: selective dissolution of binary alloys. *Philosophical Magazine A*, 59 (4):713–746, 1989.

[136] Karl Sieradzki, JS Kim, AT Cole, and RC Newman. The relationship between dealloying and transgranular stress-corrosion cracking of Cu – Zn and Cu – Al alloys. *Journal of the Electrochemical Society*, 134(7):1635, 1987.

[137] William W Mullins. Theory of thermal grooving. *Journal of Applied Physics*, 28 (3):333–339, 1957.

[138] WW Mullins and PG Shewmon. The kinetics of grain boundary grooving in copper. *Acta Metallurgica*, 7(3):163–170, 1959.

[139] Hansol Jeon, Na-Ri Kang, Eun-Ji Gwak, Jae-il Jang, Heung Nam Han, Jun Yeon Hwang, Sukbin Lee, and Ju-Young Kim. Self-similarity in the structure of coarsened nanoporous gold. *Scripta Materialia*, 137:46–49, 2017.

[140] Lev D Landau, Evgenii M Lifshitz, RJ Atkin, and N Fox. The theory of elasticity. In *Physics of Continuous Media*, pages 167–178. CRC Press, 2020.

[141] John Frederick Nye. *Physical properties of crystals: their representation by tensors and matrices*. Oxford university press, 1985.

[142] Anatolii Isakovich Lurie. *Theory of elasticity*. Springer Science & Business Media, 2010.

[143] George Ellwood Dieter and David Bacon. *Mechanical metallurgy*, volume 3. McGraw-hill New York, 1976.

[144] Lorna J Gibson, Michael Farries Ashby, GS Schajer, and CI Robertson. The mechanics of two-dimensional cellular materials. *Proceedings of the Royal Society of London. A. Mathematical and Physical Sciences*, 382(1782):25–42, 1982.

[145] LJ Gibson and MF Ashby. Cellular solids: Structure and properties, cambridge univ. *Published online*, 1999.

[146] Jonah Erlebacher. Mechanism of coarsening and bubble formation in high-genus nanoporous metals. *Physical review letters*, 106(22):225504, 2011.

[147] Yong Li, Bao-Nam Dinh Ngô, Jürgen Markmann, and Jörg Weissmüller. Topology evolution during coarsening of nanoscale metal network structures. *Physical review materials*, 3(7), 2019.

[148] Joseph R Davis. *Metals handbook desk edition*. ASM international, 1998.

[149] T John Balk, Chris Eberl, Ye Sun, Kevin J Hemker, and Daniel S Gianola. Tensile and compressive microspecimen testing of bulk nanoporous gold. *Jom*, 61:26–31, 2009.

[150] Michael Bürckert, Nicolas J Briot, and T John Balk. Uniaxial compression testing of bulk nanoporous gold. *Philosophical Magazine*, 97(15):1157–1178, 2017.

[151] FC Larche and John W Cahn. The interactions of composition and stress in crystalline solids. *Journal of research of the National Bureau of Standards*, 89(6): 467, 1984.

[152] FC Larché and John W Cahn. Overview no. 41 the interactions of composition and stress in crystalline solids. *Acta metallurgica*, 33(3):331–357, 1985.

[153] Lev Davidovich Landau, LP Pitaevskii, Arnold Markovich Kosevich, and Evgenii Mikhailovich Lifshitz. *Theory of elasticity: volume 7*, volume 7. Elsevier, 2012.

[154] Phillip L Gould and Yuan Feng. *Introduction to linear elasticity*, volume 2. Springer, 1994.

[155] C Lemier and J Weissmüller. Grain boundary segregation, stress and stretch: Effects on hydrogen absorption in nanocrystalline palladium. *Acta materialia*, 55 (4):1241–1254, 2007.

[156] David A Porter and Kenneth E Easterling. *Phase transformations in metals and alloys (revised reprint)*. CRC press, 2009.

[157] Hai-Jun Jin, Smrutiranjan Parida, Dominik Kramer, and Jörg Weissmüller. Sign-inverted surface stress-charge response in nanoporous gold. *Surface Science*, 602 (23):3588–3594, 2008.

[158] Caroline A Schneider, Wayne S Rasband, and Kevin W Eliceiri. Nih image to imagej: 25 years of image analysis. *Nature methods*, 9(7):671–675, 2012.

[159] Gideon Henkelmann, Diana Waldow, Maowen Liu, Lukas Lührs, Yong Li, and Jörg Weissmüller. Self-detachment and subsurface densification of dealloyed nanoporous thin films. *Nano letters*, 22(16):6787–6793, 2022.

[160] Hansol Jeon, Sukbin Lee, and Ju-Young Kim. Tension-compression asymmetry in plasticity of nanoporous gold. *Acta Materialia*, 199:340–351, 2020.

[161] Lukas. Lührs. *Mechanical properties of nanoporous metals: model experiments and technology-relevant materials*. PhD thesis, Technische Universität Hamburg, Hamburg, Germany, 2020.

[162] Seoyun Sohn, Claudia Richert, Shan Shi, Jörg Weissmüller, and Norbert Huber. Scaling between elasticity and topological genus for random network nanomaterials. *Extreme Mechanics Letters*, 68:102147, 2024.

[163] Yijuan Wu, Jürgen Markmann, and Erica T Lilleodden. On the consequences of intrinsic and extrinsic size effects on the mechanical response of nanoporous au. *Materials & Design*, 232:112175, 2023.

[164] Ling-Zhi Liu, Ye-Yuan Zhang, and Hai-Jun Jin. On correlation between the hardness-to-strength ratio and the plastic poisson's ratio of nanoporous gold. *Materials Research Letters*, 11(6):454–461, 2023.

[165] Birthe Zandersons, Lukas Lührs, Yong Li, and Jörg Weissmüller. On factors defining the mechanical behavior of nanoporous gold. *Acta materialia*, 215:116979, 2021.

[166] Phillip Ahn and Oluwaseyi Balogun. Elastic characterization of nanoporous gold foams using laser based ultrasonics. *Ultrasonics*, 54(3):795–800, 2014.

[167] Kodanda Ram Mangipudi, Eike Epler, and Cynthia A Volkert. Topology-dependent scaling laws for the stiffness and strength of nanoporous gold. *Acta Materialia*, 119:115–122, 2016.

[168] Trushal Sardhara, Alexander Shkurmanov, Yong Li, Lukas Riedel, Shan Shi, Christian J Cyron, Roland C Aydin, and Martin Ritter. Enhancing 3d reconstruction accuracy of fib tomography data using multi-voltage images and multimodal machine learning. *Nanomanufacturing and metrology*, 7(1):4, 2024.

[169] Trushal Sardhara, Alexander Shkurmanov, Yong Li, Shan Shi, Christian J Cyron, Roland C Aydin, and Martin Ritter. Role of slice thickness quantification in the 3d reconstruction of fib tomography data of nanoporous materials. *Ultramicroscopy*, 256:113878, 2024.

[170] CA Volkert, ET Lilleodden, D Kramer, and J Weissmüller. Approaching the theoretical strength in nanoporous au. *Applied Physics Letters*, 89(6), 2006.

[171] Ye-Yuan Zhang, Lijie Zou, Ling-Zhi Liu, Hui Xie, Cui-Hong Li, and Hai-Jun Jin. Mechanical properties of unidirectional nanoporous gold under compression. *Acta Materialia*, 235:118078, 2022.

[172] KR Mangipudi, E Epler, and CA Volkert. On the multiaxial yielding and hardness to yield stress relation of nanoporous gold. *Scripta Materialia*, 146:150–153, 2018.

[173] AM Hodge, J Biener, JR Hayes, PM Bythrow, CA Volkert, and AV Hamza. Scaling equation for yield strength of nanoporous open-cell foams. *Acta Materialia*, 55(4): 1343–1349, 2007.

[174] MC Shaw and T Sata. The plastic behavior of cellular materials. *International Journal of Mechanical Sciences*, 8(7):469–478, 1966.

[175] Ronald E Miller. A continuum plasticity model for the constitutive and indentation behaviour of foamed metals. *International Journal of Mechanical Sciences*, 42(4): 729–754, 2000.

[176] Hiroaki Okamoto, TB Massalski, et al. Binary alloy phase diagrams. *ASM International, Materials Park, OH, USA*, 12:3528–3531, 1990.

[177] PR Subramanian and DE Laughlin. Cu-pd (copper-palladium). *Journal of phase equilibria*, 12(2):231–243, 1991.

[178] H Okamoto and TB Massalski. The au- pd (gold-palladium) system. *Bulletin of Alloy Phase Diagrams*, 6(3):229–235, 1985.

[179] Matthias Graf, Bao-Nam Dinh Ngô, Jörg Weissmüller, and Jürgen Markmann. X-ray studies of nanoporous gold: Powder diffraction by large crystals with small holes. *Physical review materials*, 1(7):076003, 2017.

[180] Hongliang Xin, Aleksandra Vojvodic, Johannes Voss, Jens K Nørskov, and Frank Abild-Pedersen. Effects of d-band shape on the surface reactivity of transition-metal alloys. *Physical Review B*, 89(11):115114, 2014.

[181] Naoki Takehiro, Ping Liu, Andreas Bergbreiter, Jens K Nørskov, and R Jürgen Behm. Hydrogen adsorption on bimetallic pdau (111) surface alloys: minimum adsorption ensemble, ligand and ensemble effects, and ensemble confinement. *Physical Chemistry Chemical Physics*, 16(43):23930–23943, 2014.

[182] Fereshteh Dehghani Sanij, Vitalii Latyshev, Serhii Vorobiov, Hoydoo You, Dominik Volavka, Tomas Samuely, and Vladimir Komanicky. Preparation of gold-modified palladium thin films as efficient catalysts for oxygen reduction reaction. *arXiv e-prints*, pages arXiv–2401, 2024.

[183] S Luo, D Wang, and Ted B Flanagan. Thermodynamics of hydrogen in fcc pd-au alloys. *The Journal of Physical Chemistry B*, 114(18):6117–6125, 2010.

[184] Kazuhiro Namba, Shohei Ogura, Satoshi Ohno, Wen Di, Koichi Kato, Markus Wilde, Ivo Pletikosić, Petar Pervan, Milorad Milun, and Katsuyuki Fukutani. Acceleration of hydrogen absorption by palladium through surface alloying with gold. *Proceedings of the National Academy of Sciences*, 115(31):7896–7900, 2018.

[185] Ying Shi, Xiaohong Yu, Changfeng Chen, and Haobo Yu. Influence of hydrogen on the elastic properties and dislocation behavior in Fe – Cr and Fe – Ni alloys by dft calculations. *Scientific Reports*, 14(1):21338, 2024.

Publications & Conferences

Publications

1. Sun, H., Lührs, L., Chang, W. C., & Shi, S. **Scaling behaviour of Poisson's ratio in hierarchical nanoscale network materials**, *Acta Materialia*, (2025) 121393.

2. Sun, H., Huang, Y., & Shi, S. **Bulk nanoporous platinum for electrochemical actuation**. *Energy Mater. Devices*, (2023) *1*, 9370006.

Conference contributions

1. Sun, H., Lührs, L., Chang, W.-C., & Shi, S. **Scaling behavior of Poisson's ratio in hierarchical nanoporous materials**, DPG Frühjahrstagung 2025, 16–21 March 2025, Universität Regensburg, Germany. (*talk*)

2. Sun, H., Huang, Y., & Shi. **Dealloying-made bulk nanoporous platinum for electrochemical actuation**, MSE Congress 2024, 24–26 September 2024, Technische Universität Darmstadt, Germany. (*talk*)